Int. J. High Technology Ceramics **1** (1985) 1–2

Editorial

The concept of 'a ceramic' has seen a dramatic change during the last 25 years. This is largely the result of the development in this period of a wide range of high purity ceramic materials with controlled microstructures, possessing closely defined properties and designed for specific applications, for the most part, in the areas of electrical and mechanical engineering.

The principal objective stimulating the development of the high-performance structural ceramics (for example, the silicon nitrides, silicon carbides and sialons) was the realisation of a gas turbine running at a substantially higher temperature than can be achieved with metals. Although the ultimate aim of a commercial high temperature gas turbine using ceramic components has not yet been realised, important uses for these ceramics are already well established, and the number of applications and the quantities of material involved will grow. The automotive industry is very much attracted by the use of ceramics in the Diesel engine, with the attendant promise of increased efficiency in the use of fuel. The main contender in this field is probably the group of zirconia ceramics, with the prospect of a range of tougher and effectively less brittle materials.

At present, the largest market for advanced ceramics exists in the electronics field. Their rapid development started about 40 years ago in parallel with that of the electronics and communications industries. Today, alumina and beryllia are well established as insulators, ferrites as magnetic materials, and titanates as high permittivity piezoelectric and electro-optical components. The constant striving to fully exploit electroceramics is stimulating research into the crystal structure, microstructure and macrostructure/property relationships. This in turn is demanding starting powders of closely defined chemical and physical specifications.

Since the market value of components in many novel applications tends to be high, relatively expensive raw materials can be considered for their manufacture. The use of synthetic raw materials is probably the most

Int. J. High Technology Ceramics (**1**) (1985)—

significant distinguishing feature of *high technology* ceramics vis-à-vis the *traditional* ceramics which are of necessity based on indigenous raw materials. However, there will always be an economic limit to the 'ceramic' solution to a problem and much future work will be concerned with the production of powders at the 'right' price. The components required are, moreover, often of very complex shape and have to conform to close dimensional tolerances. Their reliable production, free from performance-inhibiting flaws, is another important field for research and development, linked in turn to the search for the 'ideal' powder.

Until now there has been no journal the primary function of which has been to report on research and development in the field of these advanced ceramics. Publications on this subject are scattered over a variety of journals which cover, for example, general ceramics (often including glass and cement), materials science and engineering, powder technology, and various branches of engineering. The *International Journal of High Technology Ceramics* has the object of bringing together the publication of all matters pertaining to technical ceramics, starting from raw materials through fabrication to their actual application, including aspects of the problems of designing with ceramic materials. One particular aim is to bring into closer association the materials scientist, the ceramic manufacturer and the user. Through the bringing together in one journal the science, technology and applications of materials which may apparently be unrelated, but which nevertheless share important common features, the stimulation and the cross-fertilization of ideas may be the more readily achieved.

Thus it is intended that research papers and reviews will appear concerning powder synthesis, the shaping of components and their consolidation by sintering, the development of special microstructures and the resulting properties of advanced ceramics. As part of these contributions, authors will be asked to state the reason for the work undertaken in the light of the applications envisaged, and to assess whether the work has achieved its technical or economic goal; in the absence of this achievement, the reasons for its failure should be analysed. Additionally, *High Technology Ceramics* will publish regularly a calendar of events of interest to the readership. Brief reports of relevant meetings that have been attended and 'Letters to the Editor' will be welcome.

The Editor is being assisted by members of an international Editorial Board, all of whom are well known for their involvement in high technology ceramics. Jointly, they are determined, by accepting only high quality contributions which have passed an established refereeing procedure, to make *High Technology Ceramics* the leading publication in this field.

Paul Popper

Int. J. High Technology Ceramics **1** (1985) 3 30

High Purity Mullite Ceramics by Reaction Sintering

P. D. D. Rodrigo* and P. Boch

ENSCI, 47 avenue Albert Thomas, 87065 Limoges Cedex, France

SUMMARY

A review of studies of the synthesis and densification of mullite ceramics suggests that reaction sintering could be the best way to obtain high purity, dense mullite from common materials (amorphous silicon dioxide and α-aluminium oxide). The use of fine grain powder mixtures allows us to obtain dense ceramics after firing at 1600°C, because such fine powders favour densification more than mullite formation, which slows down the sintering rate. The aluminium oxide to silicon dioxide ratio appears to be a critical parameter: densification reaches its maximum (97%) for the stoichiometric $3Al_2O_3 \cdot 2SiO_2$ (mullite), whereas it reaches its minimum for compositions close to 75·0 wt% Al_2O_3, in which excessive grain growth occurs. Moreover, these compositions seem to correspond to the solubility limit of Al_2O_3 in mullite.

1. INTRODUCTION

Mullite is the main crystalline phase in most of the alumino-silicate ceramics, and the Al_2O_3–SiO_2 system, to which mullite belongs, has been extensively studied. Besides, mullite is an important refractory material, which is generally produced by fusion in an electric arc furnace. However, rather few studies have been devoted to the production of high purity, dense mullite ceramics. Nevertheless, the properties of mullite can explain the growing interest that this material arouses as a potential engineering

* On leave from the Department of Materials Engineering, University of Moratuwa, Sri Lanka.

Int. J. High Technology Ceramics 0267-3762/85/$03·30

ceramic: good chemical and thermal stability, high refractoriness and low creep rate, low thermal expansion and thermal conductivity, medium strength and toughness, not very far from those of alumina, not to mention useful dielectric properties.

The present paper begins with a review of studies on the synthesis and sintering of mullite ceramics, and lists the principal data about mullite formation and mullite sintering in order to draw attention to the influence of the main parameters: the nature of the raw materials, particle size, aluminium oxide to silicon dioxide ratio, and additives or impurities. Because of the seemingly low atomic mobility in mullite, and the fact that high purity, fine grain, mullite powders are not common ceramic raw materials, we will then examine the reaction sintering of silicon dioxide and aluminium oxide mixtures, in order to determine the best way of producing high-quality mullite ceramics.

2. HIGH PURITY MULLITE CERAMICS

2.1. The Al_2O_3–SiO_2 binary system

This system appeared to be simple when the first equilibrium diagram was proposed by Bowen and Greig[1] in 1924. According to these authors, mullite is a compound of a fixed composition, $3Al_2O_3 \cdot 2SiO_2$ (71·8 wt % Al_2O_3), which melts incongruently at 1810 °C. Since then there have been many conflicting views on the Al_2O_3–SiO_2 diagram, mainly concerning mullite.

In 1962 Aramaki and Roy[2] proposed a new diagram in which mullite is a solid solution, stable in the range of composition from 71·8 to 74·3 wt % Al_2O_3, which melts congruently at 1850 °C. They provided evidence for the possibility of extending the range of mullite solid solution up to about 77·5 wt % Al_2O_3 under metastable conditions. Although this diagram is in good agreement with the results of studies demonstrating the solubility of Al_2O_3 in 3:2 mullite[3-6] and the congruent melting of mullite,[7-9] it did not explain the observed incongruent melting of mullite.[6,10-12]

Aksay and Pask[13] were the first to explain both congruent and incongruent melting of mullite. The binary system (Fig. 1), constructed using their own experimental results and those of many other workers,[2,14-20] shows that under stable equilibrium conditions mullite melts incongruently at 1828 ± 10 °C; its stable solid solution ranges from 70·5 to 74·0 wt % Al_2O_3 below 1753 °C and from 71·6 to 74·0 wt % Al_2O_3 at 1813 °C. However, they observed that ordered mullite melts congruently during superheating in the absence of α-Al_2O_3 and that disordered mullite solidifies congruently from supercooled aluminium silicate melts. These observations

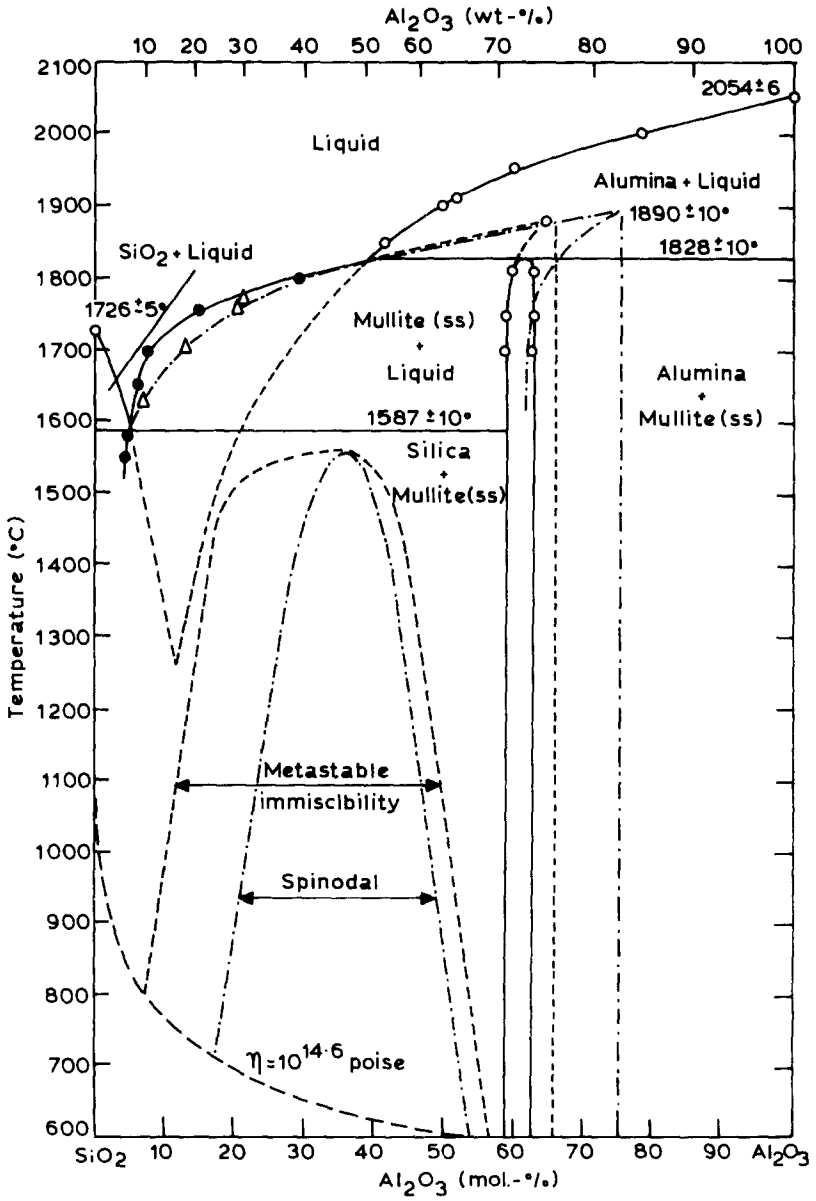

Fig. 1. The Al_2O_3-SiO_2 system according to Aksay and Pask.[13]

were shown to be associated with the difficulty of nucleation of α-Al_2O_3 in the absence of α-Al_2O_3 nuclei or nucleation sites such as sharp edges. This leads to the conclusion that congruency of mullite is observed under metastable conditions. The SiO_2-ordered mullite metastable diagram (ordered mullite melts congruently at $\simeq 1880\,°C$ and its solid solution range extends to $\simeq 77\,wt\%$ Al_2O_3) and the SiO_2-disordered mullite metastable

TABLE 1
Mullite Formation from Different Raw Materials

Reference	*Raw materials*	*Beginning of mullitization*	*Completion of mullitization*	*Other remarks*
28	Aluminium oxide–silicon dioxide mixtures prepared by hydrolysing tetraethyl silicate in the presence of aluminium hydroxide	1100–1200 °C		
29	Aluminium trichloride and silicon tetrachloride; hydroxides coprecipitated using ammonium hydroxide and dried at 150 °C	≃1100 °C	≃1150 °C	
30	Aluminium oxide–silicon dioxide mixtures of 3:2 composition prepared by hydrolysing a mixture of aluminium tris isopropoxide and silicon tetrakis isopropoxide	≃1200 °C		Surface area of as-prepared powder ≃550 $m^2 g^{-1}$ decreased down to ≃280 $m^2 g^{-1}$ when calcined at 600 °C for 1 h
27	Very fine γ-aluminium oxide (300 Å) and amorphous silicon dioxide (130–140 Å) mixed via a gel technique	≃1200 °C	≃1400 °C	
26	Aluminium oxide–silicon dioxide mixtures prepared from organo-metallic precursors	≃1200 °C	≃1500 °C	At 980 °C mixtures contained γ-Al_2O_3, HAl_5O_8 and amorphous silicon dioxide
31	Amorphous colloidal precipitate obtained from aluminium trichloride and silicon tetrachloride treated according to a process described by authors		Only mullite at 1400 °C	
36	A solution of aluminium nitrate and ethyl silicate in water–methanol (1:1 by volume) dried at 350 to 650 °C, by spraying into a reaction tube	≃980 °C	Only mullite at >980 °C	
22	α-Aluminium oxide (A14-ALCOA) and cristobalite α-Aluminium oxide (A14-ALCOA) and quartz	After 6 h at 1415 °C After 24 h at 1415 °C		Mean particle size of all powders was ≃3 μm
32	Baker's aluminium hydroxide and silicic acid		After 8 h at 1700 °C	
33	α-Aluminium oxide (A14-ALCOA) and α-quartz (Illinois Mineral Co.)		After 8 h at 1700 °C	
35	High purity aluminium oxide and quartz mixtures of 3:2 (71·8 wt% aluminium oxide) composition		≃5·5 wt% unreacted aluminium oxide after 12 days at 1500–1540 °C with four intervening grinding and mixing periods	
23	α-Aluminium oxide (XA16-ALCOA) and fused silica (Corning 7940)	≃1480 °C		
34	Aluminium oxide (KC-14, Kaiser aluminium and chemical sales) and potter's flint, mixed and ground for 48 h in a ball mill — 71·8 wt% Aluminium oxide 77·2 wt% Aluminium oxide		A very little unreacted aluminium oxide after sintering at 1710 °C A considerable amount of unreacted aluminium oxide after sintering at 1650 °C	Both mixtures contained 1 wt% magnesium oxide

diagram (disordered mullite melts congruently at $\simeq 1900\,^{\circ}C$ and its solid solution range extends to $\simeq 83{\cdot}0$ wt % Al_2O_3) correspond to two metastable conditions. In addition, the results of Davis and Pask[15] have shown the existence of a third Al_2O_3(α-Al_2O_3)–SiO_2(cristobalite) metastable diagram with a eutectic at low temperature ($\simeq 1260\,^{\circ}C$) but no mullite.

2.2. Synthesis of mullite

There have been many studies of the effects of different parameters on the synthesis of high purity mullite from aluminium oxide and silicon dioxide, or other synthetic raw materials which transform into these two oxides on heating. The crystalline form of the initial raw materials, their particle size, the SiO_2/Al_2O_3 ratio of the initial composition, and the presence of additives or impurities were found to be the major parameters controlling the mullite formation temperature and the nature of the final product.

2.2.1. Effect of the crystalline form of the SiO_2 and Al_2O_3 components
Wahl *et al.*[21] studied the formation of mullite from mixtures of α-quartz, silicic acid or β-cristobalite, with diaspore ($HAlO_2$), gibbsite ($Al(OH)_3$) or α-Al_2O_3. The mixtures of 1:4, 2:3, 3:2 and 4:1 SiO_2/Al_2O_3 mole ratio (or 87·2, 71·8, 53·1 and 29·8 wt % Al_2O_3) were prepared by mixing each of the SiO_2 components with each of the Al_2O_3 components and were fired up to 1450 °C. The X-ray diffraction experiments showed that cristobalite reacts better than the other two SiO_2 components with any of the three Al_2O_3 components and diaspore reacts better than the other two Al_2O_3 components with any of the three SiO_2 components. Their finding concerning cristobalite was later confirmed by Pask and co-workers,[22,23] who studied the sintering behaviour of the mixtures of quartz, cristobalite or amorphous silicon dioxide with α-Al_2O_3 (Table 1). Pask and co-workers explained the earlier formation of mullite in the cristobalite–α-Al_2O_3 mixture as a result of the formation of a metastable liquid phase, in accordance with the metastable Al_2O_3–cristobalite diagram without mullite. Staley and Brindley[24] have also noted the formation of such a non-crystalline phase during reactions between cristobalite and corundum and they considered it as a feature of the subsolidus reaction in the Al_2O_3–SiO_2 system.

DeKeyser[25] studied reactions occurring at 1600 °C at the interface between pressed pellets of aluminium oxide and silicon dioxide and found that a glassy phase was formed as a result of the diffusion of aluminium oxide into the silicon dioxide zone, while the mullite crystals grew with their *c*-axes oriented parallel to the direction of diffusion as a result of the movement of silicon dioxide into the aluminium oxide zone. Using DTA

results on aluminium oxide–silicon dioxide mixtures of various compositions, prepared from organo-metallic precursors, West and Gray[26] studied mullite formation up to 1500 °C, and reported that mullite develops at 1000 °C if the reaction is between amorphous silicon dioxide and hydrogen aluminium spinel (HAl_5O_8), whereas it develops at about 1200 °C once HAl_5O_8 is completely transformed into γ-Al_2O_3, which is less reactive than the defect spinel, HAl_5O_8.

Considering the crystal chemistry of the mullitization of kaolinite via metakaolinite (which has a γ-Al_2O_3-type spinel structure), Ghate *et al.*[27] assumed that γ-Al_2O_3 should react easily with amorphous silicon dioxide to give mullite. Mixtures of 71·8 wt% Al_2O_3 of amorphous silicon dioxide (130–140 Å) and γ-Al_2O_3 (300 Å), prepared by them via a gel technique, mullitized completely after 20 h at 1420 °C. The absence of α-Al_2O_3 during mullitization, and the gradual disappearance of traces of silicon dioxide, suggested the reaction was most likely occurring through diffusion and rearrangement of the spinel structural unit in agreement with the original hypothesis.

From all these data it is clear that the mullite-forming temperature is highly controlled by the crystalline forms of the SiO_2 and Al_2O_3 components. Cristobalite and γ-Al_2O_3, or other aluminium oxide components with a defect structure, seem to be the most reactive of the silicon dioxide and aluminium oxide components.

2.2.2. Effect of the particle size of aluminium oxide and silicon dioxide components

The experimental results of different investigators, summarized in Table 1, show that the mullitization of aluminium oxide–silicon dioxide mixtures has always been easier (complete mullitization below $\simeq$1500 °C) for techniques giving ultrafine particles,[26–31] whereas, in classical powder mixtures of larger particle size, detectable amounts of mullite are formed only at temperatures above 1400 °C and complete mullitization requires treatments at a temperature near 1700 °C. This is in good agreement with the generally accepted fact that the rate of a solid-state reaction increases as the particle size of the constituents decreases.

2.2.3. Effect of aluminium oxide/silicon dioxide ratio

The results of most of the investigations dealing with this subject are summarized in Table 2. None of the investigators have studied the effect of the aluminium oxide/silicon dioxide ratio on mullitization temperature. However, Wahl *et al.*[21] have observed that the beginning of mullite formation in diaspore–cristobalite mixtures always occurs at 1200 °C,

whatever the aluminium oxide/silicon dioxide ratio. This could suggest that mullitization temperature is not considerably affected by the aluminium oxide/silicon dioxide ratio.

It appears that firing silicon dioxide–aluminium oxide mixtures in the absence of a liquid phase produces mullite of nearly stoichiometric (3:2) composition (71·8 wt% Al_2O_3), though some exceptions[26] have been noticed. Probably the composition of such mullite lies in the stable solid solution range which varies from ≃70·5 to ≃74·0 wt% Al_2O_3 below ≃1750 °C (Fig. 1).

Mullites of higher aluminium oxide contents (>74·0 wt% Al_2O_3) are formed only in the presence of a liquid phase, as has been observed by Kriven and Pask,[38] Risbud and Pask,[39] and Neuhaus and Richartz[5] in supercooled aluminium silicate liquids. Such high aluminium oxide meltgrown mullites are sensitive to heat treatments, and a long annealing at a subsolidus temperature leads to exsolution of aluminium oxide.

Meltgrown mullite (or mullite formed in the presence of a liquid phase) always exhibits an acicular morphology, whereas the microstructure of mullite formed in the absence of a liquid phase can be equiaxed, and varies depending on the nature and the purity of raw materials, as well as on the composition of the starting aluminium oxide–silicon dioxide mixture. The presence of free aluminium oxide in the final product due to a high aluminium oxide/silicon dioxide ratio of the starting mixture[28,33] and/or the absence of even a small amount of intergranular glassy phase—as the one which can be formed in the presence of impurities[27]—lead to a chunky, granular microstructure. On the other hand, the choice of amorphous raw materials, intimately mixed in a molecular scale[28,30] and/or the presence of an intergranular glassy phase,[30,33] lead to a microstructure with acicular or elongated grains.

2.2.4. Effect of the presence of additives or impurities

Although this has been the subject of a large number of investigations, it is difficult to interpret the results of most of those studies, because the natural raw materials used (e.g. kaolinite) may have already contained unknown, and perhaps noticeable, amounts of different impurities. Therefore, it seems preferable to consider only the results of investigations done using high purity synthetic raw materials (Table 3).

Iron(III) oxide, chromium(III) oxide and titanium dioxide have been found to enter into solid solution with mullite in considerable quantities (respectively, 10–12 wt% above 1300 °C, 8–10 wt% above 1600 °C and 2–4 wt% above 1300 °C). They cause an increase of the unit cell volume. Because the presence of zirconium dioxide increases the sintering rate of mullite, a very low solubility of zirconium dioxide in mullite, as reported by

TABLE 2
Effect of Composition on Synthesis and Microstructure of Mullite

Reference	*Raw materials and preparation of aluminium oxide–silicon dioxide mixtures*	*Composition of the mixtures*	*Firing conditions*	*Crystalline phases present*	*Microstructural details*	*Other remarks*
21	Diaspore + cristobalite and gibbsite + silicic acid	87·18, 71·80, 53·13 and 29·82 wt% aluminium oxide	Fired up to ≃1450 °C	Mullite, corundum and cristobalite in all mixtures		Amount of mullite was always high for 71·8 wt% Al_2O_3 composition; mullitization temperature is not affected by aluminium oxide/silicon dioxide ratio
34	Aluminium oxide + potter's flint + magnesium oxide mixed and ground for 48 h in a ball mill and dried at 110 °C	71·8 wt% aluminium oxide + 1 wt% magnesium oxide	Fired up to 1710 °C	Almost 100% mullite		A mechanical mixture of fired 71·8 wt% Al_2O_3 composition and corundum with a total of 77·2 wt% Al_2O_3 gave an XRD pattern similar to that of fired 77·2 wt% Al_2O_3 composition
		77·2 wt% aluminium oxide + 1 wt% magnesium oxide	Fired up to 1650 °C	Mullite and corundum		
37	Amorphous silicon dioxide and amorphous aluminium oxide	71·8 wt% aluminium oxide	Fired at 1690 °C for 8 h	Only mullite		
29	Aluminium trichloride and silicon tetrachloride; hydroxides coprecipitated using ammonium hydroxide and dried at 150 °C	62·96 wt% aluminium oxide	Fired up to 1500 °C	Mullite and cristobalite		
		68·00, 71·83 and 74·84 wt% aluminium oxide		Only mullite		
		77·27 wt% aluminium oxide		Mullite and corundum		
33	γ-Aluminium oxide (A14-ALCOA) and γ-quartz wet mixed in a porcelain ball mill, dried and calcined at 1700 °C for 8 h	60·0 and 65·0 wt% aluminium oxide	Sintered at 1700 °C	Mullite	Totally densified due to the presence of a large amount of liquid phase	
		71·8, 73·0 and 74·0 wt% aluminium oxide	Sintered at 1700 °C	Mullite	A very small amount of an intergranular glassy phase led to the formation of a few elongated grains in an equiaxed matrix	
		75·0, 80·0, 85·0 and 90·0 wt% aluminium oxide	Sintered at 1700 °C	Mullite and corundum	Mullite and corundum formed an equiaxed structure	
36	A solution of aluminium nitrate and ethyl silicate in water–methanol (1:1 by volume), spray dried at 350–650 °C	71·8 wt% aluminium oxide	Calcined up to 1000 °C and sintered at 1650 °C for 4 h	Only mullite at any temperature above 980 °C		

28	Hydrolysing tetraethyl silicate in the presence of aluminium hydroxide or Wet milling colloidal aluminium oxide (Dispal 'M') and colloidal silicon dioxide (Ludox) in a rubber-lined ball mill for 16 h Commercial mullites	≥ 73·9 wt % aluminium oxide prepared from both methods Between ≃ 72·6 and ≃ 73·6 wt % aluminium oxide prepared from both methods	1650, 1700 or 1750 °C	Mullite and corundum Only mullite	Mainly equiaxed grains A mixture of acicular and polygonal grains Small interlocking acicular grains with a large amount of glassy (intergranular) phase	
30	Hydrolysing a mixture of aluminium tris isopropoxide and silicon tetrakis isopropoxide followed by calcination at 600 °C for 1 h	71·8 wt % aluminium oxide	Fired from 1200–1700 °C Vacuum hot-pressed at 1500 °C for 30 min	Only mullite at any stage Only mullite	A mixture of acicular and polygonal grains	
27	γ-Aluminium oxide (300 Å) and amorphous silicon dioxide (130–140 Å) mixed via a gel technique	71·8 wt % aluminium oxide	Fired at 1420 °C for 20 h	Only mullite	Equiaxed grains	
26	Prepared from pure organo-metallic precursors purified by chemical methods	74·53 and 66·68 wt % aluminium oxide	Heated up to 1500 °C	Mullite and corundum (due to incomplete reaction)		Intensity of mullite peaks in XRD patterns showed more mullite in 74·53 wt % Al_2O_3 mixture
38	α-Aluminium oxide and fused silicon dioxide	70·0 wt % aluminium oxide 75·0 wt % aluminium oxide 77·5 wt % aluminium oxide	Homogenized at 2100 °C for 24 h and slowly cooled to solidification over 13 days	Mullite with 76·7 wt % Al_2O_3 Mullite with 77·2 wt % Al_2O_3 Mullite with 77·8 wt % Al_2O_3	Bundles of acicular mullite needles in a glassy matrix	
39	α-Aluminium oxide (XA16-ALCOA) and fused silica (Corning 7940)	60·0 wt % aluminium oxide	Homogenized at 2090 °C for 55 min Quenched to room temperature Undercooled to 1725 °C; held for 1·5 h; quenched After quenching to room temperature, reheated at 1725 °C for 70 h	Mullite with 78·4 wt % Al_2O_3 Mullite with 74·5 wt % Al_2O_3	Long mullite needles (≃ 20 × 250 μm) in a glassy phase having 18·5 wt % Al_2O_3 Mullite needles of larger section (≫ 20 μm) in a glassy phase having 23·5 wt % Al_2O_3	When homogenized melt was quenched to room temperature and reheated at 1725 °C, initial mullite needles (≃ 20 × 250 μm) recrystallized and grew in section while the Al_2O_3 content of the liquid phase increased from 18·5 to 23·5 wt % Al_2O_3 due to exsolution of Al_2O_3 from mullite, changing its composition from 78·4 to 74·5 wt % Al_2O_3

TABLE 3
Influence of Additives on Synthesis of Mullite

Reference	*Additive*	*Solubility of additive in mullite*	*Effect of additive on:*			*Other remarks*
			Mullite lattice parameters	*Mullitization*	*Mullite grain growth*	
32	Fe_2O_3	< 5 wt% at 1200°C, 10–12 wt% at 1300°C	All lattice parameters increase with Fe_2O_3 content in solid solution			
	Cr_2O_3	Negligible at 1200°C, 8–12 wt% at 1600°C	All lattice parameters increase with Cr_2O_3 content in solid solution			
	TiO_2	Negligible at 1200°C, 2–4 wt% at 1600°C	All lattice parameters increase with TiO_2 content in solid solution			
29	Fe_2O_3	≃ 12 wt% at 1300°C	Cell volume increases with Fe_2O_3 content in solid solution	Lowers the mullitization temperature; enhances mullitization	Increases the rate of grain growth	All mixtures were studied in the temperature range 900–1500°C and contained 3–12 wt% additive
	TiO_2	≃ 3 wt% above 1300°C	Cell volume increases with TiO_2 content in solid solution	Enhances mullitization (effect is less than that of Fe_2O_3)	Inhibits grain growth	
45	Fe_2O_3	7·7 wt% at 1300°C				Refractive index increases and XRD lines shift with Fe_2O_3 content in solid solution
	FeO	Not soluble				FeO reacts with mullite at ≃ 1190°C to give $FeAl_2O_4$ and Fe_2SiO_4

43	Fe_2O_3	High		Increases the rate of grain growth	All mixtures were studied in the temperature range 1650–1700 °C; Fe_2O_3 changes the morphology of mullite from 'rectangular with rounded ends' to 'acicular'
	TiO_2	Low		Increases the rate of grain growth (effect is less than that of Fe_2O_3	
	CaO	Very low		Increases the rate of grain growth (effect is more than that of Fe_2O_3	
	K_2O, Na_2O			No effect	
46	Fe_2O_3		Enhances mullitization when <5 mol % added		All mixtures were fired at 1200 °C for 9 h; presence of K_2O and Na_2O diminishes the effect of Fe_2O_3 and TiO_2; the effect of TiO_2 depends on the Al_2O_3/SiO_2 ratio of the mixtures
	TiO_2		Enhances mullitization (effect is less than that of Fe_2O_3)		
	Na_2O, K_2O		No effect		
44	TiO_2	Not more than 3 wt % at any temperature		Increases grain growth (0·3 μm without TiO_2; 2·0 μm with 3 wt % TiO_2, when fired at 1600 °C for 1 h)	Presence of TiO_2 in excess of solubility limit (i.e. >3 wt %) decreases the rate of sintering, probably due to the precipitation of Al_2TiO_5 at the grain boundaries
42	Ba^{2+}, Ca^{2+}, Be^{2+}		Enhances mullitization		All mixtures were studied at 1350 °C; Ba^{2+}, Ca^{2+} and Be^{2+} increase the amount of mullite formed from 53 % to 91, 88 and 75 %, respectively, while Fe^{3+} and Ni^{3+} decrease mullitization by 46 and 40 %, respectively
	B^{3+}, Ti^{4+}, Zr^{4+}, Mn^{4+}, Mg^{2+}		No effect		
	Fe^{3+}, Ni^{3+}		Diminishes mullitization		
40	ZrO_2	Very low ($0·5 \pm 0·1$ wt %)			
41	ZrO_2	$\simeq 35$ wt % ZrO_2			

Moya and Osendi,[40] is probable, but a very high solubility of zirconium dioxide in mullite, as reported by Dinger *et al.*,[41] remains to be confirmed.

Despite the contradictory observation of Budnikov *et al.*,[42] who found a decrease of mullitization of aluminium oxide/silicon dioxide mixtures in the presence of Fe^{3+}, it generally appears that iron(III) oxide, titanium dioxide and calcium oxide facilitate mullitization of aluminium oxide/silicon dioxide mixtures. Iron(III) oxide favours grain growth and probably leads to a microstructure with large elongated grains, as Johnson and Pask[43] observed. On the other hand, small amounts of alkali-oxides do not appear to have a significant effect on mullitization or grain growth. For other additives, definitive conclusions cannot be drawn because of lack of precise information and/or contradictory observations.

2.3. Sintering of mullite

Although mullite has been the subject of many investigations, few of them have been devoted to the sintering of synthetic mullite. The results of those few studies (Table 4) show that the hot-pressing of very fine powders is required to obtain a full densification at rather low temperatures. For pressureless sintering, treatments at $< 1650\,^{\circ}C$ do not lead to densifications above 95%.

Nearly all the data concerning densification during hot-pressing, grain growth and creep lead to apparent activation enthalpies of about $700\,kJ\,mol^{-1}$. Such a value is very similar to that for lattice diffusion of Si^{4+} ($702\,kJ\,mol^{-1}$),[47] which could mean that the diffusion of silicon ions is the rate-controlling process for densification, grain growth and creep of mullite. Other creep data (stress component between 1·3 and 2,[48] grain size dependence of -2[49]) also support the idea that silicon diffusion plays the main role. However, it should be noted that Sacks and Pask[33] have observed an activation enthalpy of about $305\,kJ\,mol^{-1}$ for the early stages of densification during pressureless sintering.

On the one hand, mullite does not sinter easily and, on the other, high purity mullite powders are not so easily found in the market (compared to silicon dioxide and aluminium oxide powders). This strongly suggests the use of reaction sintering:

$$3Al_2O_3 + 2SiO_2 \rightarrow 3Al_2O_3 \cdot 2SiO_2$$

(for the case of 3:2 'stoichiometric' mullite).

However, it has been observed that the formation of mullite retards densification for α-aluminium oxide–amorphous silicon dioxide mixtures,[23] as well as α-aluminium oxide–quartz and α-aluminium oxide–cristobalite[22] mixtures. This could be linked to the two processes involved in reaction sintering (densification and reaction) which can be simultaneous or not, and

which can be mutually favourable or not. In the case of mullite, the high activation enthalpy of this compound makes it difficult to sinter at low temperatures. Moreover, dilatometric effects ($\rho(3Al_2O_3 + 2SiO_2) \simeq 3{\cdot}31\ Mg\,m^{-3} \rightarrow \rho(\text{mullite}) \simeq 3{\cdot}16\ Mg\,m^{-3}$) can disturb the densification mechanisms.

Hence it would seem better to densify before the mullitization, which could be done by varying one or more of the parameters involved in reaction sintering, such as the crystalline form of reactants, particle size, firing temperature and time. Particle size would seem the best parameter, as pointed out by Brook and Yangyun[50] in a general paper on reaction sintering: the densification kinetics depend on D^{-2} or D^{-3} (D being the mean particle size) whereas the reaction kinetics depend on D^{-1} or D^{-2}. Hence densification can be favoured against reaction by decreasing the particle size. This may be the reason why Moya and co-workers[44,51] succeeded in sintering at a fairly low temperature very fine 'premullite' powders (Table 4). However, the effect of the crystalline form of silicon dioxide and aluminium oxide on mullitization should also be employed to delay the reaction (i.e. using the least reactive aluminium oxide and silicon dioxide species). This encourages us to avoid the use of cristobalite and γ-aluminium oxide which favours the reaction, and to choose amorphous silicon dioxide and α-aluminium oxide with the complementary advantages that both materials are common ceramic raw materials and can be found in a wide range of grades, and that α-aluminium oxide has better compaction properties and a lower firing shrinkage than γ-aluminium oxide.

3. EXPERIMENTAL PROCEDURE

3.1. Preparation and sintering of specimens

The raw materials used were α-aluminium oxide* and amorphous silicon dioxide†. The powder mixtures were prepared by attrition milling in ethanol, using zirconia balls as the grinding media. The mill liner was of hardened steel. The iron introduced by grinding for 3 h (0·025 % Fe_2O_3) is less than the iron impurity in the aluminium oxide powder (0·03 %).

After drying, crushing and passing through a 200 μm sieve, the powder mixtures were mixed with 3 wt % polymethylmethacrylate dissolved in

*RC-172 DBM, Reynolds Metals Company, Chemical Division, Arkansas; chemical analysis (wt %): 0·05 Na_2O, 0·07 SiO_2, 0·03 Fe_2O_3 and 0·07 CaO; mean particle size $\simeq$0·64 μm.

† Alfa 89709 silicon(IV) oxide, <400 mesh powder (mean particle size $\simeq$3·6 μm); Alfa Research Chemicals and Materials, 7500 Karlsruhe; impurity content is <0·5 wt %.

TABLE 4
Sintering of Mullite

Reference	*Preparation of mullite*	*Composition* ($wt\%$ Al_2O_3)	*Sintering conditions*	*Porosity* (%)	*Activation enthalpy/kJ mol*$^{-1}$			*Other remarks*
					Sintering	*Grain growth*	*Creep*	
30	Derived from corresponding metal alkoxides	71·8	Vacuum hot-pressing at 1500 °C for 30 min	< 1				Before processing, as-prepared $3Al_2O_3 \cdot 2SiO_2$ powder, calcined at 600 °C for 1 h (specific surface $\simeq 280\,m^2\,g^{-1}$), was ground in a boron carbide mortar
49	Same as for Ref. 30	71·8	Vacuum hot-pressing at 1500 °C for 30 min	< 1			≃711	Grain size dependence of steady-state creep rate at 1400 °C was found to be -2
48	γ-Aluminium oxide (300 Å) and amorphous silicon dioxide (130–140 Å), mixed via a gel technique, was fired for 20 h at 1420 °C; surface area of mullite obtained was approximately $5{\cdot}5\,m^2\,g^{-1}$	71·8	Hot-pressed between 1470 and 1620 °C and ≃7 to ≃42 MPa	≃1·7 and ≃1·3 for hot-pressing at 1580 and 1620 °C	681 ± 92	761 ± 188		Stress component for creep was found to be 1·3–2·0
54	Same as for Ref. 48	71·8	Hot-pressed between 1450 and 1650 °C and ≃14 to ≃35 MPa	Minimum porosity was ≃5	706 ± 63			Stress component for creep was found to be 1·41 ± 0·65
28	Aluminium oxide and silicon dioxide of colloidal particle size mixed and milled in a rubber-lined ball mill, dried and calcined at 1560 °C for 3 h gave only mullite; it was ground for 6–114 h and all particles > 4 μm were removed	≃71·8	1 h at ≃1700 °C	2–3				Specimens were prepared by cold pressing under ≃155 MPa
	Aluminium oxide silicon dioxide mixtures obtained by hydrolysing tetraethyl silicate in the presence of aluminium hydroxide and calcined at 1400 °C for 4 h gave only mullite; it was wet or dry milled before agglomerating for cold pressing	≃71·8	1–4 h at 1650 °C 1–4 h at 1700 °C 1–4 h at 1750 °C	≃14 ≃3 ≃3				

33	Mixtures of A14-ALCOA (α-aluminium oxide) and α-quartz wet mixed in isopropanol in a porcelain ball mill, calcined at 1700 °C for 8 h, were crushed in a mechanically operated mortar and pestle and wet ground in a vibratory mill for 5 h	71·8 73·0 74·0	1 h 4 h 12 h } at 1700 °C	≃20 ≃13 ≃5·5	≃305 for early stages of sintering	Similar results were obtained using mullites prepared from two other processes; about 97% dense mullite was obtained from mullite powders ground for 36 h; specimens were die-formed under uniaxial pressure (17 MPa) followed by isostatically pressing at 170 MPa
52	α-Aluminium oxide (A16-ALCOA) and silicon dioxide (precipitated silica) milled in a plastic bottle for 2 h in methylated spirits with alumina balls was calcined and ground again for 1 h as above	71·8	2 h at { 1550 °C 1575 °C 1650 °C	16·6 11·8–14·4 9·6		Specimens were prepared by double-ended cold pressing under 70 MPa
53	Mixture of $Al(NO_3)_3 \cdot 9H_2O$ and silicon dioxide (Corning 9604) reactive fired for 24 h at 1600 °C was pulverized for 4 h in a vibrating mill using agate or alumina balls and ethanol: the slurry was dried and screened (average particle size ≃2 μm)	71·8	20 h at 1800 °C	≃7		Specimens (7–10 mm high, 6·4 mm in diameter) were obtained by uniaxial pressing at ≃120 MPa
36	Mixture of aluminium nitrate and tetraethyl silicate dissolved in water–methanol (1:1 by volume) sprayed into a preheated (650 °C) quartz reaction tube, calcined at 1000 °C for 1 h and ground in a vibrating mill for 50 h	71·8	4 h at 1650 °C	≃5		Surface area of as-prepared powder (≃15 $m^2 g^{-1}$) decreased down to ≃2 $m^2 g^{-1}$ when calcined at 1000 °C for 1 h; specimens were prepared by rubber pressing under 200 MPa
51	Al_2O_3–SiO_2 mixture of amorphous nature (called premullite) obtained by thermal and chemical treatment of a kandite (surface area ≃250 $m^2 g^{-1}$); powder was attrition milled for 1 h	72·2	2·5 h at 1570 °C	3·0		A considerable amount of impurities (e.g. CaO ≃0·2 wt%, Fe_2O_3 ≃0·15 wt%) were present in the prepared mullite; mullite formation begins at a temperature between 1200 and 1350 °C
44	Same as for Ref. 51	72·2	1–16 h at 1600 °C	≃5·0		Specimens were prepared by isostatically pressing under 200 MPa

diethyl ether (1 g in 100 ml) for 30 min and dried on a hot plate while mixed continuously. After evaporating the ether, the powder mixtures were de-agglomerated by crushing and passing through a 200 μm sieve. Specimens in the form of discs (30 mm diameter, 3–5 mm thickness) were obtained by cold pressing under $\simeq 150$ MPa in a floating steel die, using a simple hydraulic press. To obtain a better compaction and to minimize defects[55] the lower piston of the pressing assembly was subjected to an ultrasonic vibration (frequency = 20 kHz, amplitude = 10 μm) during the first 3 s of pressing.

Specimens were sintered in an electric furnace of low thermal inertia. The organic binder was burned off by heating at a low rate of $\simeq 15\,^{\circ}\mathrm{C\ min^{-1}}$ up to 800 °C and then heated at a rate of $\simeq 60\,^{\circ}\mathrm{C\ min^{-1}}$ up to the soaking temperature. After a given heat treatment the specimens were allowed to cool naturally in the furnace.

3.2. Characterization of the sintered specimens

The bulk density was determined using the liquid displacement technique with distilled water as the liquid media.

Microstructural observations were done on polished and thermally etched specimens using a JEOL T200 scanning electron microscope. Thermal etching time varied from 20 to 30 min depending on the etching temperature, which was always 100 °C less than the sintering temperature.

Both qualitative and quantitative analyses of the crystalline phases of the fired specimens were carried out using their X-ray diffraction (XRD) (Cu-Kα) patterns. The peaks used, corresponding to different phases, are given in Table 5.

S_M, S_C, S_A and S_{A^*} represent the areas under the respective peaks. Plots of $S_A/(S_M + S_A)$ or $S_{A^*}/(S_M + S_{A^*})$ versus α-aluminium oxide wt% for α-aluminium oxide–mullite mixtures and a plot of $S_C/(S_M + S_C)$ versus

TABLE 5
X-ray Diffraction Peaks of Different Phases Used for Quantitative Analysis

Crystalline phase	*Indices of the corresponding atomic plane*	*2θ value in Cu-Kα XRD pattern deg*	*Relative peak intensity*	*Interplanar distance* A	*Symbol*
Mullite	(210)	26·26	100	3·39	M
β-Cristobalite	(101)	21·92	100	4·05	C
α-Aluminium oxide	(113)	43·24	100	2·09	A
	(012)	25·58	70	3·48	A*

β-cristobalite wt % for β-cristobalite–mullite mixtures were constructed using XRD patterns of two series of mechanical mixtures. Mullite obtained by firing an amorphous silicon dioxide–α-aluminium oxide mixture of 71·8 wt % Al_2O_3 for 10 h at 1650 °C, β-cristobalite obtained by firing amorphous silicon dioxide for 10 h at 1600 °C and as-received α-aluminium oxide were used for preparing mechanical mixtures. The amount of free α-aluminium oxide or of free β-cristobalite present in fired specimens was determined using the $S_A/(S_M + S_A)$, $S_{A*}/(S_M + S_{A*})$ and $S_C/(S_M + S_C)$ ratios of the corresponding XRD patterns and the three plots constructed as explained above.

3.3. Results and discussion

3.3.1. Effects of the particle size of powders on the reactions and on the shrinkage behaviour

Powder mixtures of 71·8 wt % aluminium oxide composition attrition milled for 0, 1 and 5 h were used for this study. The dilatometric shrinkage curves (Fig. 2) were obtained using rectangular bars (4 × 4 × 20 mm) cut from pressed discs. The curves consist of a number of zones, which become more distinct with the increase of milling time. The sintering process is affected by

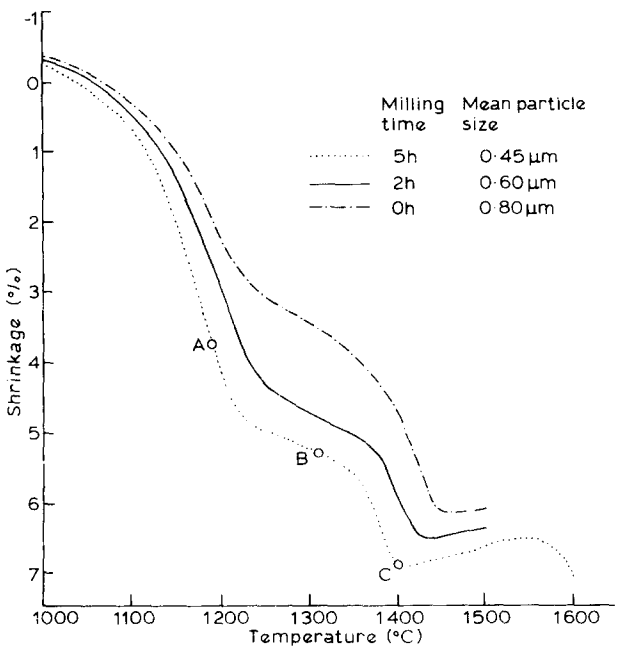

Fig. 2. Percentage shrinkage versus temperature for mixtures of 71·8 wt % aluminium oxide composition and different fineness.

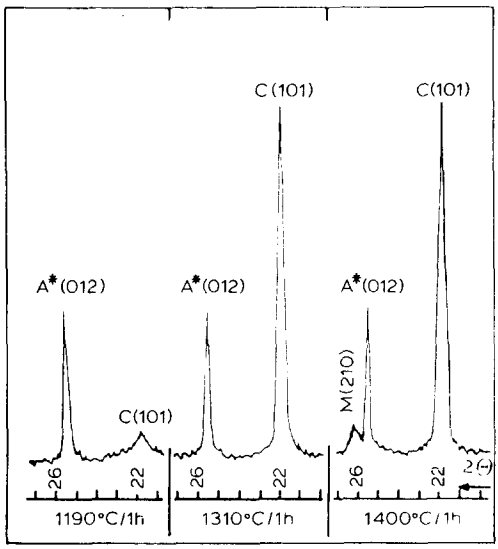

Fig. 3. X-ray diffraction patterns of 5 h attrition milled 71·8 wt % aluminium oxide mixture, fired under different conditions as indicated.

two phenomena, one taking place in a range of temperatures around 1300 °C and the other just above 1400 °C. To understand these phenomena, the mixture attrition milled for 5 h was studied further. Three samples of this mixture were fired for 1 h at 1190, 1310 and 1400 °C, the temperatures corresponding to the three points A, B and C marked on the corresponding shrinkage curve. After firing, they were analysed by X-ray diffraction. The observed XRD patterns are given in Fig. 3. At 1190 °C the most intense peak of cristobalite (C(101)) starts to appear and at 1310 °C it is of high intensity. The value of $S_C/(S_C + S_{A^*})$ is the same for XRD patterns corresponding to the specimens fired at 1310 and 1400 °C, which means that the cristobalite/aluminium oxide ratio remains almost constant from 1310 °C. At 1400 °C the (210) peak of mullite begins to develop. At any temperature above 1400 °C mullite develops at the expense of α-aluminium oxide and cristobalite. The following conclusions can be drawn from these observations:

1. Transformation of amorphous silicon dioxide into cristobalite takes place in the temperature range where the first sudden change in the rate of shrinkage is observed, and is almost complete before the beginning of the mullite formation.
2. The mullite formation starts just before the second sudden change in the rate of shrinkage and it causes a net overall expansion of the body.

The transformation of amorphous silicon dioxide (density $\simeq$ 2·22 Mg m^{-3}) into cristobalite (density $\simeq$ 2·32 Mg m^{-3}) is accompanied by a decrease of the rate of shrinkage, which is contrary to what would be expected for such a transformation, where a low-density phase transforms into a higher density phase. One possible reason for this behaviour is the formation of microflaws caused by a sudden contraction of silicon dioxide zones, which leads to a reduction of the number of particle-to-particle contacts. Another possible reason is the elimination of the amorphous phase (amorphous silicon dioxide), which may have helped densification at lower temperatures by acting as an easy diffusion path. The rapid rate of shrinkage just before the appearance of mullite (i.e. after the amorphous silicon dioxide → cristobalite transformation) may be due to the formation of a metastable liquid phase in accordance with the α-aluminium oxide–cristobalite metastable equilibrium diagram in the absence of mullite (Fig. 1).

By comparing these shrinkage curves, it can be seen that the reduction of particle size has caused an increase in the total shrinkage before mullitization, in addition to a slight reduction of the mullitization temperature. This shows the beneficial influence, for sintering, of using fine powders, as has been pointed out by Brook and Yangyun.[50] Hence, it may be possible to use the particle size effect to improve the densification before mullitization, during reaction sintering of aluminium oxide–silicon dioxide mixtures, thereby reducing the difficulty in sintering caused by the mullite formation.

3.3.2. Effect of composition on reaction, densification and microstructure

The effects of the composition on reaction and densification were investigated using five different compositions, namely 68·0, 71·8, 75·0, 77·3 and 80·0 wt % aluminium oxide, prepared by attrition milling for 3 h. The powder compacts were subjected to three different heat treatments (10 and 2 h at 1600 °C and 2 h at 1570 °C). The results of the experiments are given in Tables 6 and 7 and Figs 4a, 4b, 5 and 6. Although the results concerning specimens fired at 1570 °C for 2 h are given in Table 7 and Fig. 5, they are not discussed herein due to the difficulty of interpretation caused by incomplete reaction.

X-ray diffraction patterns given in Figs 4a and 4b correspond to the specimens fired at 1600 °C for 2 and 10 h, respectively. In both groups of XRD patterns, the compositions with 68·0 and 71·8 wt % Al_2O_3 do not show the presence of any crystalline phase other than mullite, but for the compositions with 75·0, 77·3 and 80·0 wt % Al_2O_3 the peaks of α-aluminium oxide can be seen. Their intensities show that the highest amount of free α-aluminium oxide is in the specimen with 80·0 wt % Al_2O_3 and the lowest

TABLE 6

Bulk Density and Relative Densification of α-Aluminium Oxide–Amorphous Silicon Dioxide Mixtures of Different Compositions, Fired Under Different Conditions

Composition (wt% aluminium oxide)	*Bulk density of the green compacts / Mg m⁻³ (% compaction)*	*2 h at 1570°C*		*2 h at 1600°C*		*10 h at 1600°C*	
		Density / Mg m⁻³	*Densification / %*	*Density / Mg m⁻³*	*Densification / %*	*Density / Mg m⁻³*	*Densification / %*
68·0	1·85 (58·3)	2·78	90·0	2·83	91·6	2·95	95·5
71·8	1·90 (58·4)	2·90	91·8	2·95	93·4	3·07	97·2
75·0	1·94 (58·4)	2·85	88·4	2·91	90·2	3·01	93·3
77·3	1·97 (58·4)	2·94	89·6	2·99	91·2	3·11	94·8
80·0	2·00 (58·2)	3·07	91·6	3·15	94·0	3·23	96·4

TABLE 7

Composition of Mullite Solid Solution in α-Al_2O_3–Amorphous Silicon Dioxide Mixtures of Different Al_2O_3/SiO_2 Ratios Fired at 1600 °C for 10 h

Composition of the mixture (wt% aluminium oxide)	*Estimated free α-aluminium oxide content (wt%)*	*Combined Al_2O_3 content (wt%)*	*Composition of mullite solid solution*[a] *(wt% Al_2O_3)*	*Free silicon dioxide content (wt%)*	*Theoretical density ($Mg\,m^{-3}$)*
68·0	—	68·0	71·8	5·3	3·09
71·8	—	71·8	71·8	—	3·16
75·0	1·0	74·0	74·7	—	3·225
77·3	10·0	67·3	74·8	—	3·28
80·0	20·5	59·5	74·8	—	3·35

[a] It was considered that the silicon dioxide-rich end of the mullite solid solution is 71·8 wt% Al_2O_3.

one in the specimen with 75·0 wt% Al_2O_3. This XRD observation is confirmed by the corresponding micrographs (Fig. 6): a noticeable amount of free α-aluminium oxide (white grains) in the 80·0 wt% Al_2O_3 specimen and a very low amount of free α-aluminium oxide (a few very small white grains, both at intergranular and intragranular positions) in the 75·0 wt% Al_2O_3 specimen.

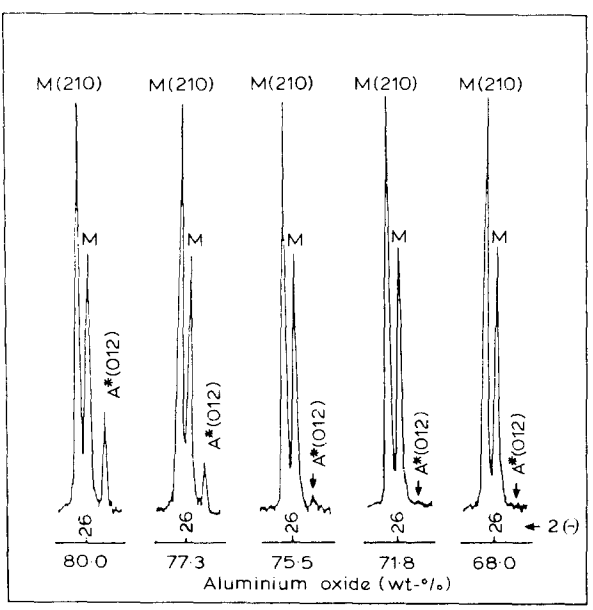

Fig. 4a. X-ray diffraction patterns (around the (210) mullite peak) of mixtures of various indicated aluminium oxide/silicon dioxide ratios fired for 2 h at 1600 °C.

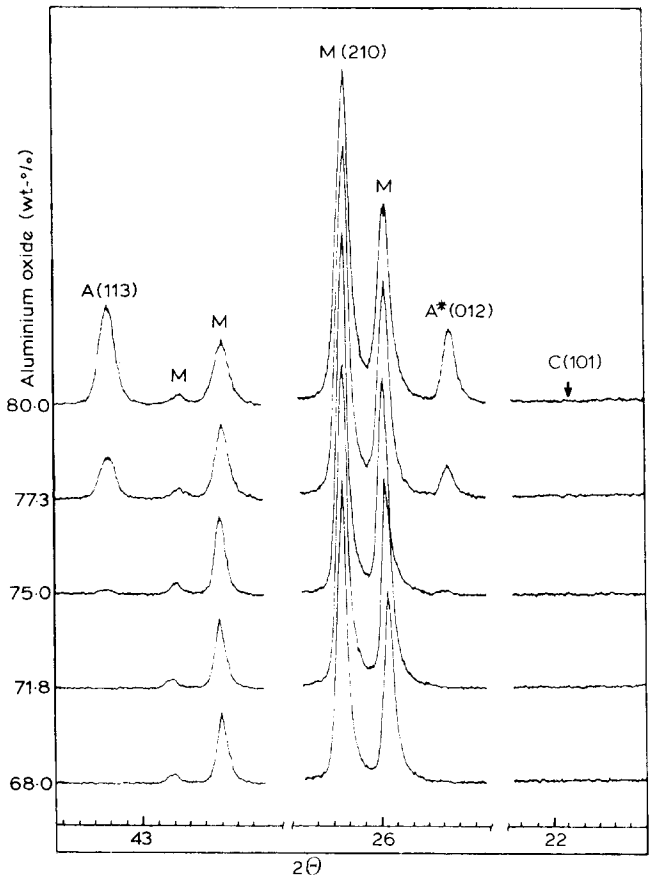

Fig. 4b. X-ray diffraction patterns of mixtures of various indicated aluminium oxide/silicon dioxide ratios fired for 10 h at 1600 °C.

Results of the quantitative estimations of free α-aluminium oxide in the specimens fired at 1600 °C for 10 h are given in Table 7. Similar results were obtained for specimens fired at 1600 °C for 2 h (see the similarity of XRD patterns in Figs 4a and 4b). Hence, mullitization has ended even before 2 h at 1600 °C.

If only α-aluminium oxide and mullite are present in fired 75·0, 77·3 and 80·0 wt % Al_2O_3 specimens, as evidenced by corresponding XRD patterns and micrographs, the composition of mullite in those specimens can be determined using the estimated values of free α-aluminium oxide (Table 7, column 2). It shows that the composition of the mullite solid solution remains constant at $\simeq 74{\cdot}8$ wt % and is independent of the original composition for mixtures having $\geq 75{\cdot}0$ wt % Al_2O_3. Consequently, the aluminium oxide-rich end of the mullite solid solution is limited to

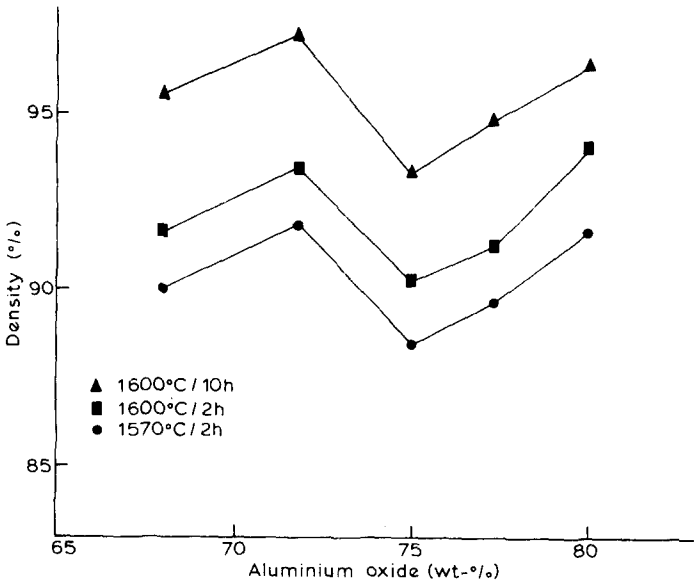

Fig. 5. Percentage density versus aluminium oxide content for α-aluminium oxide–amorphous silicon dioxide compacts fired under different conditions as indicated.

$\simeq 74{\cdot}8$ wt % Al_2O_3. This is slightly higher than the corresponding values obtained by Aramaki and Roy[2] and Aksay and Pask.[13]

If the silicon dioxide-rich end of the mullite solid solution is 71·8 wt % Al_2O_3 (as proposed by Aramaki and Roy) or 70·5 wt % Al_2O_3 (as proposed by Aksay and Pask), the fired 68·0 wt % Al_2O_3 specimen should contain $\simeq 5{\cdot}3$ or $\simeq 3{\cdot}5$ wt % free silicon dioxide, respectively. But no crystalline silicon dioxide was found in 71·8 and 68·0 wt % Al_2O_3 mixtures. However, this does not mean that the silicon dioxide-rich end of the mullite solid solution is below 68·0 wt % Al_2O_3, since, unlike free aluminium oxide, free silicon dioxide can be present as a vitreous phase. Hence no conclusion about the silicon dioxide-rich end of the mullite solid solution can be drawn without separating and analysing mullite in the fired 71·8 and 68·0 wt % Al_2O_3 specimens.

To determine the extent of densification, the theoretical density of each fired composition was calculated under the following assumptions:

1. The range of the mullite solid solution is from 71·8 to 74·8 wt % Al_2O_3, while its density varies from 3·16 to 3·22 Mg m^{-3}.
2. Excess aluminium oxide is present in the form of α-aluminium oxide (density = 3·98 Mg m^{-3}) whereas excess silicon dioxide is present in the form of a vitreous phase. The density of the latter was considered to be similar to that of the amorphous silica used (2·22 Mg m^{-3}).

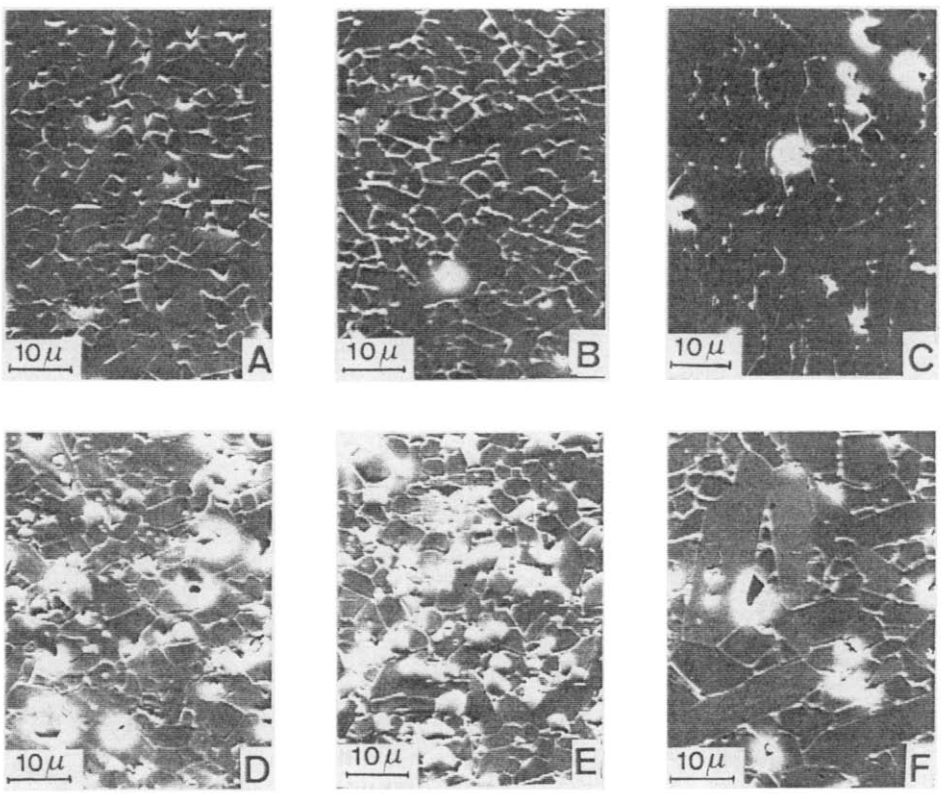

Fig. 6. Microstructures of (A) 68·0, (B) 71·8, (C) 75·0, (D) 77·3, (E) 80·0 and (F) 75·0 wt % Al_2O_3 compositions, fired 10 h at 1600 °C (thermal etching: 20 min at 1500 °C).

The bulk density and the percentage densification of each composition after each heat treatment are given in Table 6. Figure 5 shows that the densification versus wt % Al_2O_3 plots consist of maxima at 71·8 wt % Al_2O_3 and minima at 75·0 wt % Al_2O_3. This is confirmed by the micrographs in Fig. 6. The lower densification of the 75·0 wt % Al_2O_3 composition is coupled with a higher rate of grain growth, leading to a microstructure which consists of a mixture of large elongated grains ($\simeq 7 \times 30\ \mu m$) with small equiaxed grains ($\simeq 5 \times 5\ \mu m$), whereas the microstructures of the other compositions are more or less equiaxed. This peculiar behaviour of the 75·0 wt % Al_2O_3 composition is not yet understood and is being studied further.

4. CONCLUSIONS

This paper shows that the reaction sintering of amorphous silicon dioxide–α-aluminium oxide mixtures is a good way of producing high

purity, fine grain, nearly dense mullite ceramics. The comparison with alumina—which is justified by the fact that this material remains the archetype of high technology ceramics—demonstrates that reaction-sintered mullite can be processed using similar treatments as those required by 'reactive' aluminium oxide. Indeed, nearly dense ($\simeq 97\%$), fine grain ($\simeq 5\ \mu m$) mullite is obtained after firing for some hours at 1600 °C, i.e. after a treatment close to that required by RC-172 DBM Reynolds aluminium oxide. However, the particle size of the initial mixture must be as fine as possible, which could call for an additional grinding. The aluminium oxide/silicon dioxide ratio appears to be a critical parameter: the composition of $3Al_2O_3 \cdot 2SiO_2$ stoichiometric mullite ($\simeq 71{\cdot}8$ wt % Al_2O_3) leads to the best densification, and the finest microstructure. On the other hand, compositions near the limit of solubility of Al_2O_3 in mullite (74·8 wt % Al_2O_3) exhibit rather poor densification and excessive grain growth. Further studies are being done to understand this behaviour.

As far as the mechanical properties are concerned, reaction-sintered stoichiometric mullite has a room-temperature flexure strength of $\simeq 200$ MPa (biaxial flexure on 30 mm diameter discs) and toughness, K_{Ic}, of $\simeq 2{\cdot}2$ MPa $m^{1/2}$ (SENB experiments on $3 \times 3 \times 30$ mm).[56] The influence of temperature is rather moderate and the flexure strength at 900 °C is $\simeq 150$ MPa. Such values can be favourably compared with those obtained in sintered mullite,[52] even if they cannot compete with zirconium dioxide-toughened mullite.[57,58]

The use of additives, which can lead to vitreous phases which decrease the sintering temperature and which increase the room-temperature strength,[59] is another point requiring further study.

REFERENCES

1. Bowen, N. L. and Greig, J. W., The system Al_2O_3–SiO_2, *J. Am. Ceram. Soc.*, **7** (1924) 238.
2. Aramaki, S. and Roy, R., Revised phase diagram for the system Al_2O_3–SiO_2, *J. Am. Ceram. Soc.*, **45** (1962) 229.
3. Rooksby, H. P. and Partridge, J. H., X-ray study of natural and artificial mullites, *J. Soc. Glass Technol.*, **23** (1939) 338T.
4. Bárta, R. and Bárta, C., A study of the system Al_2O_3–SiO_2, *Zh. Priklad Khim.*, **29** (1956) 341.
5. Neuhaus, A. and Richartz, W., Über die Einkristallzuchtung und Zustandsverhaltniss von Mullit [Growing of single crystals of mullite and their constitution], *Ber. Deut. Keram. Ges.*, **35** (1958) 108.
6. Welch, J. H., A new interpretation of the mullite problem, *Nature*, **186** (1960) 545.

7. Bauer, W. H., Gordon, I. and Moore, C. H., Flame fusion synthesis of mullite single crystals, *J. Am. Ceram. Soc.*, **33** (1950) 140.
8. Toropov, N. A. and Galakhov, F. Y., New data for the system Al_2O_3–SiO_2, *Dokl. Akad. Nauk SSSR*, **78** (1951) 299.
9. Trömel, G., Comments on the equilibrium diagram Al_2O_3–SiO_2, in *Conference on Physical Chemistry of Iron and Steel Making*, MIT Press, Cambridge, Mass., 1956, 77–8.
10. Filonenko, N. E. and Lavrov, I. V., Fusion of mullite, *Dokl. Akad. Nauk SSSR*, **89** (1953) 141.
11. Trömel, G., Obst, K. H., Konopicky, K., Bauer, H. and Patzak, I., Untersuchungen im System SiO_2–Al_2O_3 [Investigation in the system SiO_2–Al_2O_3], *Ber. Deut. Keram. Ges.*, **34** (1957) 397.
12. Horibe, T. and Kuwabara, S., Thermo-analytical investigation of phase equilibria in the Al_2O_3–SiO_2 system, *Bull. Chem. Soc. Japan*, **40** (1967) 972.
13. Aksay, I. A. and Pask, J. A., Stable and metastable equilibria in the system SiO_2–Al_2O_3, *J. Am. Ceram. Soc.*, **58** (1975) 507.
14. Aramaki, S. and Roy, R., Revised equilibrium diagram for the system Al_2O_3–SiO_2, *Nature*, **184** (1959) 631.
15. Davis, R. F. and Pask, J. A., Diffusion and reaction studies in the system Al_2O_3–SiO_2, *J. Am. Ceram. Soc.*, **55** (1972) 525.
16. Aksay, I. A. and Pask, J. A., Diffusion in SiO_2–Al_2O_3 melts; for abstract see *Am. Ceram. Soc. Bull.*, **52** (1973) 710.
17. Aksay, I. A., Davis, R. F. and Pask, J. A., Diffusion in mullite ($3Al_2O_3 \cdot 2SiO_2$); for abstract see *Am. Ceram. Soc. Bull.*, **52** (1973) 710.
18. Schneider, S. J. and McDaniel, C. L., Effect of environment upon the melting point of Al_2O_3, *J. Res. Natl. Bur. Stand., Sect. A*, **71** (1967) 317.
19. Greig, J. W., Immiscibility in silicate melts: Part I, *Am. J. Sci.*, **13** (1927) 1; Part II, ibid. 133.
20. Schairer, J. F. and Bowen, N. L., The system K_2O–Al_2O_3–SiO_2, *Am. J. Sci.*, **253** (1955) 681.
21. Wahl, F. M., Grim, R. E. and Graf, R. B., Phase transformation in silica alumina mixtures as examined by continuous x-ray diffraction, *Am. Mineralogist*, **46** (1961) 1064.
22. Rana, A. P. S., Aiko, O. and Pask, J. A., Sintering of α-Al_2O_3/quartz, and α-Al_2O_3/cristobalite related to mullite formation, *Ceram. Int.*, **8** (1982) 151.
23. Nurishi, Y. and Pask, J. A., Sintering of α-Al_2O_3–amorphous silica compacts, *Ceram. Int.*, **8** (1982) 57.
24. Staley, W. G. and Brindley, G. W., Development of noncrystalline material in subsolidus reaction between silica and alumina, *J. Am. Ceram. Soc.*, **52** (1969) 616.
25. DeKeyser, W. L., Reactions at the point of contact between SiO_2 and Al_2O_3, in *Science of Ceramics*, Vol. II, Ed. G. H. Stewart, Academic Press, New York, 1963, 243–57.
26. West, R. R. and Gray, T. J., Reactions in silica–alumina mixtures, *J. Am. Ceram. Soc.*, **41** (1958) 132.
27. Ghate, B. B., Hasselman, D. P. H. and Spriggs, R. M., Synthesis and characterization of high purity, fine grained mullite, *Bull. Am. Ceram. Soc.*, **52** (1973) 670.
28. Metcalee, B. L. and Sant, J. H., The synthesis, microstructure and physical properties of high purity mullite, *J. Brit. Ceram. Soc.*, **74** (1975) 193.

29. McGee, T. D. and Wirkus, C. D., Mullitization of alumino-silicate gels, *Bull. Am. Ceram. Soc.*, **51** (1972) 577.
30. Mazdiyasni, K. S. and Brown, L. M., Synthesis and mechanical properties of stoichiometric aluminium silicate (mullite), *J. Am. Ceram. Soc.*, **55** (1972) 548.
31. Crofts, J. D. and Marshall, W. W., A novel synthesis of alumino-silicates and similar materials, *Trans. Brit. Ceram. Soc.*, **66** (1967) 121.
32. Murthy, M. K. and Hummel, F. A., X-ray study of the solid solution of TiO_2, Fe_2O_3, and Cr_2O_3 in mullite ($3Al_2O_3 \cdot 2SiO_2$), *J. Am. Ceram. Soc.*, **43** (1960) 267.
33. Sacks, M. D. and Pask, J. A., Sintering of mullite, in *Processing of Crystalline Ceramics, Materials Science Research, Volume II*, Eds Hayne Palmour III, R. F. Davis and T. M. Hare, Plenum Press, New York, 1978, 193–203.
34. Fenstermacher, J. E. and Hummel, F. A., High-temperature mechanical properties of ceramic materials: IV, sintered mullite bodies, *J. Am. Ceram. Soc.*, **44** (1961) 284.
35. Pankratz, L. B., Weller, W. W. and Kelley, K. K., *Low-temperature Heat-content of Mullite*, US Bur. Mines, Rept. Invest., 6287, 1963.
36. Kanzaki, S., Tabata, H., Kumazawa, T. and Ohta, S., Sintering and mechanical properties of stoichiometric mullite, *J. Am. Ceram. Soc.*, **68** (1985) C-6.
37. DeKeyser, W. L., Contribution to the study of sillimanite and mullite by x-rays, *Trans. Brit. Ceram. Soc.*, **50** (1951) 349.
38. Kriven, W. M. and Pask, J. A., Solid solution range and microstructures of melt-grown mullite, *J. Am. Ceram. Soc.*, **66** (1983) 649.
39. Risbud, S. H. and Pask, J. A., Mullite crystallization from SiO_2–Al_2O_3 melts, *J. Am. Ceram. Soc.*, **61** (1978) 63.
40. Moya, J. S. and Osendi, M. I., Effect of ZrO_2 (ss) in mullite on the sintering and mechanical properties of mullite/ZrO_2 composites, *J. Mat. Sci. Lett.*, **2** (1983) 599.
41. Dinger, T. R., Krishnan, K. M., Thomas, G., Osendi, M. I. and Moya, J. S., Investigation of ZrO_2/mullite solid solution by energy dispersive x-ray spectroscopy and electron diffraction, *Acta Met.*, **32** (1984) 1601.
42. Budnikov, P. P., Keshishyan, T. N. and Volkova, A. V., Effect of small additions on mullite formation at low temperatures, *Silikaty Okisly Khim. Vys. Temp.*, **1963** (1963) 233.
43. Johnson, S. M. and Pask, J. A., Role of impurities on formation of mullite from kaolinite and Al_2O_3–SiO_2 mixtures, *Bull. Am. Ceram. Soc.*, **61** (1982) 838.
44. Baudin, C. and Moya, J. S., Influence of titanium dioxide on the sintering and microstructural evolution of mullite. *J. Am. Ceram. Soc.*, **67** (1984) C-134.
45. Brownell, W. E., Subsolidus reactions between mullite and iron oxide, *J. Am. Ceram. Soc.*, **41** (1958) 226.
46. Skinner, K. G., Cook, W. H., Potter, R. A. and Palmour, H., Effect of TiO_2, Fe_2O_3, and alkali on mineralogical and physical properties of mullite-type and mullite-forming Al_2O_3–SiO_2 mixtures: I, *J. Am. Ceram. Soc.*, **36** (1953) 349.
47. Aksay, I. A., *Diffusion and Phase Relationship Studies in the Alumina–Silica System*, PhD Thesis, University of California, Berkeley, California, April 1973.
48. Ghate, B. B., Hasselman, D. P. H. and Spriggs, R. M., Kinetics of pressure-sintering and grain-growth of ultra-fine mullite powder, *Ceram. Int.*, **1** (1975) 105.

49. Dokko, P. C., Pask, J. A. and Mazdiyasni, K. S., High-temperature mechanical properties of mullite under compression, *J. Am. Ceram. Soc.*, **60** (1977) 150.
50. Brook, R. J. and Yangyun, S., Preparation of zirconia-toughened ceramics by reaction sintering, private communication, 1984.
51. Moya, J. S. and Osendi, M. I., Microstructure and mechanical properties of mullite/ZrO_2 composites, *J. Mat. Sci.*, **19** (1984) 2909.
52. de Portu, G. and Henney, J. W., The microstructure and mechanical properties of mullite–zirconia composites, *Trans. Brit. Ceram. Soc.*, **83** (1984) 69.
53. Mussler, B. H. and Shafer, W., Preparation and properties of mullite cordierite composites, *Bull. Am. Ceram. Soc.*, **63** (1984) 705.
54. Penty, R. A., Hasselman, D. P. H. and Spriggs, R. M., Pressure sintering kinetics of fine grained mullite by the change in pressure and temperature technique, *Bull. Am. Ceram. Soc.*, **52** (1973) 692.
55. Rogeaux, B. and Boch, P., Influence of an ultrasonic assistance to the powder compaction on the Weibull modulus of sintered alumina, *J. Mat. Sci. Lett.*, **4** (1985) 403.
56. Rodrigo, P. D. D. and Boch, P., *Mullite Ceramics by Reaction Sintering of Alumina–Silica Mixtures*, Internal Report, École Nationale Supérieure de Céramique Industrielle, Limoges, October 1984.
57. Boch, P. and Giry, J. P., Preparation and properties of reaction-sintered mullite zirconia ceramics, *Mat. Sci. Eng.*, **71** (1985) 39.
58. Claussen, N. and Jahn, J., Mechanical properties of sintered, *in situ*-reacted mullite–zirconia composites, *J. Am. Ceram. Soc.*, **63** (1980) 228.
59. Orange, G., Turpin-Launay, D., Goeuriot, P., Fantozzi, G. and Thevenot, F., *Mechanical Behaviour of a Al_2O_3–AlON Composite Ceramic Material (Aluminalon)*, Sci. Ceramics 12, Saint-Vincent, Italy, June 1983, 661–6.

Received 16 May 1985; amended version received and accepted 25 July 1985

Int. J. High Technology Ceramics **1** (1985) 31–58

Post-treatment of Pre-sintered Silicon Nitride by Hot Isostatic Pressing

G. Ziegler and G. Wötting

Deutsche Forschungs- und Versuchsanstalt für Luft- und Raumfahrt (DFVLR), Institut für Werkstoff-Forschung, D-5000 Köln 90, FRG

SUMMARY

The results of three different types of experiment are discussed: 1. Density, flexural strength and fracture toughness data at room temperature for different materials after post-hipping. The starting materials varied concerning the type and amount of sintering additive, as well as the pre-sintering conditions. 2. The post-densification behaviour by hipping of pre-densified starting materials, which were produced under well-defined conditions and in which various parameters were systematically changed: the residual porosity, the amount and viscosity of the liquid phase, and the silicon nitride phase composition ratio (α/β). 3. Results of model experiments: the behaviour of incorporated artificial macropores and cracks, as well as the change of the grain orientation in hot pressed silicon nitride (HPSN) with different degrees of texture.

Positive effects of post-hipping are a slight density increase, particularly the filling of residual macropores or the reduction of the pore size, and the enhanced healing of cracks. Negative effects may be grain coarsening and grain globularization, as well as surface defects caused by vaporization of the liquid phase and/or decomposition of silicon nitride during hipping. As a result, a marked increase of strength is not observed. However, the scatter of strength values can be reduced and fracture toughness is often improved. The latter observation seems to depend on a more intensive interlocking of the elongated β-Si_3N_4 grains, supported by local plastic deformation at the contact points of the grains. Which effect is dominant depends on the morphology and arrangement of the β-Si_3N_4 grains and the characteristics of the liquid phase in the starting pre-sintered materials, as well as on the hipping conditions.

Int. J. High Technology Ceramics 0267-3762/85/$03·30

1. INTRODUCTION

Hot isostatic pressing (hipping) is an advanced and promising processing technique which has become more and more important during the past years. The reason for this is that hipping combines the possibility of improving mechanical and thermo-mechanical properties with the possibility of producing complex-shaped components. Up to now this technique has been used for the processing of various material groups, e.g. metals and hard metals, and also ceramic materials such as some oxides, carbides and nitrides, as well as several composites.[1-3] Many applications showed that not only the physical and mechanical properties of these materials but also those of the ceramic components may be improved, reliability increased and costs reduced compared with conventional processes. Based on these positive results, it was thought that hipping was also a suitable method for the production of ceramic components made from high-temperature structural materials such as silicon nitride. For this reason, during the past years special hipping equipment has been developed to allow hot isostatic pressing at temperatures higher than 1700 °C.[1-3]

In the case of silicon nitride, several advantages are expected from this technique. As for other ceramic materials, the main advantage for silicon nitride is that the nearly net-shaping possibility eliminates post-machining of the densified part, except for surfaces with extremely close tolerances. Thus, this technique offers a potential for the production of advanced ceramic components. Besides that, material properties are expected to be improved; for example, the uniform way of applying the high pressure results in fully isotropic material properties. The pressure increase by more than one order of magnitude over uniaxial hot-pressing enhances the densification process of silicon nitride. As a result, dense silicon nitride parts with powder compositions containing only small amounts of consolidation aids, or with more refractory additives, may be produced. Furthermore, the high pressure applied is thought to result in a more uniform and fine-grained microstructure under optimized hot isostatic pressing conditions, which may lead to improved strength. Healing of cracks under high pressure can result in an additional improvement both of the absolute values and of the reduced scatter of mechanical properties. Moreover, this technique gives the opportunity of joining silicon nitride parts produced by different techniques (diffusion bonding or gas pressure bonding). Therefore, hipping offers the possibility of producing near net-shaped components and a good opportunity for further improvement of the strength and high-temperature properties, as well as a reduction of the scatter of properties.

During hipping high pressure is applied via a gas to consolidate a porous compact after canning, or to remove the residual porosity from pre-sintered

uncanned materials, which contain only closed pores. In the case of silicon nitride, the latter technique of post-treating pre-sintered silicon nitride by post-hipping is not yet well understood. Open questions are, in particular, the influence of microstructural characteristics of the pre-sintered materials, the influence of the type and amount of additives, and the influence of defect healing on the mechanical properties of the hipped materials. This paper attempts to answer these questions. In this context the results of three types of experiments are presented:

1. Density, flexural strength and fracture toughness data at room temperature for different materials after post-hipping. The starting materials varied concerning the type and amount of sintering additives, as well as the pre-sintering conditions.
2. The post-densification behaviour by hipping of pre-densified starting materials which were produced in the laboratory under well-defined conditions and in which various parameters were systematically changed: the residual porosity, the amount and viscosity of the liquid phase, and the silicon nitride phase composition ratio (α/β).
3. Results of model experiments: the behaviour of incorporated artificial macropores and cracks (induced by Knoop hardness indentation), as well as the change of the grain orientation in hot pressed silicon nitride (HPSN) with different degrees of texture.

2. HOT ISOSTATIC PRESSING OF SILICON NITRIDE

In order to produce nearly dense ceramic parts from silicon nitride via the hipping technique, three routes can be followed (Fig. 1):

(i) Hipping of silicon nitride powder compacts, moulded by any appropriate technique to the final shape; the shrinkage occurring during densification, however, has to be considered.
(ii) Hipping of reaction bonded silicon nitride (RBSN), also preformed to the final shape, taking into account shrinkage; this means starting with silicon powder and producing RBSN in a first step.
(iii) Hipping treatment of sintered silicon nitride (SSN) or sintered reaction bonded silicon nitride (SRBSN) as starting material. The two steps, sintering and hipping, were combined into one sinter-hipping cycle.

For all three techniques a certain amount of consolidation aid has still to be added in most cases. Using the first two techniques, the starting material has to be coated with a temperature- and pressure-resistant barrier against the high-pressure gas, to prevent the gas penetrating into the porous body. The starting material for the third technique usually has almost no open porosity, which makes encapsulation unnecessary.

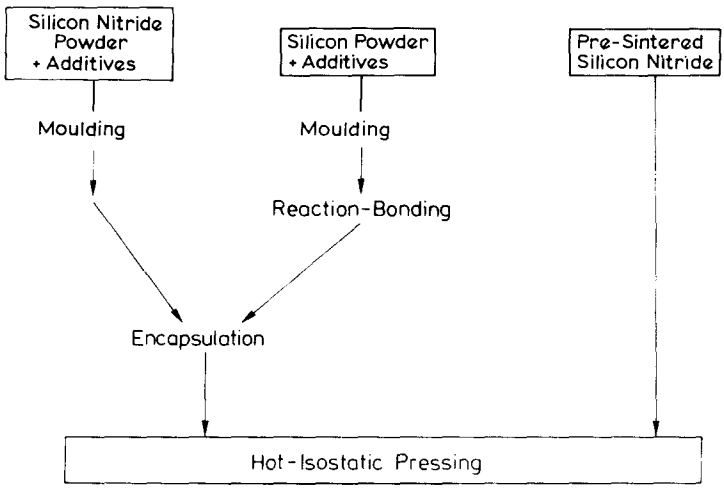

Fig. 1. Different routes for hipping silicon nitride.

Though hipping is a promising technique and many workers have started activities in this field, only a few papers have been published up to now. As this technique, however, is undergoing rapid development, important results are to be expected during the next few years.

The state of the art may be summarized as below.

2.1. Encapsulation

The encapsulation ('canning') of complex-shaped components, particularly parts with sharp edges and corners, still presents serious problems.[4-7] Different prerequisites for successful canning need to be fulfilled:

- The encapsulation material must have sufficient thermal stability at the hipping temperature, but is simultaneously required to have a certain amount of plasticity in order to transfer the applied gas pressure uniformly to the part to be consolidated. This restricts the selection of materials to refractory metals (tantalum, molybdenum, tungsten), glasses with high softening temperatures (silica glass, 'vycor' glass), or certain ceramic materials.
- Chemical reactions between the capsule and the ceramic parts must not occur; this often requires an additional barrier layer.
- The coefficients of thermal expansion of the container material and the material to be consolidated have to match well in order to avoid cracking during heating and cooling.
- Decapsulation of the densified parts has to be mechanical or chemical without any damage to the parts.

Geometrically simple-shaped components (discs, bars, etc.) may be encapsulated in glass tubes or metal containers, which are sealed off by softening or welding under vacuum. For more complex parts other methods are necessary. For example, small parts like turbine blades may be encapsulated in glass tubes or metal containers under vacuum. However, to avoid tearing-off or other damage to the glass layer at the thin, sharp trailing edges of the blades, such parts were additionally embedded into a powder, e.g. boron nitride.[8,9] This powder acts as a pressure transmitter and simultaneously prevents chemical reactions and the building up of thermal stresses due to differences in expansion characteristics between the part to be consolidated and the capsule material ('powder-bed-canning technique'). Furthermore, decapsulation is easy and subsequent machining may often be avoided. For example, this technique has been applied to produce turbine blades for rotors with a metallic hub.[9]

For the production of larger, more complicated parts like turbo-chargers or monolithic turbine rotors, possible encapsulation methods comprise, up to now, the construction of equally complex metal housings,[3,10] the 'glass-particle-canning technique'[4,5,11,12] or the 'sinter-canning technique'.[6,13,14] The first one is a very costly method as refractory metal sheets have to be welded. In the second method, the 'glass-particle-canning technique', the ceramic part is coated with one or more layers of glass particles and is heated up under vacuum until the glass (or one layer of glass) softens, thus sealing off the body. This method has been applied especially in Sweden. It has been reported that complete turbine rotors, shaped by injection moulding of silicon nitride powders, have been produced of near theoretical density without subsequent machining.[4,5,11,15] The third method, the 'sinter-canning technique', comprises coating of the parts with a fine-grained ceramic powder or powder mixture, which is sintered under vacuum to gas tightness. It is relatively easy to adjust similar thermal expansion characteristics of the capsule and the silicon nitride part by using silicon nitride powders for the capsule. In order to prevent any reaction between the layer and the silicon nitride component, an interlayer may be used. This technique was, for example, successfully applied to the consolidation of cutting tools, turbine blades and monolithic rotors made from RBSN.[9,14,16]

2.2. Processing routes and material properties

The first two routes for hipping (see Fig. 1) show large differences in the shrinkage of the components. Starting with silicon nitride powder compacts, which usually have a green density of about 2·0 $Mg\,m^{-3}$ (i.e. about 60% theoretical density) after moulding, results in a volume shrinkage of nearly 40%. With RBSN the starting density may be up to about 2·6 $Mg\,m^{-3}$

(~80% theoretical density). As a result, the volume shrinkage during hipping is much lower. The linear shrinkage of only 6–7% facilitates the production of complex-shaped components with close dimensional tolerances. This relatively low shrinkage is one advantage of the second route. Besides this, the combination of the easy shaping possibility of RBSN and the high strength data of dense silicon nitride is a further advantage of this technique.

For the hipping of silicon nitride powder compacts, the results show that density and mechanical properties are dependent on the purity of the starting powder and the type and amount of consolidation additive.[4,5,17–20] Using commercial silicon nitride powders, density values higher than 94% theoretical density were achieved without any additives. In this case the density of hot isostatically pressed silicon nitride (HIPSN) is dependent on the characteristics of the silicon nitride starting powder, primarily on the phase composition and the impurity content. Using highly pure silicon nitride powder,[20] the maximum density achieved was 94% theoretical density, but self-bonding between the grains was weak; in the case of starting materials containing a relatively high amount of impurity, complete densification was reached. To obtain fully dense materials with high-purity silicon nitride powders, only small additions of sintering aids are necessary. Mechanical properties are completely isotropic. High room-temperature strength data and high values of the Weibull modulus, m, have been observed. Improved high-temperature strength and creep behaviour were found. Nevertheless, it has not been possible up to now to develop materials with high room-temperature strength and simultaneously excellent high-temperature properties. Parts of cylindrical, conical and flat sections, and also complex-shaped components for gas turbines, have been fabricated to final shape without any or little post-machining. It has been reported[3,4] that the tolerances of the finished products are rather good and that shaped parts can be processed with tolerances and surface quality acceptable even for turbine blades.

Using a suitable encapsulation technique with the hipping of RBSN, fully dense materials have been achieved, even with low amounts of additives. Compared to hot-pressed materials and/or sintered grades, the yttrium oxide doped and hipped materials displayed similar or even superior high-temperature properties.[6,8,9,16,21]

Applying the 'sinter-canning technique' to RBSN, cutting tools, turbine blades, welding nozzles and monolithic rotors have been produced. Now the goal has to be to transfer the material properties, which have already been achieved in test specimens, to complex-shaped components, and to develop economical production techniques.

Because of the technical problems associated with the encapsulation

technique and the relatively high costs in mass production, the third route, the post-treatment of pre-sintered silicon nitride by hipping without using a container, may be expected to gain wide acceptance on a short-term basis. This route, especially the combined sinter–hipping technique, is thought to be promising for the future and will therefore undergo rapid development supported by further progress in the sintering techniques. Up to now only a few results have been reported which indicate that the hipping of pre-sintered silicon nitride is strongly dependent on various microstructural characteristics of the sintered starting materials (density, grain size, grain morphology, grain boundary characteristics). Results of some systematic investigations have been published by a Japanese group.[7,22,23] These experiments were carried out in the temperature range between 1700 and 1900 °C under a pressure of 100 MPa using argon or nitrogen. Some interesting results were achieved; a density increase was only observed if the density of the pre-densified silicon nitride was higher than about 93% theoretical density. In any case, nitrogen as pressure gas led to higher densities and higher strength values compared to an argon atmosphere because high nitrogen gas pressure suppresses the decomposition of silicon nitride. One of the reasons for the strength reduction after argon hipping is thought to be a formation of pores, especially near the specimen surface. After nitrogen hipping the improvement in strength for some materials was accompanied by an increase in Weibull modulus. The strength after hipping was dependent on the type of pre-sintered silicon nitride. The α/β-silicon nitride phase composition and the grain morphology of the pre-densified material seem to be decisive parameters for improving strength values. It is thought that a certain amount of α-phase and the existence of needle-like crystallites in the pre-sintered starting materials are necessary to improve the strength by nitrogen hipping. Moreover, the improvement in strength depends not only on the sintering conditions but also on the process parameters during hipping (type of gas, pressure, temperature, time). In addition, healing of relatively large internal defects, originated during cold-pressing or sintering, was observed after nitrogen hipping.

Recent investigations of the authors about fracture strength, fracture toughness and microstructural changes after post-hipping of pre-sintered silicon nitride permit the conclusion to be drawn that the microstructure of the pre-sintered starting materials and the healing of cracks and flaws are key parameters in the post-hipping process.[24,25]

There is one more point which should be discussed here: the solution of nitrogen during post-hipping. Following the third route, the high-pressure gas directly contacts the pre-sintered materials. Thus, solution of gas molecules in the silicon nitride compact is a possible phenomenon. So, for sintered silicon nitride containing 2·2 wt% aluminium oxide, 1·3 wt% magnesium oxide and 2 wt% silicon dioxide as densification aids, an

increase in nitrogen of 0·6 wt % (and a decrease in oxygen content) was observed during hipping when the specimens were kept in a graphite crucible at 126 MPa and 1750 °C for 14 h.[26] The density increased slightly and the strength was improved. The authors think that nitrogen gas dissolves in the silicon nitride compact, which contains a liquid phase, and that nitridation of the silicon dioxide component takes place during hipping when the cycle runs for 10 h or more. The density increase after long soaking, and the improvement of strength, too, are thought to be partly caused by this effect. When heating up these specimens to high temperatures under atmospheric pressure, the dissolved nitrogen may be released, which results in the formation of pores.

2.3. Densification mechanism and microstructural development

The basis for the discussion of the properties of hipped materials is the understanding of the densification mechanism and the microstructural development. As for sintering and hot-pressing, densification by hipping occurs by a liquid phase sintering process involving rearrangement, solution–diffusion–reprecipitation and coalescence. However, the contribution and the rate of the different densification steps are changed by the application of pressure. Moreover, by enhancing different processes during densification, like dissolution, formation of β-nuclei and growth of β-silicon nitride crystals, fine-grained microstructures can be achieved. Thus, the microstructure of these HIPSN materials consists mainly of the two hexagonal phases α- and β-silicon nitride and a largely amorphous silicate or nitride oxide grain boundary phase (5 to 20 vol %), which is arranged in thin layers of about 1–5 nm thickness and in larger concentrations at grain triple junctions. One typical feature of all dense silicon nitride materials is the difference in the grain morphology; the α-grains are equiaxial ($\sim$0·1 to 2 μm), the β-silicon nitride phase reveals an elongated grain structure ($\sim$ 5 to 10 μm) with aspect ratios (= length to thickness ratios) of between 5 and 10.

The processes taking place during post-hipping of pre-sintered materials, however, are not yet completely understood. It seems that grain rearrangement is possible by grain-boundary sliding, that solution may occur at the highly stressed particle contact points, and that coalescence processes may take place.

3. EXPERIMENTAL PROCEDURE

3.1. Sample preparation

Besides samples which were prepared for systematic sintering studies and which contain different types and amounts of sintering additive (for details

see Refs 24 and 25), various sets of starting materials and special pre-treated samples were prepared for hipping experiments. With these sets an attempt was made to evaluate parameters which determine the densification behaviour during hipping and to obtain information about the processes and mechanisms that are effective. These materials are characterized in Table 1.

In order to study the influence of the density of the starting material on the final density after hipping, sets of materials with different levels of density were prepared by compaction-limited hot-pressing (set I). Additionally, the influence of high and low amounts of sintering additive to the starting powder composition was investigated. The influence of the silicon nitride phase composition ratio α/β was studied with materials which were prepared by varying the hot-pressing time (set II).

In set III artificial pores were introduced by incorporating disc-shaped wax particles at a distance from the surface of about one-third of the specimen width. The average diameter of the pores was about 500 μm. These experiments were conducted with two materials, again with different

TABLE 1
Starting Materials for Hipping Experiments

Set	*Objective*	*Variations*	*Processing*
Systematic investigations			
I	Influence of starting density and additive concentration	– Starting density ~95 – ~98 % theoretical density – Additive amount low → high – Softening temperature low → high	Compaction-limited hot-pressing
II	Influence of α/β-phase composition	α-content ~70 – ~10 %	Varying of hot-pressing time
Model experiments			
III	Filling of pores	Additive amount low → high	Incorporation of an artificial 500 μm pore, sintering
IV	Rearrangement/change of grain orientation in HPSN	– Additive amount/ softening temperature low → high – α-content ~70 – ~0 %	Hot-pressing
V	Healing of cracks	Additive amount/ softening temperature low → high	Hot-pressing, Knoop hardness indentation

amounts of additive in order to change the characteristics of the liquid phase: 5 wt% yttrium oxide + 1·1 wt% aluminium oxide and 15 wt% yttrium oxide + 3·4 wt% aluminium oxide.

To study the rearrangement of the β-silicon nitride grains during post-hipping, hot-pressed materials with different types and amounts of additive were prepared, which showed large differences in orientation.[27] In all materials complete $\alpha \rightarrow \beta$-silicon nitride phase conversion had occurred (set IV).

Crack healing effects were studied with specimens where artificial cracks were introduced by Knoop hardness indentation (load 50 kg). The damaged surface zone was removed before hipping. The experiments were carried out with two materials fluxed with different additives: 5 wt% yttrium oxide and 8 wt% yttrium oxide + 2 wt% aluminium oxide + 4 wt% silicon dioxide, respectively (set V).

3.2. Hot isostatic pressing

The pre-sintered materials were post-treated by hipping without canning. Only one set of specimens was encapsulated before hipping. The pre-sintered samples were hipped in a boron nitride crucible. Boron nitride powder was used to prevent reaction between the specimens. In most cases hipping was carried out in the small-scale hipping equipment, 'HIP 2000' of National Forge, in nitrogen; some experiments were performed in the ASEA press 'QIH32' in argon. The temperature was varied between 1750 and 1980 °C. In all cases a pressure between 180 and 200 MPa was applied.

3.3. Characterization methods

Materials were characterized before and after hipping by density measurement, X-ray diffraction (silicon nitride phase analysis, orientation for different hot-pressed silicon nitride materials) and microstructural analysis, as well as by fracture strength and fracture toughness measurements. Quantitative microstructural analysis was performed on etched microsections. Following the method described in Refs 25 and 28, the thickness, $\bar{d}$, and length, $\bar{l}$, of the elongated β-silicon nitride grains were measured and the aspect ratio, $\bar{a} = \bar{l}/\bar{d}$, was determined.

Fracture strength was determined with specimens (3·5 × 4·5 × 45 mm) in 4-point bending (span 10/20/10 mm). Fracture toughness was measured by the Vickers hardness indentation technique, applying a 20 kg load and using the equations:[29]

$$K_{Ic} = 0{\cdot}111 \times P \times b^{-1{\cdot}5}; \qquad b = \frac{(\Sigma \bar{l} + 2\bar{d})}{4}$$

The size and location of the artificial pores in the starting material, as well as in the post-hipped samples, were determined by a microradiographic method, described in Ref. 30. The size of the induced cracks by Knoop hardness indentation was analysed using a procedure described in Ref. 31.

4. EXPERIMENTAL RESULTS

4.1. Summary of results of various post-hipping treatments

Figures 2, 3 and 4 summarize the data of density, flexural strength and fracture toughness at room temperature for different materials which were prepared and post-hipped. These materials contain different types and amounts of consolidation additives and were pre-densified by pressureless sintering or by hot-pressing using various processing conditions. These data indicate some results which have been achieved by applying post-hipping to various pre-densified silicon nitride materials.

Figure 2 gives the density values after hipping as a function of the density of the starting material. For most materials an increase in density is observed, which ranges for the materials with $\rho > 90\%$ theoretical density from 0 to a maximum of 5%. The average density increase for these

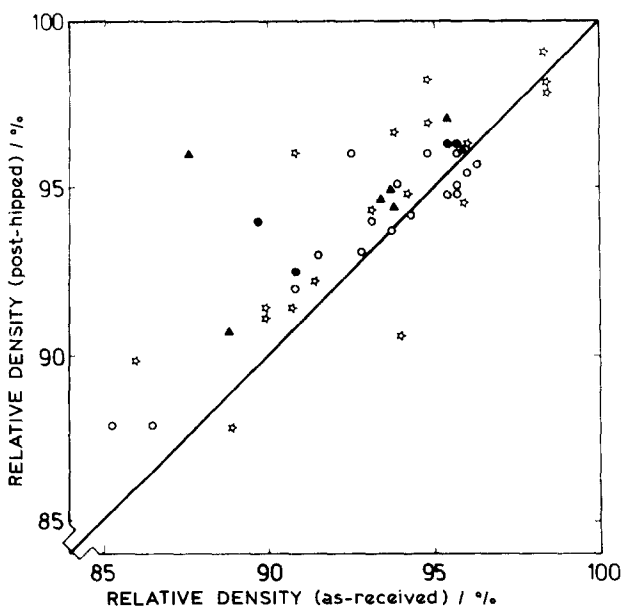

Fig. 2. Density values of post-hipped materials as a function of the relative density of the starting materials. ○, Argon; ●, encapsulated; ▲, argon + powder bed; ☆, nitrogen.

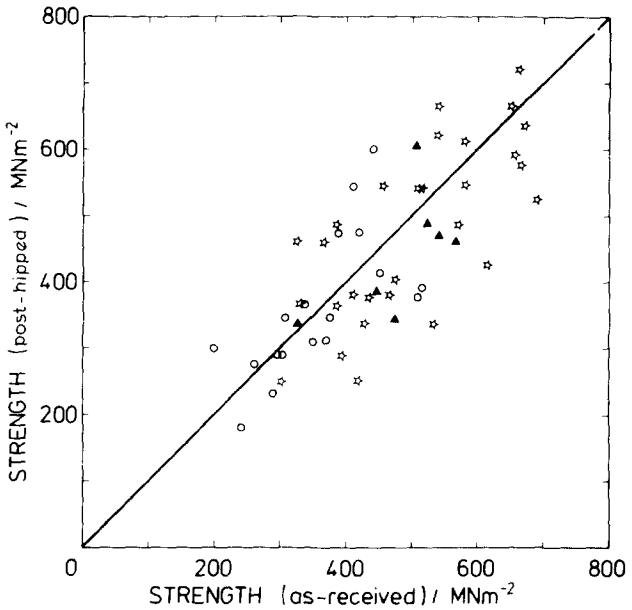

Fig. 3. Flexural strength data of post-hipped materials as a function of the strength values of the starting materials. ○, Argon; ▲, argon + powder bed; ☆, nitrogen.

pre-sintering conditions, however, is only about 1·1·5%. In no case is the theoretical density approached. Here it should be noted that a decrease or only a slight increase in density was observed for hipping in argon but also in some cases for hipping under high pressure nitrogen for some relatively dense materials. The reasons for this are the decomposition of silicon nitride in argon, and the vaporization of the liquid phase in the surface area of relatively dense materials or from the bulk of less dense silicon nitride grades (which still exhibit open porosity) due to the high hipping temperatures. The amount of vaporization mainly depends on the quantity and composition of additives (not shown here) which determine the properties of the liquid phase, especially its refractoriness. In contrast to this density reduction, a density increase can be observed in some cases with materials which still reveal a certain amount of open porosity. These materials contain additives which lead to further sintering at the hipping temperatures ($T_{hip} > T_s$).

Figure 3 summarizes the flexural strength data before and after hipping. These data indicate that an improvement of strength, but also a strength degradation, can be obtained, independent of the strength level of the starting material. Figure 4 shows the fracture toughness values before and after hipping. Also in this case, an increase but also a reduction in fracture toughness was observed for different materials. Here it is interesting to note that the K_{Ic} values of those materials that already had a relatively high K_{Ic} value in the pre-sintered state are clearly increased.

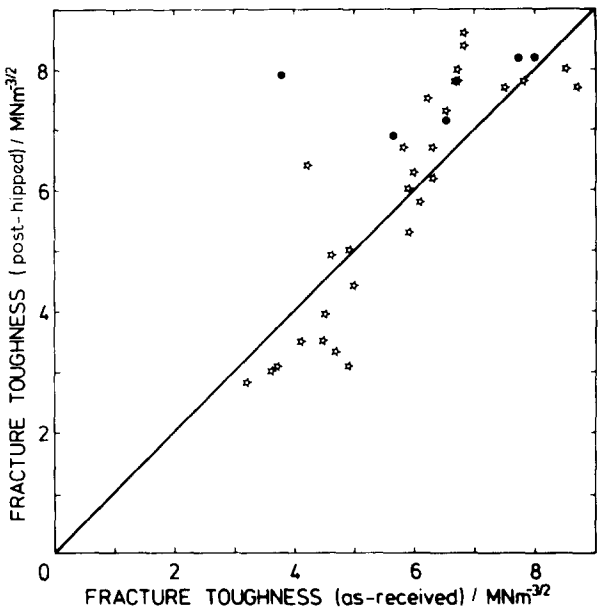

Fig. 4. Fracture toughness data of post-hipped materials as a function of the fracture toughness values of the starting materials. ●, Encapsulated; ☆, nitrogen.

As an example, Fig. 5 shows changes in density, flexural strength and fracture toughness by post-hipping of various materials, in relation to the additive composition. This demonstrates that neither are the property changes simply related to the type and amount of additive.

In order to interpret these results, some systematic investigations and model experiments were carried out (see Table 1) to evaluate the influence of certain characteristics of the starting material on the post-densification behaviour by hipping.

4.2. Results of systematic investigations

4.2.1. Influence of the density of the pre-sintered starting materials

Figure 6 shows the influence of the density of the starting material on the final density after post-hipping for two material groups with 1 and 5 wt% yttrium oxide (set I, Table 1), i.e. different amount and viscosity of the liquid phase. Each material group was prepared with a starting density $<95\%$ and $>95\%$ theoretical density. These results demonstrate that a density increase can only be observed if the starting materials contain no open pores. In the case of the 1% yttrium oxide fluxed sintered silicon nitride, the change from open to closed porosity occurs at about 94% theoretical density. Below this value a decrease in density takes place, probably

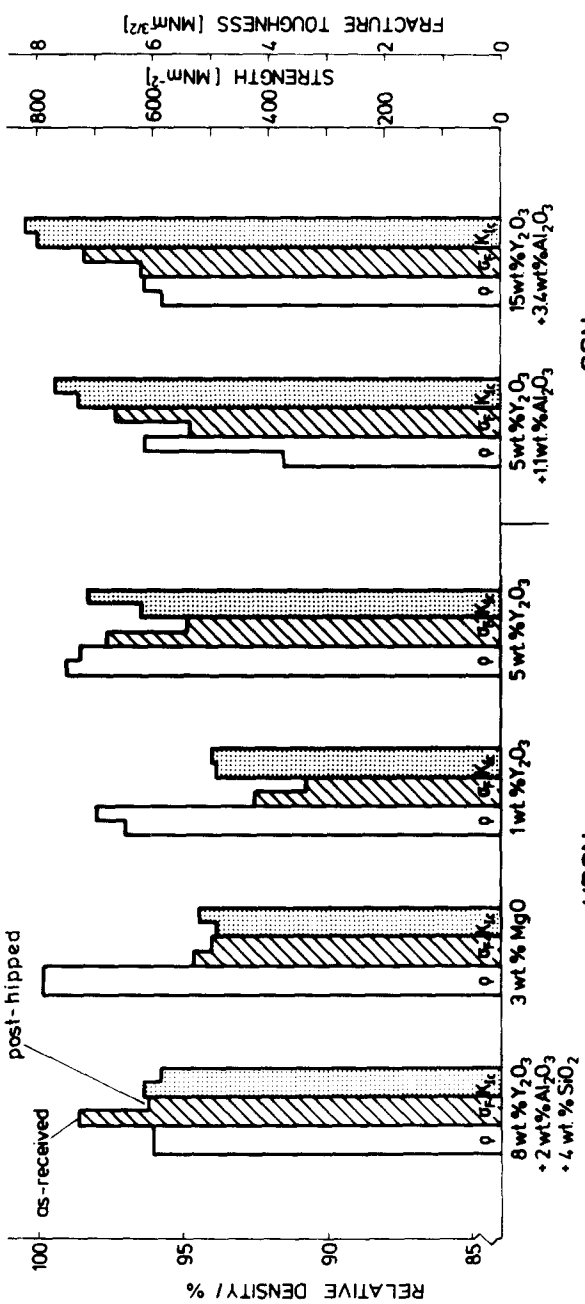

Fig. 5. Changes in density (ρ), fracture strength (σ_F) and fracture toughness (K_{Ic}) by post-hipping of various materials containing different amounts of additive.

caused by the vaporization of the liquid phase. Here, however, it should be mentioned that the density at which a material changes from open to closed porosity cannot be specified accurately because the theoretical density of the materials is usually not known exactly due to insufficient knowledge of the density of the secondary phases. The density increase for the high-density materials is about 1–1·5% of theoretical density. For many materials investigated the density gains get smaller as the density of the starting materials approaches the theoretical density. In no case was the theoretical density reached for materials pre-sintered in nitrogen.

For purposes of comparison, Fig. 6 (left) presents the densification behaviour of a pre-sintered low-density material by post-hipping, which was encapsulated. In this case, nearly theoretical density was achieved. The high densification was caused by a real pressure-assisted sintering effect, similar to the densification process occurring during hot isostatic pressing of powder compacts or RBSN, and probably by the control of the equilibrium partial pressure of all components, thus avoiding vaporization.

As can be seen from Fig. 6, the amount of additive does not markedly influence the post-hipping behaviour. To prove this, samples with different amounts of additives were prepared in order to obtain an increasing viscosity of the liquid phase. Again, two groups of materials were used, the

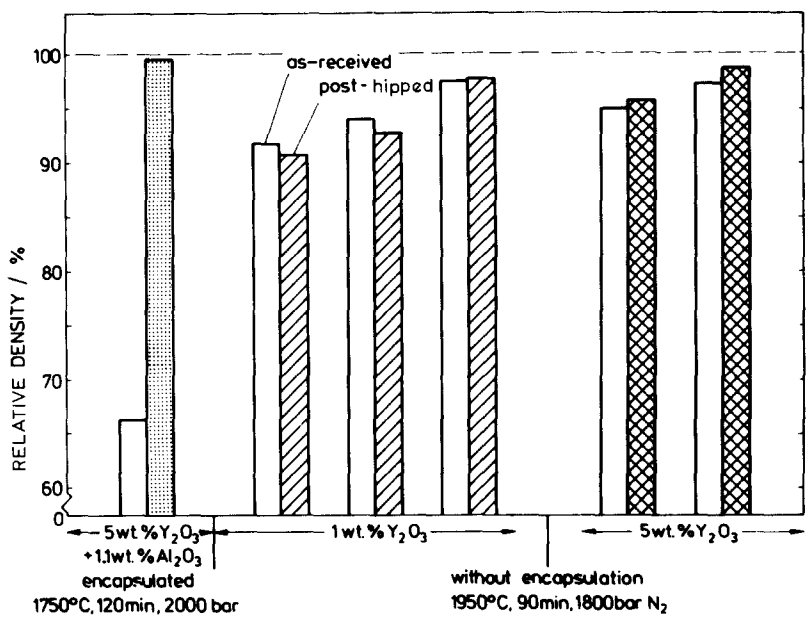

Fig. 6. Influence of the density of the starting materials on the final density after post-hipping for two materials with different amounts of yttrium oxide (for comparison, the final density of an encapsulated low-density starting material is given on the left).

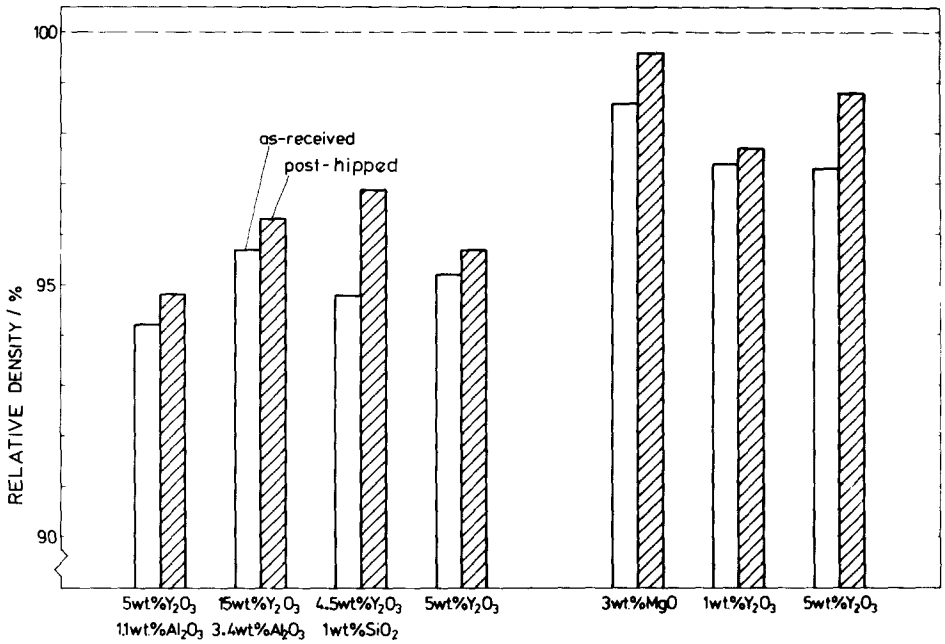

Fig. 7. Density values before and after post-hipping for materials with different type and amount of additive, arranged for two groups of similar starting density values.

first with a starting density of about 95 % theoretical density and the second with about 98 % theoretical density. The results are summarized in Fig. 7. The viscosity of the liquid phase is thought to increase within each group from left to right. These results again show neither a relation of the post-densification behaviour to the viscosity of the liquid phase nor to its quantity. Therefore, the conclusion may be drawn that besides density other microstructural characteristics exert a strong influence on the post-densification behaviour, whereas the amount and viscosity of the liquid phase is of secondary importance.

4.2.2. Influence of the silicon nitride phase composition ratio (α/β) in the pre-densified starting materials

Figure 8 shows the influence of the silicon nitride phase composition ratio (α/β) of pre-densified magnesium oxide fluxed starting materials on the final density and phase composition ratio, as well as on flexural strength and fracture toughness after hipping at 1850 °C in nitrogen (set II, Table 1).

The density of the hot-pressed starting materials increases slightly with higher β-phase content. The final density of all post-hipped materials rises by about 0·02 $Mg\,m^{-3}$ and is independent of the β-phase content of the starting materials. The β-phase content of the post-hipped materials is dependent on the phase composition of the starting material. Only for high

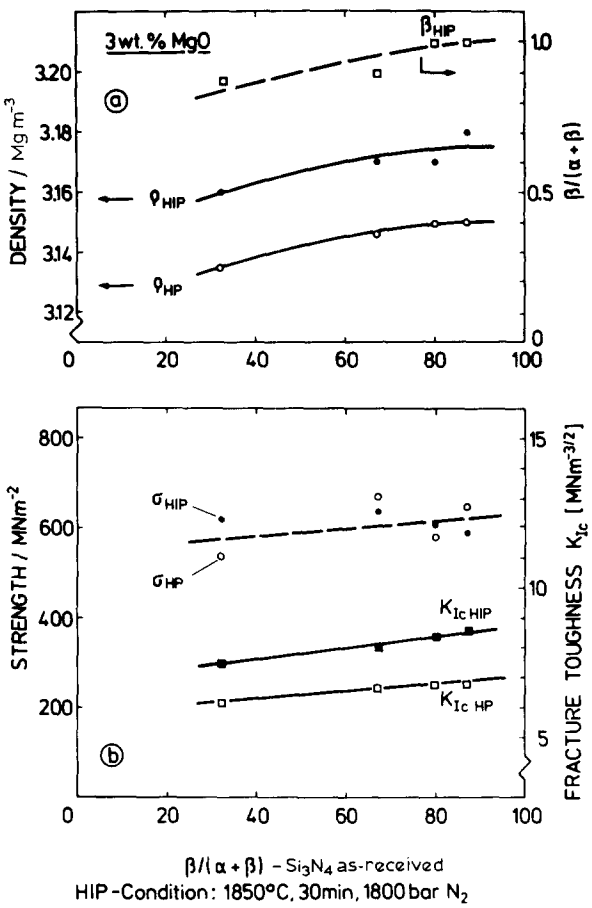

Fig. 8. Influence of silicon nitride phase composition ratio (α/β) of hot-pressed magnesium oxide fluxed (3 wt %) starting materials on: (a) final density (ρ_{HIP}) and phase composition ratio (α/β) (ρ_{HP} = density of the starting material); and (b) fracture strength and fracture toughness of post-hipped materials.

β-phase content in the pre-densified specimens does complete phase transformation occur during hipping under these conditions.

Fracture toughness increases for all materials after post-hipping. A slight improvement of K_{Ic} with higher β-phase content in the pre-densified materials was observed; this means that there is the same tendency as in the starting material. The strength data reveal no change.

4.3. Model experiments

4.3.1. Incorporation of artificial pores

The results given above show that in nearly all materials with closed porosity a slight reduction in total porosity was achieved by post-hipping. In order to

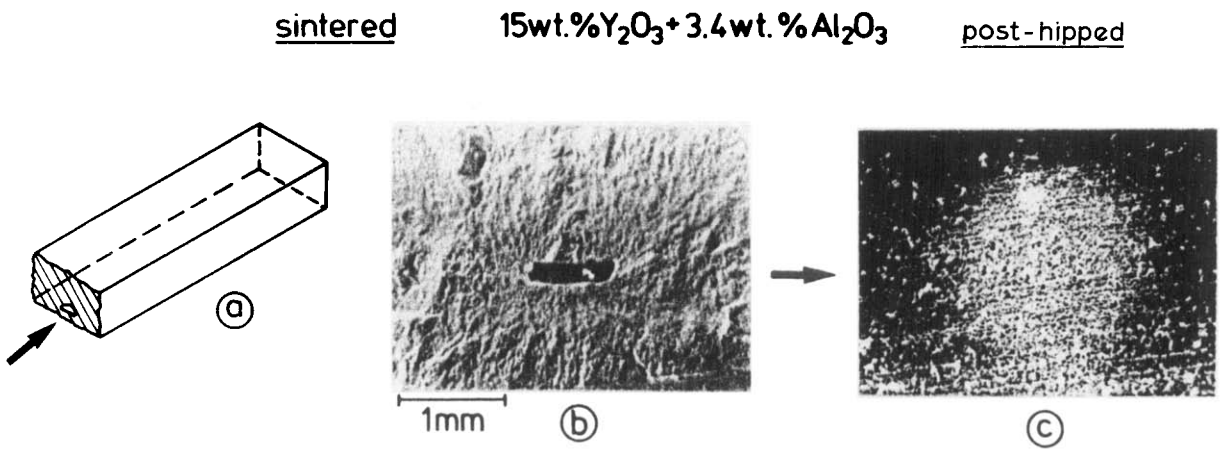

Fig. 9. Incorporation of artificial pores. (a) Location of pore (schematic); (b) artificial pore in the fracture surface; (c) pore filling detected in the cross-section.

study the mechanisms of porosity reduction, artificial pores were introduced (Fig. 9, set III, Table 1). These experiments were carried out with two materials containing different additive compositions, i.e. with different amount and characteristics of the liquid phase: 5 wt% yttrium oxide + 1·1 wt% aluminium oxide and 15 wt% yttrium oxide + 3·4 wt% aluminium oxide. In the case of a high amount of liquid phase, complete filling of the artificial pore was observed (Fig. 9(c)) as determined by microradiographic and SEM evaluation. The material in these pores is characterized by very fine grains, lower hardness and a somewhat higher silicon/yttrium ratio compared to the characteristics of the matrix. However, in the case of the material with a lower amount of liquid phase, the large artificial pore was not filled completely. This means that the effect of pore filling is dependent on the amount and probably on the viscosity of the liquid phase.

4.3.2. Influence of post-hipping on the grain orientation of hot-pressed materials

Though the elimination of residual macropores by the reduction of pore size occurs during post-hipping, the question still remains why, in most cases—even for as-received materials with residual α-phase content—complete densification cannot be achieved. A possible answer is that during post-hipping of pre-densified materials no essential rearrangement of the elongated β-Si_3N_4 grains takes place and, consequently, the reduction of porosity is limited ('bridge effect'). Thus, the microstructure and the pore structure of the post-hipped materials are mainly controlled by the microstructure of the starting materials (characteristics of the liquid phase and arrangement of the β-Si_3N_4 grains).

This hypothesis was proved by post-hipping HPSN with different types and amount of additive (set IV, Table 1). It is well known that hot-pressed materials exhibit a strong grain orientation. The reason for this is that the elongated β-Si_3N_4 grains crystallize during hot-pressing in such a way that their direction of elongation, which coincides with the crystallographic *c*-axis of the hexagonal β-phase, is oriented perpendicular to the hot-pressing direction. This preferred orientation results in a pronounced anisotropy of strength, fracture toughness and thermal properties.[32] The orientation effect was found to be dependent on the type and amount of additive.[27] This is demonstrated in Fig. 10 for materials with different magnesium oxide and yttrium oxide concentrations. In this graph the orientation effect is indicated by the X-ray intensity ratio $I(200)/I(002)$ of the hexagonal β-Si_3N_4 phase. This figure also demonstrates that post-hipping does not result in any marked change of the β-Si_3N_4 grain orientation. Only if starting materials with high residual α-Si_3N_4 phase are post-hipped (Fig. 11) does the average

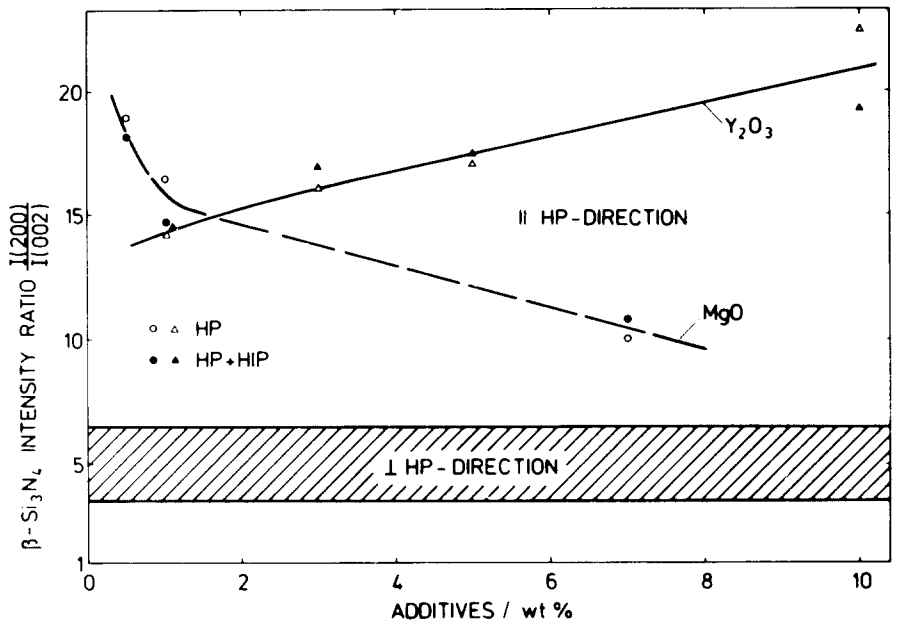

Fig. 10. Influence of post-hipping on the grain orientation of hot-pressed materials ($\beta/(\alpha+\beta)=1$): β-Si_3N_4 intensity ratio $I(200)/I(002)$ as a function of the additive concentration for hot-pressed (HP) and post-hipped (HP + HIP) materials. ||HP: measured parallel to the hot-pressing direction. ⊥HP: measured perpendicular to the hot-pressing direction.

orientation become smaller after hipping, because the newly-formed β-Si_3N_4 grains precipitate without orientation, due to the isotropic pressure.

4.3.3. Introduction of artificial cracks and crack healing experiments

In order to study the effect of enhanced crack healing during hipping, two materials with large differences in the viscosity of the liquid phase were pre-cracked using the Knoop hardness indentation technique and the flexural strength was measured before and after hipping (set V, Table 1). Figure 12 shows the fracture strength for two materials fluxed with 5 wt% yttrium oxide (high viscosity of the liquid phase) and yttrium oxide + aluminium oxide + silicon dioxide additives (low viscosity of the liquid phase) in the uncracked and pre-cracked as-received state. Hipping results in an improvement of the fracture strength of both pre-cracked materials. The strength data are only limited by decompositional effects during hipping, as can be seen from the strength reduction of the uncracked material.

One important effect of post-hipping is the reduced scatter of strength data. This is demonstrated in Fig. 13 for three hot-pressed materials which were very badly machined. The improvement in data scatter after hipping is mainly caused by the healing of cracks; however, the elimination or reduction of residual pores may additionally contribute to this effect.

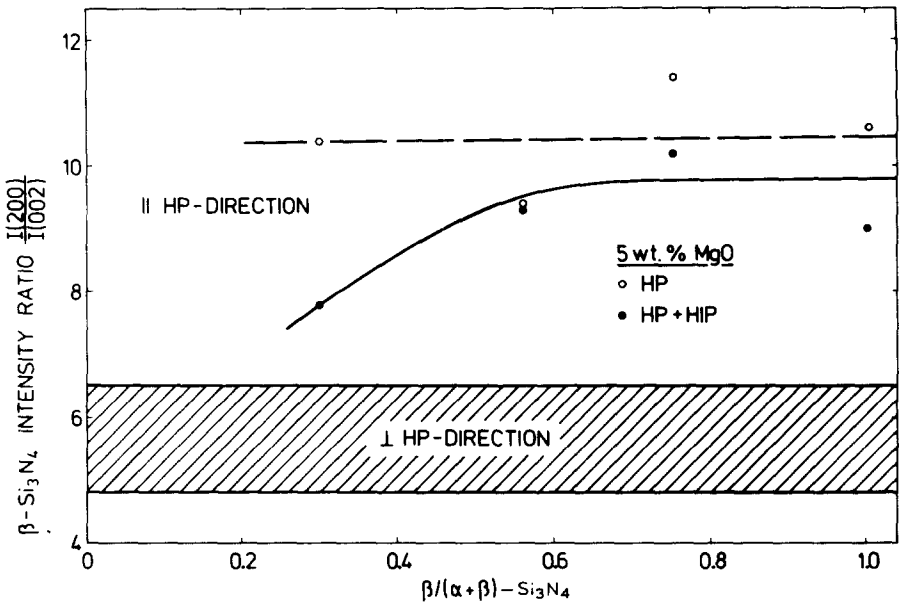

Fig. 11. Influence of post-hipping on the grain orientation of hot-pressed materials with different amounts of residual α-Si_3N_4 phase: β-Si_3N_4 intensity ratio $I(200)/I(002)$ as a function of the α/β-phase composition in the starting material for hot-pressed (HP) and post-hipped (HP + HIP) materials. ||HP: measured parallel to the hot-pressing direction. ⊥HP: measured perpendicular to the hot-pressing direction.

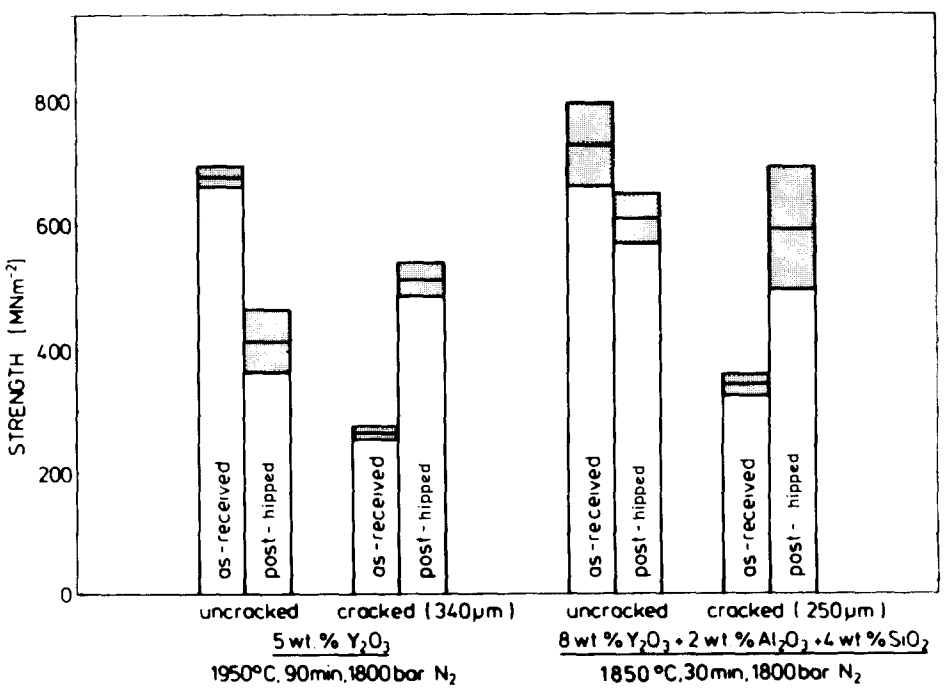

Fig. 12. Crack healing during post-hipping in two materials with different amount and composition of additive, i.e. different amount and viscosity of the liquid phase: flexural strength of uncracked and pre-cracked materials before and after hipping.

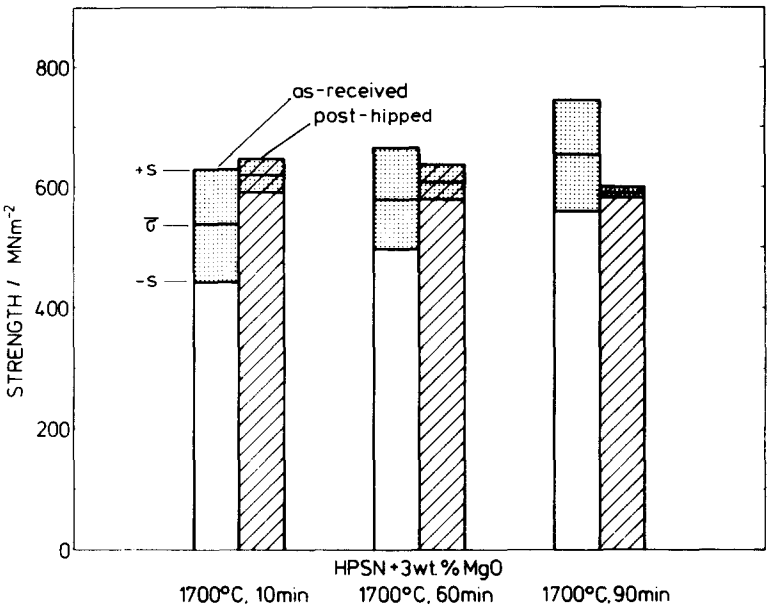

Fig. 13. Reduction of the scatter $\pm s$ in strength by post-hipping of badly machined hot-pressed materials.

5. DISCUSSION

The experimental results, particularly the systematic investigations and model experiments, permit some conclusions to be drawn about the microstructural changes which take place during post-hipping of pre-sintered materials and about the effect of these changes on the mechanical properties.

5.1. Microstructural changes

In nearly all materials with closed porosity sintered in nitrogen a slight reduction in total porosity was achieved by post-hipping. The change in density becomes smaller as the density of the pre-sintered material approaches the theoretical density. In the authors' experiments with holding times of ≤ 1 h at maximum temperature, theoretical density was not obtained. Here it should be noted, however, that for long holding times (≥ 6 h) theoretical density has been reached.[26] As the experiments with artificial pores indicated, the reduction of residual porosity is caused at least partially by filling of pores due to viscous flow of the liquid from two grain boundaries (or triple points) into the pores. Thus, pore filling is controlled by the viscosity and the amount of liquid phase. The difference between the compositions of the pore filling and the grain boundary phase might be caused by the silicon monoxide condensation, released by the liquid phase,

and by the presence of silicon nitride whiskers within the pore which may be formed by a gas phase reaction during sintering or during the first stage of hipping.

One important reason for the limitation in porosity reduction, however, is that during the post-treatment of pre-densified materials by hipping no essential rearrangement of the elongated β-Si_3N_4 grains takes place, as demonstrated by post-hipping experiments of pre-hot-pressed materials. Even for starting materials with a certain amount of residual α-Si_3N_4 phase the density increase is controlled by the interlocking of the elongated β-Si_3N_4 grains in the pre-densified materials ('bridge effect' during the application of high pressure). This observation is independent of the type and amount of additive.

Although the arrangement of grains during post-hipping of pre-sintered (or pre-hot-pressed) materials is not changed considerably, in many cases globularization (indicated by the decrease in the aspect ratio of the elongated β-Si_3N_4 grains) and grain coarsening take place. Both microstructural changes are dependent on the microstructure of the pre-sintered materials and the hipping conditions. Two typical examples are shown in Fig. 14. Here, as in most cases, a decrease in the length, $\bar{l}$, and the aspect ratio, $\bar{a}$, of the elongated β-Si_3N_4 grains has been observed. In both materials these changes are associated with density gains and an increase in fracture strength and fracture toughness. This is unusual behaviour, as the change in grain morphology towards equiaxed grains, due to long soaking times and high temperatures, usually leads to a strength degradation, as shown schematically in Fig. 15. Therefore, other mechanisms seem to affect the mechanical properties of post-hipped pre-sintered silicon nitride materials, as will be discussed in Section 5.2. Apart from these examples, the globularization and coarsening of the β-Si_3N_4 grains often resulted in a reduction in fracture strength and/or in some cases in fracture toughness. Thus, the processing parameters, temperature, time, pressure and atmosphere, are important, and the optimum conditions depend on the type and concentration of the additives.

The choice of temperature and atmosphere is limited by the decomposition of the silicon nitride and the vaporization of the liquid phase at high temperatures. Both effects result in microcavities in the surface area and in pore formation in the sub-surface zone which lead to strength degradation. This means that the hipping temperature and atmosphere have to be optimized for the different additives to avoid these negative effects. In order to minimize the thermal decomposition of the silicon nitride, hipping of unencapsulated materials is preferably carried out under high nitrogen pressure, and/or the preforms have to be embedded in a powder bed consisting of a mixture of silicon nitride and sintering additives.

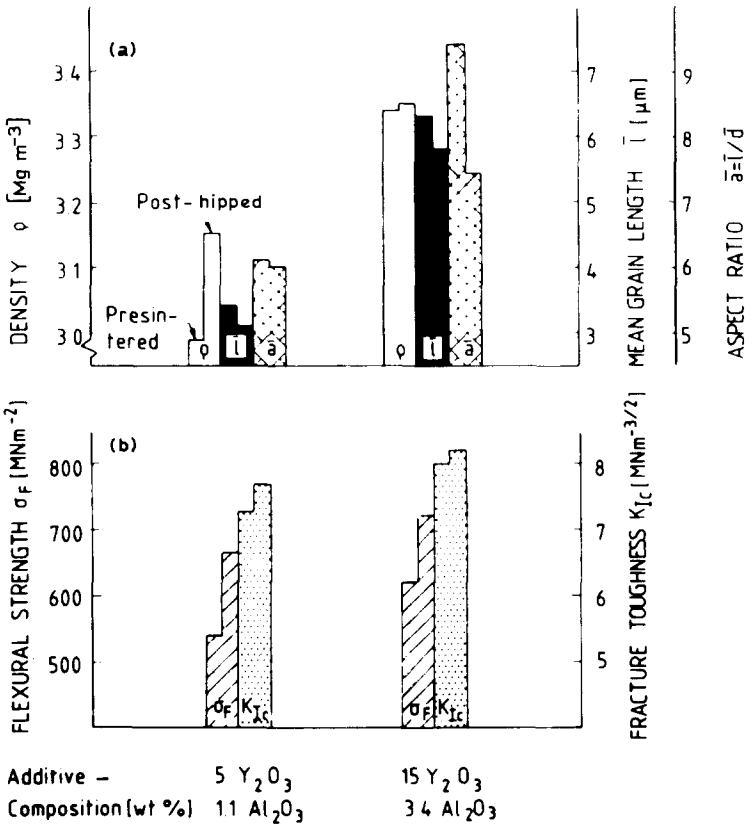

Fig. 14. Changes of microstructural characteristics and mechanical properties by post-hipping of two sintered materials with different additive compositions: (a) density (ρ), mean length ($\bar{l}$) and aspect ratio ($\bar{a}$) (ratio of length to thickness) of β-Si_3N_4 grains; (b) fracture strength (σ_F) and fracture toughness (K_{Ic}).

All these microstructural changes, which can occur during post-hipping, have to be considered when the mechanical properties of post-hipped materials are discussed.

5.2. Mechanical properties

A number of investigations show that the fracture strength of dense silicon nitride is generally controlled by various microstructural characteristics: the elongated β-Si_3N_4 grains frequently characterized by the aspect ratio, $\bar{a}$ ($\bar{a}\uparrow \rightarrow \sigma\uparrow$); the grain dimensions (grain size $\uparrow \rightarrow \sigma\downarrow$); and the residual porosity, P ($P\uparrow \rightarrow \sigma\downarrow$). Quantitative microstructural characterization of different types of dense silicon nitride, and the interdependence with mechanical properties, permit the conclusion to be drawn that the major factor controlling fracture strength (and fracture toughness) is the aspect

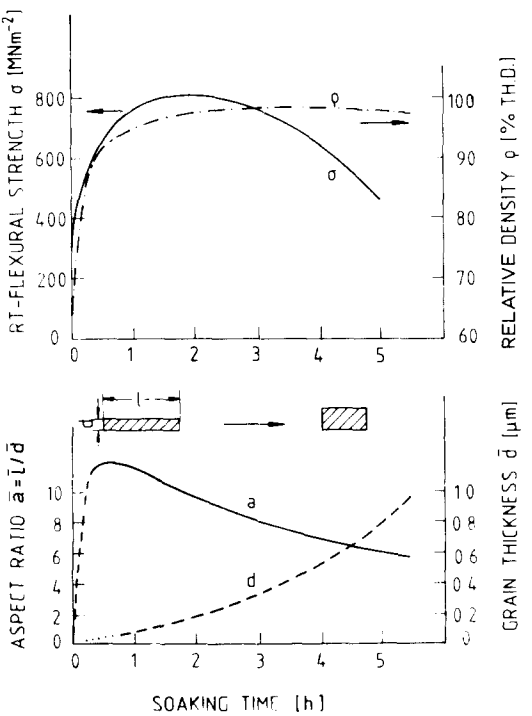

Fig. 15. Influence of soaking time on density, microstructural characteristics and the room-temperature flexural strength (schematic plot).

ratio of the β-Si_3N_4 grains.[24,25,28] The influence of grain size on fracture strength has been found to be essentially smaller. Nevertheless, there are some indications that other parameters, such as the amount and properties of the glassy phase, also have an influence on room-temperature strength.

The mechanical properties of silicon nitride after hipping are mainly controlled by the following changes: (i) the slight reduction of total porosity, (ii) the elimination or reduction of residual macropores, (iii) the healing of cracks, and (iv) the variation in grain size and grain morphology. Additionally, microcavities in the surface area may be created if during hipping in argon, or partly also in nitrogen, chemical decomposition cannot be avoided.

The slight reduction in total porosity and the filling of residual pores and other cavities result in an improvement of fracture strength, both of the absolute values and of the data scatter.

As is known from the literature, crack healing can occur in dense silicon nitride during post-annealing at temperatures higher than 900 °C, depending on the composition of the sintering additives.[31] Crack healing results in an improvement of mechanical properties, the absolute strength

and data scattering. Annealing treatments in different atmospheres indicate that two mechanisms are mainly responsible for crack healing: (a) formation of cristobalite and silicates on the surface due to the effect of atmospheric oxygen and (b) the viscous flow of the liquid phase. The extent of crack healing is dependent on the viscosity and the amount of liquid phase. In the case of high viscosity and low amounts of liquid, as used for high-temperature materials, crack healing is limited. For these materials the healing of cracks is enhanced by applying high pressure at high temperature during post-hipping. In particular, the improvement of the scatter is one of the main advantages of post-hipping of pre-sintered silicon nitride.

The quantitative microstructural analysis of various materials before and after post-hipping clearly demonstrates that in many cases a globularization and coarsening of the β-Si_3N_4 grains takes place (see Fig. 14). Usually these effects result in a reduction of fracture strength and fracture toughness. Nevertheless, for the post-hipped materials no clear relationship was observed between fracture toughness, K_{Ic}, and the aspect ratio, $\bar{a}$; for example, K_{Ic} can be increased by post-hipping, though the aspect ratio is reduced. Consequently, other parameters must be effective. These results may be explained by the build-up of residual stress and by plastic deformation of the elongated β-Si_3N_4 grains during post-hipping, which strengthens the interlocking growth and leads to a stronger linking of the elongated β-Si_3N_4 grains. This assumption seems to be confirmed by observations in the literature.[17–19] TEM studies are under way to prove this effect.

In the case of fracture strength, no systematic interdependence was found to exist between strength data and the aspect ratio, $\bar{a}$. Usually, strength degradation is expected with decreasing $\bar{a}$ value; this result, however, was not observed in all cases. The reason for this is that fracture strength of post-hipped materials is determined by the improvement of fracture toughness, and additionally by the reduction of pore size effects and by crack healing. Which effect is dominant depends on the morphology and arrangement of the β-Si_3N_4 grains and the characteristics of the liquid phase as well as on the hipping conditions.

6. SUMMARY AND CONCLUSIONS

The systematic investigations and model experiments allow some conclusions to be drawn about the factors which determine the post-hipping behaviour of pre-sintered silicon nitride materials, the mechanisms being effective and the resulting properties:

(a) Post-hipping of pre-sintered silicon nitride without canning primarily demands materials which reveal only closed porosity. This is

usually the case above about 94 % theoretical density of the starting material, otherwise encapsulation is necessary.

(b) In many cases only a slight increase in density was observed with materials pre-sintered in nitrogen. The reduction of residual porosity is caused by the filling of residual macropores, which may occur by squeezing out liquid phase from grain boundaries and triple junctions. A prerequisite is a sufficiently high amount of low-viscosity liquid phase.

(c) Though post-hipping may lead to an increase in density, in no case has theoretical density been achieved. One reason seems to be the rearrangement of the mainly elongated β-Si_3N_4 grains in pre-sintered silicon nitride compacts during hipping being prevented by a 'bridging' effect.

(d) The mechanical properties of hipped materials at room temperature are controlled by an overlapping of different effects. Essential positive effects are the slight density increase, particularly the filling of residual macropores or the reduction of the pore size, and the enhanced healing of cracks. Negative effects are the grain coarsening and grain globularization, as well as surface defects caused by vaporization of the liquid phase and decomposition of silicon nitride during hipping.

(e) As a result, a marked increase of strength levels is not observed. However, the scatter of strength values can be reduced and fracture toughness values often are improved. The latter observation seems to depend on a more intensive interlocking of the elongated β-Si_3N_4 grains, supported by local plastic deformation at the grain contact points. This is one more positive effect during post-hipping.

(f) Which effect is decisive depends on the morphology and arrangement of the β-Si_3N_4 grains and the characteristics of the liquid phase in the starting pre-sintered materials, as well as on the hipping conditions.

Therefore, an improvement of properties of pre-sintered silicon nitride by post-hipping demands optimized hipping conditions, as well as a well-defined microstructure of the pre-sintered starting material.

REFERENCES

1. Moritoki, M., HIP activities in Japan, *Proc. Conference on Hot-Isostatic Pressing: A Global Assessment*, Danvers, Mass., USA, 30 Mar.–1 Apr. 1982.
2. Fujikawa, T., Moritoki, M. and Homma, K., The high temperature HIP-furnace and its application in densification of ceramics, *Proc. 2nd International Conference on Isostatic Pressing*, Stratford-upon-Avon, 21–23 Sept. 1982.
3. Hunold, K., *cfi./Ber. Deut. Keram. Ges.*, **60** (1983) 182–9.
4. Larker, H., in *Ceramics for Turbine Engine Applications*, AGARD Conf. Proc. No. 276, AGARD, Neuilly sur Seine, France, 1979, 18/1–4.

5. Larker, H., in *High Pressure Science and Technology*, Vol. 2, Eds K. H. Timmerhaus and M. S. Barber, Plenum Publ. Corp., New York, 1979, 651–5.
6. Heinrich, J. and Böhmer, M., *Proc. Powd. Met. Aerospace Materials*, MPR Publ. Services Ltd, Bellstone, Shrewsbury, UK, 1984, 42/1–14.
7. Fujikawa, T., Moritoki, M., Kanda, T., Homma, K. and Okada, H., in *Ceramic Components for Engine*, Eds S. Sōmiya, E. Kanai and K. Ando, KTK Scientific Publ., Tokyo/D. Reidel Publ. Co., Dordrecht, 1983, 425–33.
8. Heinrich, J. and Böhmer, M., *Science of Ceramics*, **11** (1981) 439–46.
9. Heinrich, J. and Böhmer, M., *cfi./Ber. Deut. Keram. Ges.*, **61** (1984) 399–405.
10. Härdtl, K. H., *Philips Techn. Rdsch.*, **35** (1975/76) 46–53.
11. Adlerborn, J. and Larker, H., Verfahren zur Herstellung eines Gegenstandes aus Siliziumnitrid, Offenlegungsschrift 27 02 073 (1977).
12. Hunold, K., Reinmuth, K. and Lipp, A., Verfahren zur Herstellung von praktisch porenfreien polykristallinen Formkörpern durch isostatisches Heißpressen in Glashüllen, Europäische Patentanmeldung 0 050 875 A1 (1981).
13. Böhmer, M. and Heinrich, J., Verfahren zum heißisostatischen Pressen kompliziert geformter poröser Körper, Patentschrift DE 30 47 237 C2 (1980).
14. Heinrich, J. and Böhmer, M., Verbessertes Verfahren zum Verdichten poröser keramischer Bauteile für das heißisostatische Pressen, Patentanmeldung 34 03 917.1 (1984).
15. Larker, H., Adlerborn, J. and Bohmann, H., *Proc. International Automotive Engineering Congress and Exposition*, Detroit, 28 Feb.–4 Mar. 1977.
16. Heinrich, J. and Böhmer, M., *Powd. Met. Internat.*, **16** (1984) 233–5, 283–6.
17. Yeh, H. C. and Sikora, P. F., *Am. Ceram. Soc. Bull.*, **58** (1979) 444–7.
18. Wills, R. R., Brockway, M. C., McCoy, L. G. and Niesz, D. E., *Ceram. Eng. Sci. Proc.*, **1** (1980) 534–9.
19. Wills, R. R. and Brockway, M. C., *Science of Ceramics*, **11** (1981) 233–48.
20. Yamada, T., Shimada, M. and Koizumi, M., *Am. Ceram. Soc. Bull.*, **60** (1981) 1225–8.
21. Richerson, D. W. and Wimmer, J. M., *J. Am. Ceram. Soc.*, **66** (1983) C173–6.
22. Homma, K., Tatsuno, T., Okada, H. and Fujikawa, T., *Proc. 20th Japan Congress on Materials Research*, Kyoto, 1982.
23. Homma, K., Tatsuno, T., Okada, H. and Takada, H., *Zairyo*, **31** (1982) 960–6.
24. Wötting, G. and Ziegler, G., in *Ceramic Components for Engine*, Eds S. Sōmiya, E. Kanai and K. Ando, KTK Scientific Publ., Tokyo/D. Reidel Publ. Co., Dordrecht, 1983, 412–24.
25. Wötting, G. and Ziegler, G., *Ceramics International*, **10** (1984) 18–22.
26. Hirota, K., Ichikizaki, T., Hasegawa, Y. T. and Suzuki, H., in *Ceramic Components for Engine*, Eds S. Sōmiya, E. Kanai and K. Ando, KTK Scientific Publ., Tokyo/D. Reidel Publ. Co., Dordrecht, 1983, 434–41.
27. Kanka, B., Wötting, G. and Ziegler, G., in preparation.
28. Wötting, G. and Ziegler, G., *Science of Ceramics*, **12** (1983) 361–70.
29. Majdic, M. and Ziegler, G., *Ber. Deut. Keram. Ges.*, **57** (1980) 140–5.
30. Goebbels, K., Reiter, H., Hirsekorn, S. and Arnold, W., *Science of Ceramics*, **12** (1983) 483–94.
31. Ziegler, G., *Ber. Deut. Keram. Ges.*, **55** (1978) 397–400.
32. Ziegler, G., Bentsen, L. and Hasselman, D. P. H., *J. Am. Ceram. Soc.*, **64** (1981) C35–6.

Received 10 June 1985; accepted 20 July 1985

Int. J. High Technology Ceramics **1** (1985) 59–67

Sintering of CVD Aluminum Oxide–Titanium Dioxide Powders

Saburo Hori and Ryuichi Kurita

Kureha Chemical Industry Co. Ltd,
16 Ochiai, Nishikimachi, Iwaki City, Fukushima 974, Japan

and

Masahiro Yoshimura and Shigeyuki Sōmiya

Research Laboratory of Engineering Materials, Tokyo Institute of Technology,
4259 Nagatsuta, Midori-Ku, Yokohama 227, Japan

SUMMARY

The sintering behavior of co-deposited aluminum oxide–titanium dioxide powder prepared by a flame chemical vapor deposition (CVD) technique was studied in the compositional range of 56–73·5 wt% aluminum oxide. Significant densification was observed between 1100 and 1300°C with the co-deposited powder of stoichiometric composition, or of a slight excess aluminum oxide content. The titanium dioxide crystallites appeared to accelerate the densification when they were sufficient in amount and homogeneously mixed with the aluminum oxide. The excellent sinterability of these powders of relatively lower aluminum oxide content resulted in dense (maximum 95·5% of theoretical) and large-grained (20–50 μm) aluminum titanate ceramics at higher temperatures, while the microstructures of specimens from the mechanically mixed powder or from the co-deposited powder having an excess of aluminum oxide were porous and fine-grained. In the case of the co-deposited powder containing slight excess aluminum oxide, small (1–3 μm) aluminum oxide particles were dispersed on the boundary of β-Al_2TiO_5 grains.

1. INTRODUCTION

Aluminum titanate (Al_2TiO_5) is known as a ceramic material of low thermal expansion,[1,2] but its application for commercial uses is rather limited,

Int. J. High Technology Ceramics 0267-3762/85/$03·30

mainly due to its very low mechanical strength. The significant thermal expansion anisotropy of aluminum titanate, when the grains are larger than a critical size, causes extensive intergranular cracking and dilation during cooling after densification, which results in a low thermal expansion coefficient but also in low mechanical strength.[3]

In the previous studies on the pressureless sintering of aluminum titanate,[4–6] two categories of starting powder were used: mixed powders of aluminum oxide and titanium dioxide, and synthesized aluminum titanate powders. The latter showed better sinterability and gave a higher bend strength than the former. There still appeared to exist some room for improvement in sinterability and possibly in the mechanical properties, since the maximum density achieved with the synthesized powders was only about 94% of theoretical.[6]

The authors have initiated a chemical vapor deposition (CVD) technique to produce ultrafine sinterable two-component ceramic powders using a combustion flame process.[7] The usefulness of this technique was demonstrated by achieving dense zirconium dioxide-toughened alumina ceramics with a homogeneous zirconium dioxide dispersion from the CVD aluminum oxide–zirconium dioxide powders.[8]

The same technique has been applied to produce aluminum oxide–titanium dioxide powders in the compositional range of 56–73·5 wt% aluminum oxide, resulting in ultrafine ($\simeq$40 nm) spherical particles which contained γ-Al_2O_3 and minute ($\simeq$10 nm) rutile (TiO_2) crystallites.[9] The purpose of this study is to investigate the sintering behavior of the CVD aluminum oxide–titanium dioxide powders.

2. EXPERIMENTAL

Three compositions of the co-deposited aluminum oxide–titanium dioxide powders (55·9, 61·8 and 73·5 wt% aluminum oxide), CVD aluminum oxide (δ-phase) and titanium dioxide (mainly anatase) were produced by the flame CVD technique using the same reaction temperature and time. The average particle sizes of these powders ranged from 30 to 50 nm, and the co-deposited powders consisted mainly of γ-Al_2O_3 particles containing minute ($\simeq$10 nm) rutile crystallites.[9] The three co-deposited powders and the mixture of the CVD aluminum oxide and titanium dioxide powders (adjusted to be 61·8 wt% aluminum oxide) were dispersed into ethanol by ultrasonic agitation and filtered by filter paper (nominal size 7 μm) to remove foreign material. Each of the powder slurries which passed through the filter was centrifuged, dried and calcined at 800°C for 1 h. The calcination was intended to remove residual chloride ions from the powders because

chloride ions are generally known to hinder the densification,[10] but, at the same time, slight changes in crystalline phases were observed. The anatase which existed as a minor phase in the co-deposited powders, transformed to rutile, and the aluminum oxide became more like δ-phase rather than γ-phase.[9]

The calcined powders were ball-milled using a plastic lined mill and plastic media in water, together with a surfactant (Yukanol NCS, Tetsuno Yuka, Japan) for 40 h, dried at 80 °C for more than two days and milled again in a mortar. The powders were uniaxially shaped into pellets, isostatically pressed at 294 MPa, and dried further. Subsequent to the green density measurements, the specimens were preheated at 250 °C for 2 h and at 500 °C for 1 h to remove free water and sintered between 1000 and 1600 °C for 1 h in an air atmosphere by means of a 'Kanthal Super' box furnace. The temperature was raised from 500 °C to the target temperature in less than 20 min, and the furnace was cooled rapidly after sintering by switching off the power.

The densities of the specimens were determined by the weight/dimension measurements; some were confirmed by an Archimedes method using mercury displacement. The relative density calculations were simplified by assuming that the only phases in the theoretically dense specimens were β-Al_2TiO_5 and α-Al_2O_3, though aluminum titanate was not detected in the specimens sintered at temperatures up to 1200 °C. The theoretical densities of β-Al_2TiO_5[11] and α-Al_2O_3[12] were assumed to be 3·702 and 3·987 Mg m^{-3}, respectively.

X-ray diffraction (XRD) analyses using Cu–Kα were made mainly on the as-sintered surfaces of the specimens and the microstructures were observed by scanning electron microscopy (SEM) on the fractured surfaces.

3. RESULTS AND DISCUSSION

3.1. Phase changes during sintering

Figure 1 shows the change of XRD profile as a function of sintering temperature with the specimens of 61·8 wt% aluminum oxide. Similar changes of XRD profiles were observed with specimens of different compositions, except that the intensities of α-Al_2O_3 and rutile varied according to the composition.

Between 1000 and 1200 °C, the only phases detected were α-Al_2O_3 and rutile. The phase changes of Al_2O_3 from γ or δ to α occurred below 1000 °C, whereas they occurred at temperatures higher than 1000 °C, without titanium dioxide addition[13] or without compaction.[9] Titanium dioxide

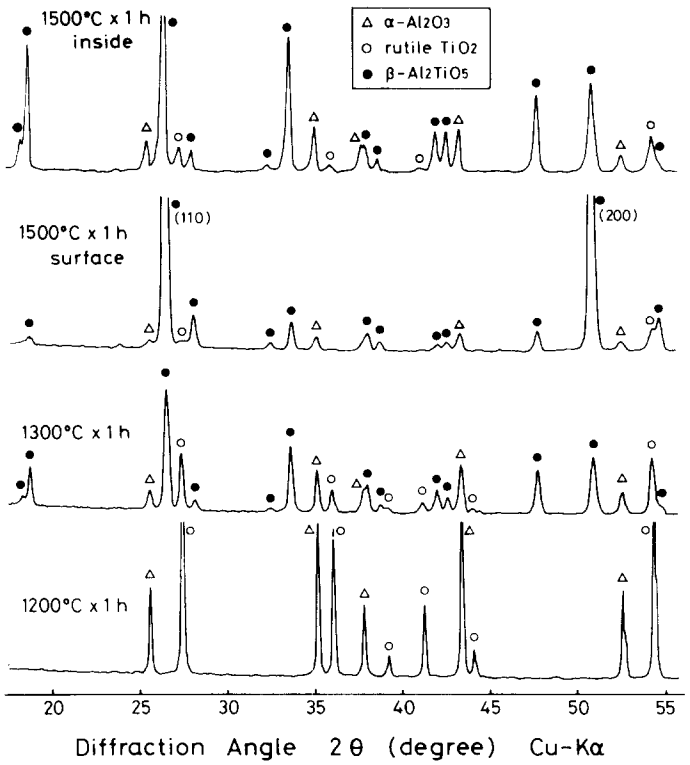

Fig. 1. Phase changes taking place during sintering in the case of powder No. 605 (co-deposited powder, 61·8 wt % aluminum oxide). The XRD measurements were made mainly on the as-sintered surfaces. The inside of the specimen sintered at 1500 °C was measured for comparison.

appeared to accelerate the Al_2O_3 phase changes from γ or δ to α especially when the powder was compacted. This is in contrast to the fact that a zirconium dioxide addition to δ-Al_2O_3 retarded the Al_2O_3 phase change.[13]

The reaction of α-Al_2O_3 and TiO_2 to form β-Al_2TiO_5 started to occur between 1200 and 1300 °C. The amount of unreacted aluminum oxide and titanium dioxide decreased when the temperature was raised further. The β-Al_2TiO_5 peaks indicated a strong orientation of the crystallites at high temperatures, especially when the composition was close to the stoichiometry of aluminum titanate. The (200) and (110) surfaces, especially the former, of β-Al_2TiO_5 appeared to be preferentially oriented parallel to the sintered surface.

Other phases, such as 'X-phase' reported by Gani and McPherson[14] or 'Y-phase' detected by calcining the co-deposited aluminum oxide–titanium dioxide powders,[9] were not observed.

3.2. Densification behavior

The densification behavior appeared very different from that of conventional ceramic materials and strongly dependent on the powder composition and characteristics. As shown in Fig. 2, significant densification occurred between 1100 and 1200 °C with the co-deposited powders of stoichiometric composition and with those with a slight excess aluminum oxide content (powder Nos 602 and 605). The densification did not proceed at such low temperatures with the co-deposited powder having an excess of aluminum oxide (No. 608) or with the mechanically mixed powder (No. 609).

The formation of β-Al_2TiO_5 appeared to retard densification. At 1300 °C, the formation of β-Al_2TiO_5 was so slow that the densification had progressed significantly before Al_2TiO_5 was formed. At 1400 °C, the densities of specimen Nos 608 and 609 decreased because β-Al_2TiO_5 was formed quickly before sufficient densification could take place. At temperatures higher than 1300 °C more severe microcracking was caused by the further formation of β-Al_2TiO_5 and the development of preferred orientation and, as can be seen in the case of Nos 602 and 605, this resulted in slightly lower densities. Specimen Nos 608 and 609 were densified further between 1400 and 1600 °C, as the driving force for densification became larger, because some porosity remained in these specimens.

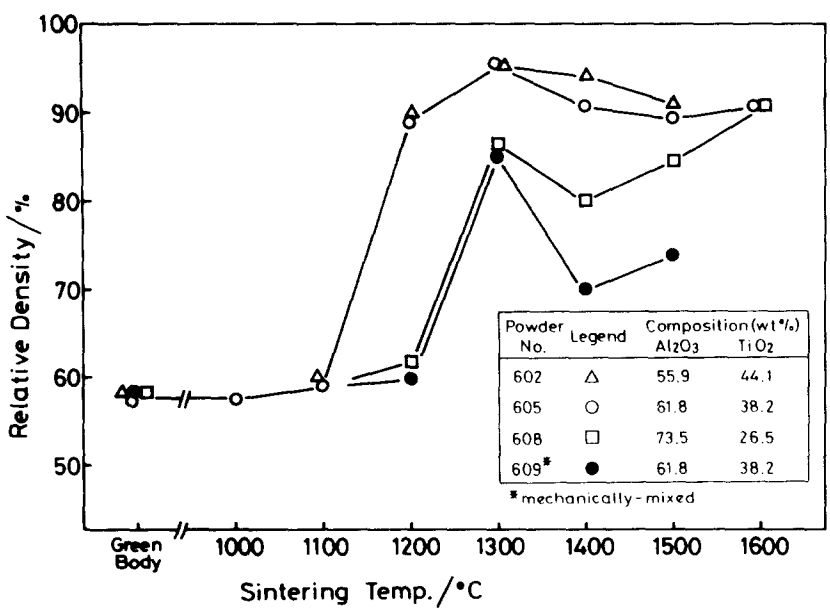

Fig. 2. Densification behavior of CVD aluminum oxide–titanium dioxide powders. Comparisons were made on compositions and between the co-deposited and the mechanically mixed powders.

It appeared advantageous to use the co-deposited powders of stoichiometric composition or of a slight excess aluminum oxide content because higher densities could be achieved before the formation of β-Al_2TiO_5. In comparison with the densification behavior of the synthesized aluminum titanate powder reported by Ohya *et al.*,[6] these co-deposited powders showed superior sinterability. The densities achieved from the co-deposited powders at 1200 °C for 1 h and at 1300 °C for 1 h were 89 % and 95·5 % of theoretical, respectively, which should be compared with 72 % and 78 % at 1300 °C for 2 and 4 h, respectively, achieved by the synthesized powder.

The reason for the low-temperature densification with these powders can be attributed to the existence of ultrafine titanium dioxide crystallites. As Yan and Rhodes[15] showed, titanium dioxide powders can be sintered at very low temperatures, especially when they are small in size and agglomerate-free. The rutile crystallites contained in the γ- or δ-Al_2O_3 particles are more effective at increasing the sinterability of aluminum oxide–titanium dioxide mixture than independent titanium dioxide particles mechanically mixed with aluminum oxide, not only because of their smaller sizes but also because of the better contact with aluminum oxide as hypothesized in the following. The rutile crystallites are probably swept out to the surface of the particles when Al_2O_3 transforms from γ (or δ) to α, and then the densification is strongly enhanced by these titanium dioxide crystallites on the surface of aluminum oxide particles. It appears important to obtain a sufficient amount of fine titanium dioxide crystallites attached to the surface of aluminum oxide particles, since the densification does not proceed at such low temperatures when the amount of titanium dioxide is small (No. 608) or when the powder is mechanically mixed (No. 609).

3.3. Microstructural observations

Figure 3 shows the scanning electron micrographs (SEMs) of the fractured specimens. The dependence of microstructure on sintering temperature was compared in the case of 61·8 wt % aluminum oxide (No. 605). At 1200 °C (Fig. 3(a)), the microstructure consisted of small ($\simeq 1\ \mu m$) aluminum oxide and titanium dioxide grains and appeared fairly dense despite the low sintering temperature. At 1300 °C (Fig. 3(b)), as the result of β-Al_2TiO_5 formation, the microstructure consisted of large (average $\simeq 50\ \mu m$) aluminum titanate grains and intergranular microcracking, while high density was achieved. The excess aluminum oxide appeared to be dispersed mostly as small (average $\simeq 3\ \mu m$) particles on the grain boundaries. Despite the high density and the large aluminum titanate grain sizes, the microcracking was not very severe, probably due to the incompleteness of the reaction between Al_2O_3 and TiO_2 to form β-Al_2TiO_5. At 1500 °C

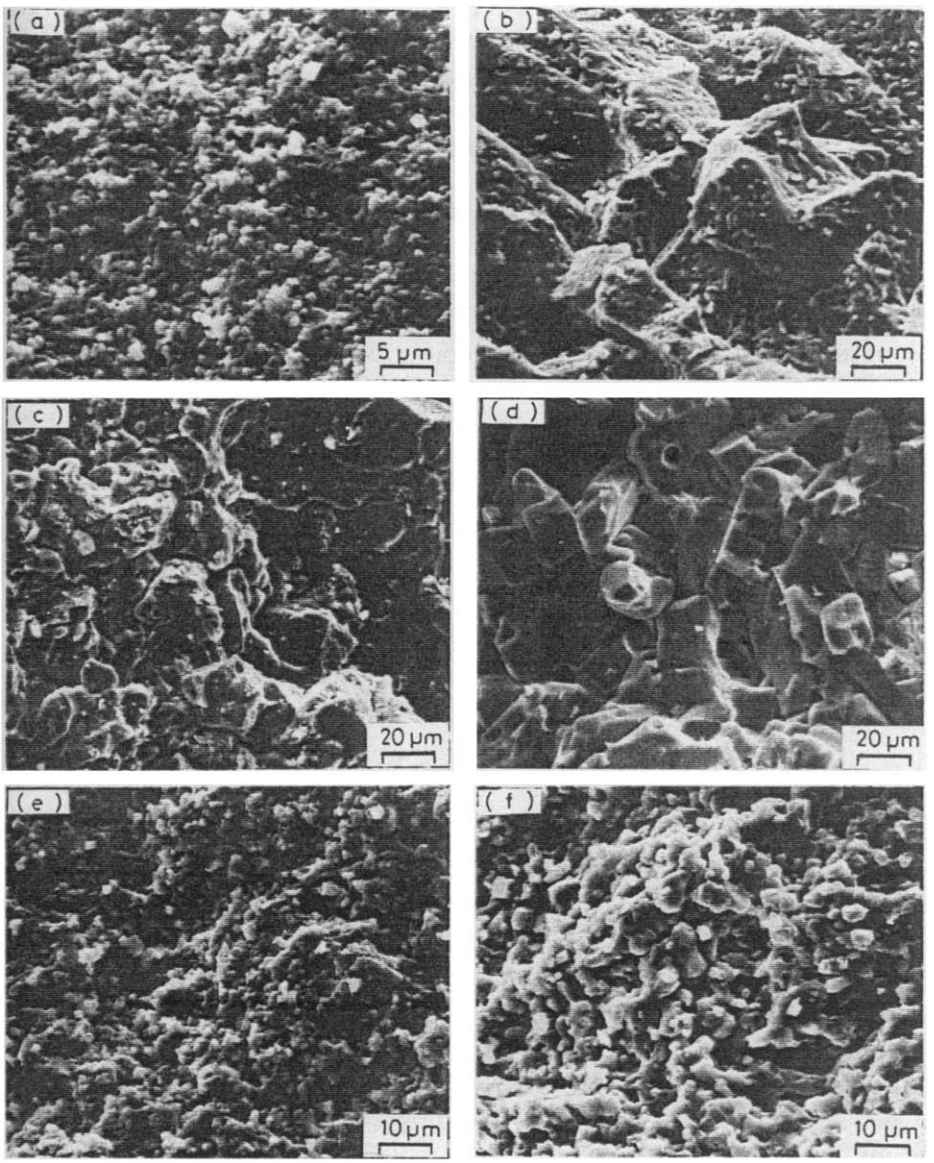

Fig. 3. Scanning electron micrographs of fractured specimens. (a), (b) and (c), No. 605 (61·8 wt % Al_2O_3) sintered at 1200, 1300 and 1500 °C for 1 h, respectively. (d), (e) and (f), sintered at 1500 °C for 1 h from No. 602 (55·9 wt % Al_2O_3), No. 608 (73·5 wt % Al_2O_3) and No. 609 (61·8 wt % Al_2O_3, mechanically mixed), respectively.

(Fig. 3(c)), the grain sizes were smaller (average 20–30 μm) and microcrack density was higher than those at 1300 °C. The reason can be attributed to the higher density of nucleation sites of β-Al_2TiO_5 resulting from the larger chemical driving force. The excess aluminum oxide was also dispersed on the grain boundaries but in smaller particle sizes. It appeared that the sintering schedule strongly influenced the microstructure.

The dependence of microstructure on the composition and powder characteristics was compared between specimens sintered at 1500 °C for 1 h in Figs 3(c), (d), (e) and (f). The specimens sintered from the co-deposited powder of stoichiometric composition (Fig. 3(d), 55·9 wt % aluminum oxide) showed almost the same aluminum titanate grain sizes and microcrack density as those of slight excess aluminum oxide, but the surfaces of aluminum titanate grains with the stoichiometric composition were very smooth, whereas those having a slight excess of aluminum oxide (Fig. 3(c)) were spotted and rugged, due to fine aluminum oxide particles. The specimens sintered from co-deposited powder of 73·5 wt % aluminum oxide (Fig. 3(e)) showed a porous microstructure of small grains. The existence of an excess of aluminum oxide prevented the densification and, at the same time, suppressed the grain growth. The specimens sintered from the mechanically mixed powder of 61·8 wt % aluminum oxide (Fig. 3(f)) showed a noticeably porous microstructure due to the poor sinterability. The co-deposited powder of the same composition achieved much higher density, as is apparent when Figs 3(c) and (f) are compared.

4. CONCLUSIONS

The co-deposited aluminum oxide–titanium dioxide powders of stoichiometric composition and with a slight excess aluminum oxide content showed excellent sinterability which could be attributed to the fact that there were sufficient titanium dioxide crystallites present which were very small in size and homogeneously mixed with the aluminum oxide. The microstructures of specimens sintered from these highly active powders at the higher temperatures appeared to be influenced by the amount of excess aluminum oxide and also by the density of nucleation sites for aluminum titanate formation.

These highly active powders can give more flexibility of processing parameters in controlling the microstructures and properties of aluminum titanate. Further study is in progress as to how the processing parameters, especially the sintering schedule, can affect the microstructures and properties.

ACKNOWLEDGEMENT

The authors thank Professor K. Hamano and his colleagues of the Research Laboratory of Engineering Materials, Tokyo Institute of Technology, for valuable comments on this paper.

REFERENCES

1. Buessem, W. R., Thielke, N. R. and Sarakauskas, R. V., Thermal expansion hysteresis of Al_2TiO_5, *Ceram. Age*, **60** (1952) 38–40.
2. Hamano, K., Aluminum titanate ceramic, *Taikabutsu* (*Refractories*), **27** (1975) 520–7.
3. Cleveland, J. J. and Bradt, R. C., Grain size/microcracking relations for pseudobrookite oxides, *J. Am. Ceram. Soc.*, **61** (1978) 478–81.
4. Hamano, K., Nakagawa, Z. and Sawano, K., Effects of additives on several properties of aluminum titanate ceramic, *Nippon Kagaku Kaishi*, (1981) 1647–55.
5. Hamano, K., Ohya, Y. and Nakagawa, Z., Microstructure and mechanical strength of aluminum titanate ceramic prepared from mixture of alumina and titania, *Yogyo-Kyokai-Shi*, **91** (1983) 94–101.
6. Ohya, Y., Hamano, K. and Nakagawa, Z., Microstructure and mechanical strength of aluminum titanate ceramics prepared from synthesized powders, *Yogyo-Kyokai-Shi*, **91** (1983) 289–97.
7. Hori, S., ZrO_2 and ZrO_2-containing ultrafine powders by chemical vapor deposition method, in *Zirconia Ceramics 1*, Ed. S. Sōmiya, Uchida Rokakuho, Tokyo, 1983, 21–8.
8. Hori, S., Yoshimura, M., Sōmiya, S. and Takahashi, R., Al_2O_3–ZrO_2 ceramics prepared from CVD powders, in *Advances in Ceramics 12: Science and Technology of Zirconia II*, Eds N. Claussen, M. Rühle and A. H. Heuer, The American Ceramic Society, Columbus, Ohio, 1984, 794–805.
9. Hori, S., Ishii, Y., Yoshimura, M. and Sōmiya, S., Preparation of codeposited Al_2O_3–TiO_2 powders by vapor phase reaction using combustion flame, submitted to *Yogyo-Kyokai-Shi*.
10. Scott, C. E. and Reed, J. S., Effect of laundering and milling on the sintering behavior of stabilized ZrO_2 powders, *Am. Ceram. Soc. Bull.*, **58** (1979) 587–90.
11. JCPDS X-ray Powder Diffraction File, No. 26-40.
12. JCPDS X-ray Powder Diffraction File, No. 10-173.
13. Hori, S., Kurita, R., Yoshimura, M. and Sōmiya, S., Densification and grain growth of ZrO_2-toughened Al_2O_3 ceramics from CVD powder, *Rept Res. Lab. Engineering Materials, Tokyo Institute of Technology*, **10** (1985) 45–55.
14. Gani, M. S. J. and McPherson, R., The structure of plasma-prepared Al_2O_3–TiO_2 powders, *J. Mater. Sci.*, **15** (1980) 1915–25.
15. Yan, M. F. and Rhodes, W. W., Low-temperature sintering of TiO_2, *Mater. Sci. Eng.*, **61** (1983) 59–66.

Received 18 June 1985; amended version received and accepted 30 July 1985

Int. J. High Technology Ceramics **1** (1985) 69–79

Ceramics for High Performance Rolling Element Bearings: A Review and Assessment

R. Nathan Katz

Army Materials and Mechanics Research Center,
Watertown, Massachusetts 02172, USA

and

James G. Hannoosh

Norton Company, Worcester, Massachusetts 01606, USA

SUMMARY

Modern, high performance structural ceramics offer the potential for a significant increase in many of the performance characteristics of both rolling element and sliding contact bearings. Thus, substitution of high performance ceramics for conventional metals is becoming an increasingly attractive option in applications where systems performance is currently constrained by state-of-the-art bearing technology. This paper will review the potential benefits of ceramics and provide selected examples where these benefits have been demonstrated in research and development programs. The emphasis will be on rolling element bearings. The desired properties for ceramic bearings and the properties of currently available high performance ceramics will be reviewed. The problem areas which are impeding the implementation of ceramic bearing technology, and directions for future research and development to resolve these impediments, will be discussed.

1. INTRODUCTION

The development of the first high performance structural ceramic, fully dense hot-pressed silicon nitride (HPSN), in the late 1960s coincided with a growing awareness that new materials for rolling elements would be required to meet the evermore stringent systems demands imposed on aircraft gas

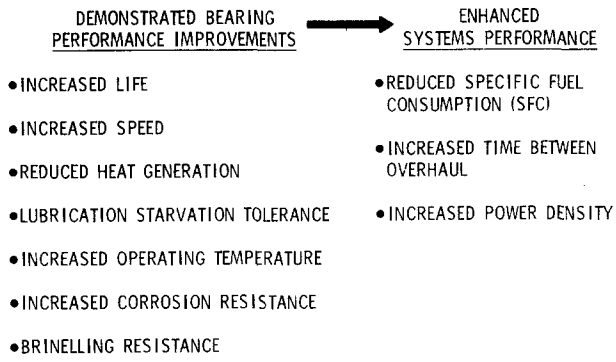

Fig. 1. Potential benefits of ceramics in bearings.

turbine bearings. Thus, the past dozen years have seen a number of modestly funded research and development programs aimed at the application of HPSN element bearings in high performance gas turbine engines.[1-7] What advantages do high performance ceramics offer the bearing designer to merit this effort?

Figure 1 lists the effects that ceramic elements could have on bearing performance. These benefits have their ultimate pay-off in several areas of enhanced systems performance, also listed in Fig. 1. The increased fatigue life of HPSN rolling elements has been demonstrated for roller elements by Baumgartner,[2] and for balls by Dalal,[4] both via rig tests. Baumgartner[5] has reported verification of the increased fatigue life of HPSN rolling elements in actual bearing tests. In this reference, Baumgartner also discusses the mechanism of fatigue failure in NC-132 HPSN,* pointing out that the fatigue spalls which cause failure result from non-elastic behavior of this material. The increased fatigue life of NC-132 HPSN rolling elements (balls) is very dependent on the quality of the surface finish, as shown by Dalal's data in Table 1[4] and Sibley's data.[7] Increased speed (DN) results from the lower mass density of silicon nitride as compared to steels. This lower density will also reduce skidding. Sibley[7] has pointed out that ceramic balls can reduce heat generation. Thus, they may allow the reduction of the size of oil cooling systems, thereby reducing cost and vulnerability.

Perhaps one of the most intriguing benefits of ceramic rolling element bearings is the possibility of lubrication starvation tolerance. Bersch[3] has reported that a bearing with HPSN rollers survived a rig test for 117 h with the lubricant shut off. The bearing condition at the end of the test was reported as 'good'! Figure 2 shows the result of a lubrication starvation test

* NC-132 is a commercial hot-pressed silicon nitride (containing magnesium oxide additive) manufactured by the High Performance Ceramics Division of Norton Company, Worcester, Massachusetts, USA.

TABLE 1
Rolling Four-ball Fatigue Life Test Data on 17·5 mm CVM M-50 Steel and Silicon Nitride Balls Finished by Various Methods

Spindle ball	*Spindle speed /rpm*	*Max. Hertz stress /GPa (ksi)*	*No. of CVM M-50 steel support ball set failures*	*Test life /10^6 revs*	*Spindle ball condition after test*
M-50	5 200	4·7 (680)	0	20·2	Spalled
			0	3·2	Spalled
			1	26·0	Spalled
			0	11·0	Spalled
			0	7·1	Spalled
			0	11·7	Spalled
As-received silicon nitride (NC-132)	5 200	4·7 (680)	2	117·3	Spalled
	10 000	5·5 (800)	1	12·0	Spalled
	10 000	5·5 (800)	0	66·6	Spalled
	10 000	5·5 (800)	0	24·6	Spalled
	10 000	5·5 (800)	1	41·5	Spalled
	10 000	5·5 (800)	2	18·3	Spalled
Diamond lapped silicon nitride (NC-132)	10 000	5·5 (800)	1	190·8	Intact
			1	183·6	Intact
			3	183·0	Intact
			1	182·4	Intact
			3	102·0	Spalled
			3	183·6	Intact

of an all NC-132 HPSN (except for the cage) roller bearing in an engine. All components survived approximately one hour of full engine testing. This attribute of silicon nitride for rolling element bearings offers enormous potential for aircraft safety in general and battlefield survivability in particular. Sibley has reported[7] that in one instance an HPSN ball bearing, with M-50 steel races running at 93 000 rpm and 200 N load, survived the complete destruction of the cage. In this instance the HPSN balls and M-50 races both emerged in excellent condition. This is further substantiation of the ability of HPSN rolling elements to endure very abusive environments.

Given the above benefits of ceramics, their future application in high speed and ultrahigh speed turbomachinery would seem to be a natural progression. A potential application for ceramic roller bearings is the adiabatic turbocompound diesel engine (ATDE). In the ADTE there is no radiator (or forced cooling), the cylinder walls are insulated and waste heat previously rejected to the environment via the radiator is now entrained in the exhaust. The hot exhaust is then run through a small gas turbine, the output of which is geared back into the main power shaft. This is the

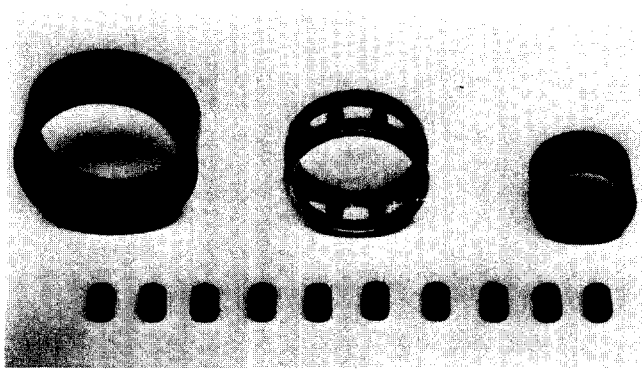

Fig. 2. NC-132 HPSN roller bearing tested in an engine 50 min at 39 000 rpm without lubricant.

turbocompounding feature. The ultimate refinement of such an engine is the minimum friction–minimum heat rejection ATDE as described by Bryzik and Kamo.[8] In this refinement, as illustrated in Fig. 3, sliding friction is converted into rolling friction with an attendant reduction of friction by a factor of 3–5 times. If the piston rings are replaced by a piston which operates as a gas bearing, as also shown in Fig. 3, friction and heat rejection will be further reduced. Full implementation of this concept requires bearings which do not require oil lubrication or oil cooling. Thus, dry lubricated ceramic bearings are the currently favored design option. Should this be demonstrated as feasible technology, the demand for ceramic roller bearings could be very large. In any event, it is apparent that there are several applications in which ceramic bearing elements would provide significant benefits. We now turn our attention to the question 'Which ceramics?'.

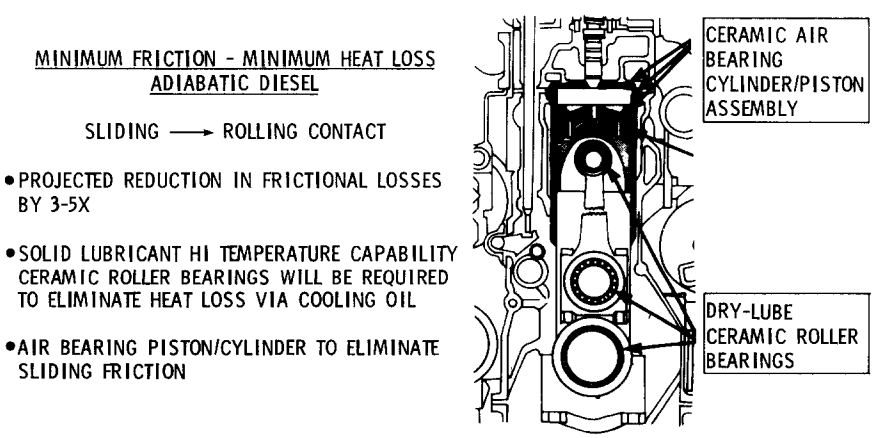

Fig. 3. Ceramic bearings for diesel engines.

2. POTENTIAL CERAMIC BEARING MATERIALS

Before discussing which ceramics have potential for application as bearing materials we must have a clear idea of what properties we would like in an enhanced bearing material. Table 2 provides such a listing. The desire for low density has been discussed above. However, it is important to point out that low density cannot be provided by porosity in the bearing material. From a microstructural standpoint the bearing must be essentially 100% theoretical density. The need for hardness, strength and corrosion resistance are self-explanatory. While a high fracture toughness is listed as a desired property, this must be put into the proper context. M-50 steel, the state-of-the-art high performance bearing steel, has a fracture toughness of only about 15 MN $m^{-3/2}$. Hot-pressed silicon nitride, which gives excellent rolling contact fatigue life, has a fracture toughness value of only 5 MN $m^{-3/2}$. Thus, a value somewhere between 5 and 15 MN $m^{-3/2}$ is a realistic goal. What is of note is that while fracture toughness is an important parameter for high performance bearings, the magnitude of the toughness which is required is much less than in many other highly loaded structural applications. This is an important point for the application of ceramics to such bearings. A low value of elastic modulus, E, is desired to minimize contact stresses. However, all of the current generation high performance ceramics (silicon nitride, silicon carbide and zirconia) have values of E equal to, or significantly greater than, steel. The upper use temperature listed is far above that which any oil-lubricated bearing could tolerate. However, under lubrication starvation or uncooled, dry lubricant conditions, such high temperature capability is to be desired. Finally, we must address the subject of failure mode. While we do our best to reduce the possibility of bearing element failure (and consequently bearing failure), we cannot entirely eliminate it. Thus, when a bearing element does fail it should be in a relatively benign mode such as spalling, rather than by catastrophic

TABLE 2
Desired Properties for Bearing Ceramics

Fracture toughness, K_{1c}	High	> 5 MN $m^{-3/2}$
Hardness	High	> 1 200 kg mm^{-2}
Elastic modulus	Low	< 210 GPa
Density	Low	< 4 Mg m^{-3}
Bend strength	High	> 700 MPa
Corrosion resistance	High	—
Upper use temperature	High	> 800 °C
Failure mode	'Steel-like' spallation	Small spalls

TABLE 3
Properties of High Performance Structural Ceramics and M-50 Steel

Property	*Silicon nitride*	*Silicon carbide*	*Alumina*	*Zirconia*	*M-50 steel*
Description	Hot-pressed NC-132	Sintered	Fully dense sintered	Sintered transformation-toughened	Wrought ingot
Fracture toughness, K_{1c} /MN m$^{-3/2}$	5–6	4	5	8–10	12–16
Hardness, H /kg mm^{-2}	~1 800–2 000	~2 800	~2 000	~1 300	~800
Elastic modulus, E /GPa	310	410	385	205	210
Density, ρ/Mg m^{-3}	3·2	3·1	4	5·6	8
Modulus of rupture /MPa	700	450	550	600–900	NA
Corrosion resistance	High	High	High	High	Moderate
Upper use temperature /°C	1 100	1 400	1 000+	800–900	325
Failure mode	Spalling	Fracture	Fracture	Spalling	Spalling

fracture. Clearly, the spalls should be as small as possible and certainly not significantly larger than those resulting when M-50 bearing elements fail.

Given the above list of desired properties, how do the modern high performance structural ceramics appear? Table 3 lists the properties of NC-132 HPSN, sintered silicon carbide, sintered alumina, sintered transformation-toughened zirconia (TTZ) and M-50 steel. While HPSN has been the choice for ceramic rolling elements in the demonstration programs described above, transformation-toughened zirconia has a rather intriguing set of properties. It is possible that, if this material could be fabricated with near zero porosity and a significantly reduced grain size, it would be an outstanding rolling element. In any event the silicon carbide, the alumina and the TTZ materials all have potential as sliding bearings materials.

Given the performance gains and successful bearing demonstrations described in the introduction and the desirable properties described above, why are the ceramic bearings not in wider use today? The following section deals with that question from the standpoints of design and manufacturing technology.

3. PROBLEM AREAS

In most instances where the potential for material substitution exists, there are institutional, technological and economic factors which are actual or perceived problems, and which act to retard the rate of implementation of

the new technology. In the specific case of ceramics for rolling element bearings these factors include brittleness, different design practices, reliability and reproducibility of product, and cost.

Ceramics, even the modern high performance ceramics, are brittle materials. Yet, as we saw in Fig. 5, M-50 steel is also a brittle material (low fracture toughness). Since current metallic high performance bearings utilize brittle materials, bearing designers are already familiar with probabilistic design techniques. Also, at least in the case of HPSN, the rolling contact fatigue failure modes of the metallic and ceramic bearings are the same, namely spalling. Thus, brittleness *per se* is not a problem. When people cite it as a problem they are probably using the word as a form of shorthand for three real problems often associated with, but not necessarily related to, brittleness. First, for ceramics other than fully dense silicon nitride and tough zirconias, there is the worry about failure mode (i.e. rolling elements made of the other ceramics fracture rather than spall). Secondly, existant design codes, predictive models and related computer programs have been developed and optimized based on steels. As pointed out by Bersch[3] and Sibley,[7] this produces both non-optimal designs and erroneous life and heat generation rate predictions when applied to ceramics with their very different properties. Thus, a critical need is to generate design and life prediction programs appropriate for ceramics—in particular, fully dense silicon nitride. The authors are aware that some work on the development of such codes for both metal/ceramic hybrid and all-ceramic bearings is currently under way. Thirdly, greater scatter in the performance of ceramic (HPSN) rolling elements than that in M-50 elements was occasionally observed prior to 1980. Such scatter in properties may be exacerbated by brittleness but its root cause was the small scale and relative immaturity of ceramic bearing manufacturing technology. This scatter has been reduced or eliminated over the past several years by process improvements which stress cleanliness and control. In some recent cases it has been observed that NC-132 HPSN is more reliable (less scatter) than M-50 steel.

Until recently, silicon nitride rolling elements have been made by hot-pressing billets, cutting the billets into blanks, rough machining the blanks into spheres or cylinders and then finally grinding and polishing the elements. All machining, grinding and polishing requires diamond abrasives and is thus inherently expensive. Additionally, there is at present no cost-effective, real-time, high-reliability quality control methodology to identify substandard blanks prior to adding value in the finishing process, or even to ensure high life elements after machining has been accomplished. In order to ensure high-reliability ceramic rolling elements, a manufacturing-based reliability strategy must be developed, as illustrated in Fig. 4. The key points in Fig. 4 are the focus on in-process quality assurance (QA), analysis and

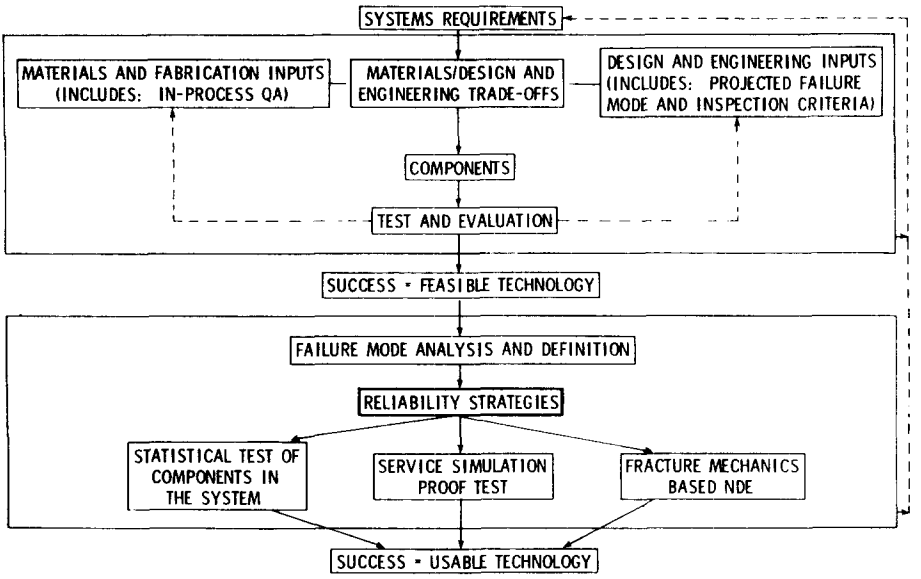

Fig. 4. Brittle materials design/reliability—systems trade-off logic.

definition of failure modes leading to realistic inspection criteria, and the development of a post-processing quality monitoring methodology which will both measure the product quality and provide input into how the process should be modified to correct any detected deficiencies.

Development of such a manufacturing based reliability strategy will clearly improve reliability and reproducibility of the ceramic rolling elements. But what about cost? Part of the current high cost of ceramic rolling elements is attributable to the fact that thus far they have only been produced in limited size prototype batches. However, part of the high cost is also the result of starting with billets which require excessive diamond cutting and polishing. The economic feasibility of ceramic bearing elements requires techniques to fabricate blanks to near net shape.

Currently, one of the authors is involved in developing a pilot scale process for producing near net shape silicon nitride bearing components. The recent technical advances in this area will allow for the cost-effective manufacturing of these components. Work is also proceeding in the area of quality assurance. Non-destructive examination (NDE) techniques as well as proof testing are being evaluated at several stages in the manufacturing process. The goal of this effort is to produce bearing elements that are competitive with high performance steels. Examples of some net shape components are shown in Fig. 5. Preliminary test results of near net shape parts show rolling contact fatigue life comparable to, or better than, that of hot-pressed billet material.

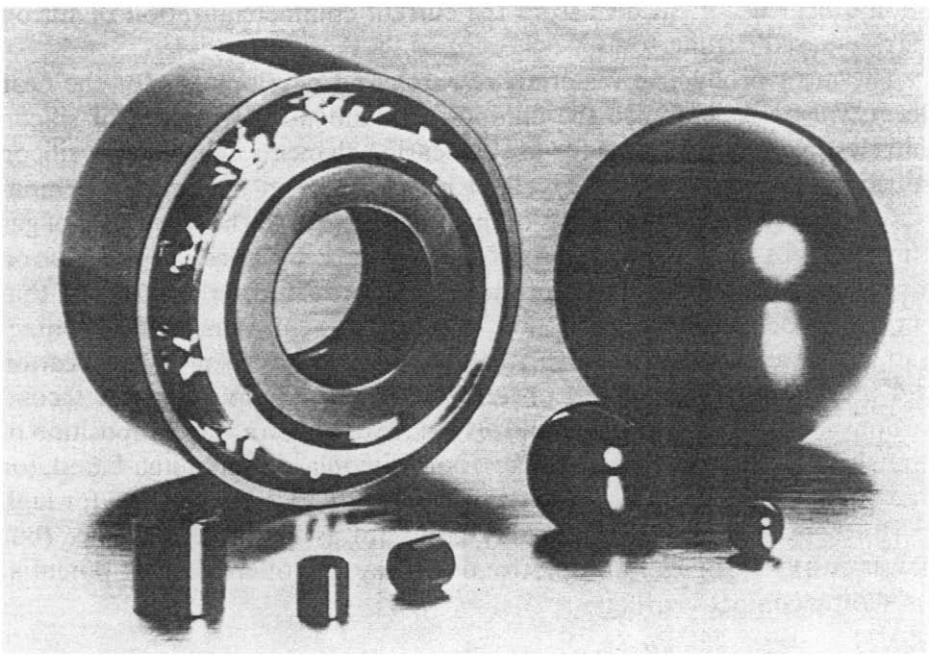

Fig. 5. Examples of net shape components.

4. DIRECTIONS FOR FUTURE RESEARCH

The main thrust of research and development on ceramics for rolling element bearings for the near term future must be on processing and manufacturing technology if the two impediments to application, reliability and cost are to be overcome. In particular, a method to produce near net shape preforms, from which fully dense silicon nitride elements can be fabricated, is an urgent requirement. As mentioned above, at least one US manufacturer is working in this area. One potential route to achieve this is to use a two-step nitrogen overpressure sintering process to effectively 'cladless' hot isostatically press (hip) the silicon nitride elements. In this process silicon nitride preforms are sintered to the closed porosity state (about 92–95% of theoretical density) under one or two atmospheres of nitrogen and then the nitrogen pressure is increased to 20–100 atm. The result, as described by Gazza *et al.*,[9] is a material with microstructure and properties similar to HPSN. The advantages of such a technique over conventional hipping technology are less potential for surface reactions or damage, less labor and lower capital cost for equipment. Both net shape processing and quality assurance of small high quality fully dense silicon nitride components

should benefit a great deal from the current commercialization of silicon nitride-based cutting tools.[10,11]

The most productive materials research and development for the near term will be to optimize the composition and microstructure of silicon nitrides (including sialons) for use as bearing elements. The current silicon nitrides which have shown excellent performance in the bearing demonstration programs are materials optimized for use in the hot flow path of gas turbines, not as bearing materials! Recent work by Lucek at the Norton Company on optimized compositions of silicon nitride has shown that improved performance is possible. This improvement in rolling contact fatigue life and performance variability is obtained by proper densification aid addition, as well as key process parameter manipulation. A second promising area would be to optimize the microstructure and composition of transformation-toughened ceramics, both zirconia- and alumina-based, for bearing application. These materials, in addition to their potential for high performance rolling elements, may be useful as lower performance (but lower cost) bearings for automotive use. They also offer excellent potential as sliding contact bearings.

5. CONCLUSIONS

This paper has shown that ceramic materials (NC-132 HPSN in particular) have demonstrated high potential and feasibility for application as rolling elements in bearings.

The major point of this paper is that the significant potential of ceramic bearings will require a major effort in manufacturing science and technology in order to be realized. Because such an effort must be highly focused and will require a large expenditure for any given material to be developed, only materials such as fully dense silicon nitride with demonstrated bearing performance are likely to be beneficiaries of such programs.

REFERENCES

1. Chiu, Y. P. and Dalal, H., Lubricant interaction with silicon nitride in rolling contact applications, in *Ceramics for High Performance Applications*, Eds J. J. Burke, A. E. Gorum and R. N. Katz, Brook Hill Publishing Co., Chestnut Hill, Massachusetts, USA, 1974, 589.
2. Baumgartner, H. R., Evaluation of roller bearings containing hot-pressed silicon nitride rolling elements, ibid., 713.
3. Bersch, C. F., Overview of ceramic bearing technology, in *Ceramics for High Performance Applications—II*, Eds J. J. Burke, E. S. Lenoe and R. N. Katz, Brook Hill Publishing Co., Chestnut Hill, Massachusetts, USA, 1978, 397.

4. Dalal, H. M., Machining bearings for turbine applications, ibid., 407.
5. Baumgartner, H. R., Ceramic bearings for turbine applications, ibid., 423.
6. Bersch, C. F., Ceramics in rolling element bearings, in *Ceramics for Turbine Engine Applications*, AGARD Conf. Proc. No. 276, AGARD, Neuilly sur Seine, France, March 1980, 9.
7. Sibley, L. B., Silicon nitride bearing elements for high-speed high-temperature applications, in *Problems in Bearings and Lubrication*, AGARD Conf. Proc. No. 323, AGARD, Neuilly sur Seine, France, 1982, 5.
8. Bryzik, W. and Kamo, R., TACOM/Cummins adiabatic engine program, in *The Adiabatic Diesel Engine*, SAE SP-543, 1983, 21.
9. Gazza, G. E., Katz, R. N. and Priest, H. F., Densification of Si_3N_4 Y_2O_3/Al_2O_3 by a dual N_2 pressure process, *J. Am. Ceram. Soc.*, **64**(11) (1981) C161.
10. Ezis, A., A silicon nitride cutting tool, paper presented at the *8th Annual Conf. on Composites and Advanced Ceramics*, American Ceramic Society, Cocoa Beach, Florida, Jan. 1984.
11. North, B., Substitution of ceramics for conventional cutting tools, *Materials and Society*, **8**(2) (1984) 257–70.

Received 18 July 1985; accepted 1 August 1985

Int. J. High Technology Ceramics **1** (1985) 87–105

Creep of Reaction-bonded, Siliconized Silicon Carbide

H. Cohrt and F. Thümmler

Institut für Werkstoffkunde II, Universität Karlsruhe,
Institut für Material- und Festkörperforschung, Kernforschungszentrum Karlsruhe,
Postfach 3640, D-7500 Karlsruhe 1, FRG

SUMMARY

Creep of reaction-bonded siliconized silicon carbide (SiSiC) has been found to be of a transient nature under most of the experimental conditions, and can be described by an extended Norton creep law, considering strain-hardening processes. The deformation is controlled by the silicon carbide skeleton that limits the deformation. A steady-state creep component of the creep curve, observed only under certain conditions, seems to be correlated with microstructural damage. The damaging process can be divided into two stages, microcrack formation and microcrack growth, the latter leading also to pore formation. Creep rupture occurs only above a threshold stress.

1. INTRODUCTION

Of the technical ceramics, those based on silicon carbide and silicon nitride have reached the greatest potential for use at high temperatures. A special silicon carbide material is the reaction-bonded, siliconized silicon carbide (SiSiC). The evaluation of this material has reached a standard which allows its successful use as a structural material at temperatures up to 1350 °C, for example for combustion chambers, components of gas-turbines, heat exchangers, evaporators, thermally stressed rollers, and rocket nozzles.

SiSiC is a two-phase ceramic material consisting of up to 95% silicon carbide, and free silicon in the range 5–40%. The density varies from 3·17–2·86 $Mg\,m^{-3}$ with variation in the content of free silicon. At the present time 25 °C bend strength values of 350–400 M Pa can be reached. The good thermal conductivity and the low thermal expansion result in good

Int. J. High Technology Ceramics 0267-3762/85/$03·30

TABLE 1
Literature Results Dealing with Creep of SiSiC

Author	*Year of publication*	*Test parameter*		*Atmosphere*	*Results*	*Reference*
		Temperature/ °C	*Stress/ MPa*			
P. Marshall	1967	1 000–1 360	290	Carbon dioxide	Transient creep according to $\varepsilon \sim t^{1/3}$, grain boundary sliding influenced by free silicon	1
J. C. V. Rumsey and A. L. Roberts	1967	1 200	140–170	Air	Stationary creep, creep mechanism influenced by free silicon	2
P. Marshall and R. B. Jones	1969	1 000–1 200	207–414	Air	Transient creep according to $\varepsilon \sim t^k$, $k = 0{\cdot}2$–$0{\cdot}5$	3
R. M. Adams	1972	Tensile test		—	Stationary creep, $\dot{\varepsilon}_s \sim \sigma^n$, $n = 1$	4
N. J. Osborne	1975	1 227–1 370	77	Air	No statement on creep mechanisms	5
M. Seltzer	1976	1 400	110–138	Air	No statement on creep mechanisms	6
V. Krishnamachari and M. R. Notis	1977	1 300–1 400	34–86	Air	Grain boundary diffusion controlled by silicon-diffusion	7
D. C. Larsen *et al.*	1978	1 200	240–275	Air	No statement on creep mechanisms	8
G. Wirth *et al.*	1978	1 200 Tensile test	1 200	Air	No statement on creep mechanisms	9
K. Schnürer *et al.*	1979 1980	810–1 200	100–190	Air and vacuum	Grain boundary diffusion controlled by silicon diffusion and dislocation mechanisms within the silicon carbide grains	10 11
E. Gugel *et al.*	1981	1 200–1 350	130–190	Air	No final statement on creep mechanisms	12
C. H. Carter *et al.*	1984	1 575–1 650 Compression test	110–220	Air	Stationary creep, $\dot{\varepsilon}_s \sim \sigma^n$, $n = 5{\cdot}7$ Dislocation climb within silicon carbide grains	13

thermal shock resistance. The inherent good oxidation resistance of the constituents results in good oxidation behaviour of SiSiC.

In looking at creep behaviour, large differences in the interpretations of the results are seen. A comprehensive overview of the papers dealing with creep of SiSiC is given in Table 1. In this work the creep behaviour of SiSiC is reinvestigated and attention is drawn to the deformation mechanisms. The process of creep damage is also discussed.

2. MATERIALS

The investigations were carried out on two materials produced by slip casting. The main features of the materials are given in Table 2. Free carbon was found to be the main impurity but with a total content of not

TABLE 2
Content of Free Silicon and Density of the SiSiC Materials

Material	*Free silicon*		*Density* ρ/*Mg m*$^{-3}$	
	(*Vol.* %)	(*wt* %)	ρ_1[a]	ρ_2[b]
1	15·5	11·7	3·03	3·08
2	14·5	11·0	3·08	3·09

[a] Determined by weighing.
[b] Determined by image analysis.

more than 0·5 %. Other impurities were found only in small quantities (i.e. Fe < 0·1 %, Ca < 0·05 %, Mg < 0·01 %, Al < 0·1 %, B < 0·1 %). These impurities were detected by wet chemical methods. Oxygen was not found by Auger-electronspectroscopy if the sample had been sputtered by argon ions during the measurement. Therefore the material can be regarded as being substantially free of oxygen.

The microstructures of the materials are shown in Fig. 1. The polished specimens were etched by Murakami's solution (100 ml water, 10 g sodium hydroxide, 10 g potassium ferricyanide). The silicon carbide is the grey phase and the free silicon is the white one. In material 1 large dark areas are seen, consisting of porous free carbon which did not react during processing. The porous free carbon is the reason for the great difference between the measured and calculated densities in Table 2. The silicon carbide phase usually consists of primary and secondary silicon carbide, the latter being formed by the reaction of carbon and silicon during infiltration of the preform.

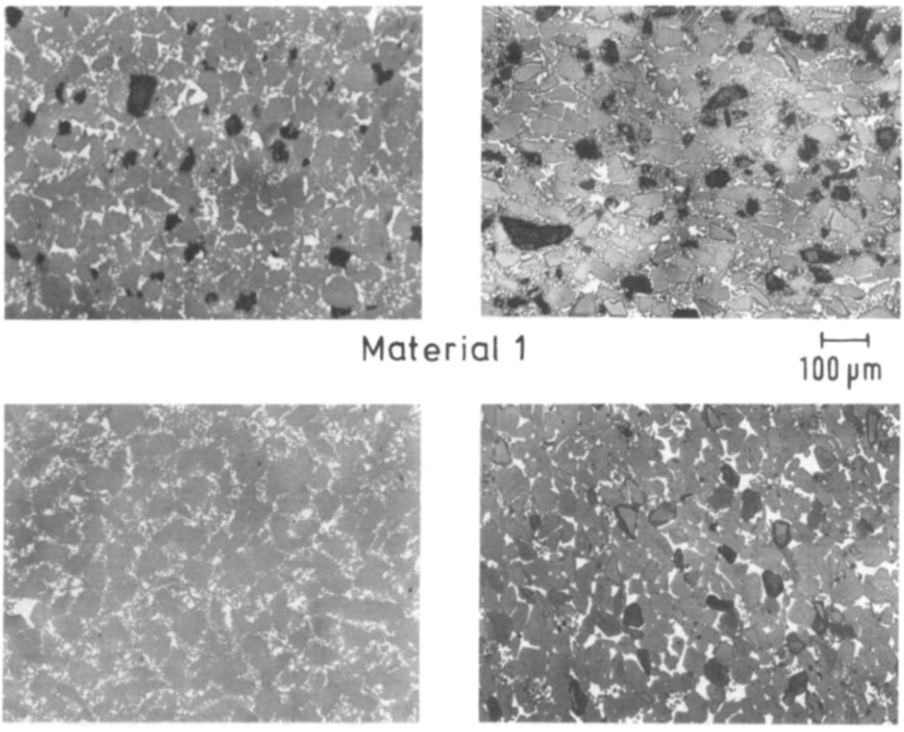

Fig. 1. Microstructure of the SiSiC materials. Left, unetched; right, etched by Murakami's solution.

By etching, boundaries within the silicon carbide structure become visible which makes possible a distinction between the coarse- and fine-grained primary silicon carbide and the secondary silicon carbide. It is not easy to distinguish between the fine-grained primary and the secondary silicon carbide.

By ceramographic investigation four typical defects in the microstructure of SiSiC were found (Fig. 2). The most frequent defects, especially in Material 1, were particles of free porous carbon (Fig. 2(a)) which were surrounded by a dense barrier of silicon carbide formed during the infiltration process. The silicon carbide barrier prevents the diffusion processes needed for transformation of the free carbon into secondary silicon carbide.

Sometimes large areas of free silicon were found in the microstructure (Fig. 2(b)). These defects may be due to bubbles in the slip which could not escape during preparation of the preform and were filled by free silicon during the infiltration process.

Cracks in the silicon carbide structure should be regarded as very critical

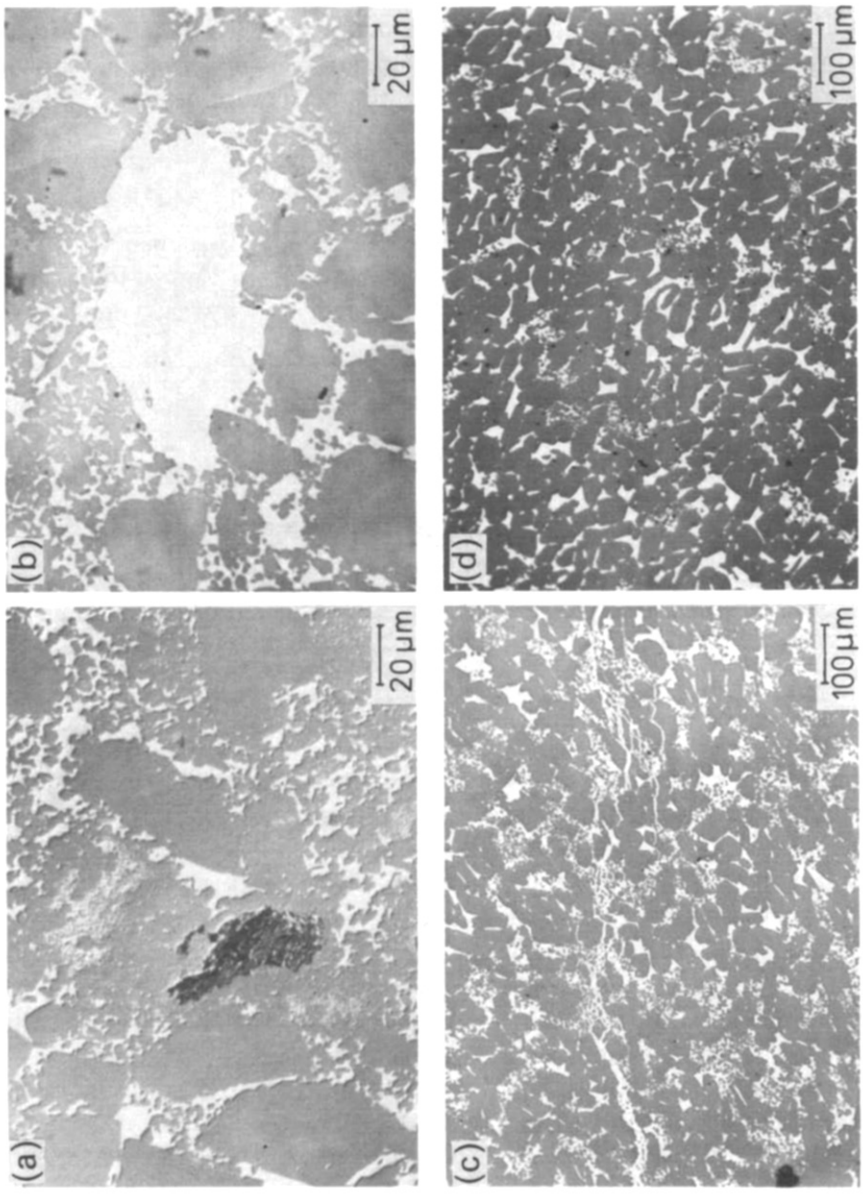

Fig. 2. Microstructure defects in SiSiC. (a) Inclusion of free carbon (Material 1); (b) large area of free silicon (Material 1); (c) crack in the silicon carbide structure filled by free silicon (Material 1); (d) inhomogeneous distribution of fine-grained silicon carbide (Material 2).

defects (Fig. 2(c)). These cracks can be initiated by the anomalous solidification behaviour of the free silicon, which shows, analogous to water, an expansion of about 10% by volume during solidification. The cracks sometimes reach a length of several millimetres and large silicon carbide grains can be made to split. Generally the cracks were filled with free silicon.

The inhomogeneous distribution of the fine-grained silicon carbide shown in Fig. 2(d) may be regarded as a further microstructure defect.

3. EXPERIMENTAL DETAILS

The creep tests were carried out on a 4-point bend specimen with the dimensions 4·5 mm × 3·5 mm × 45 mm. The main dimensions of the fixture are given in Fig. 3. The diameter of the rollers (d) was 3 mm. This

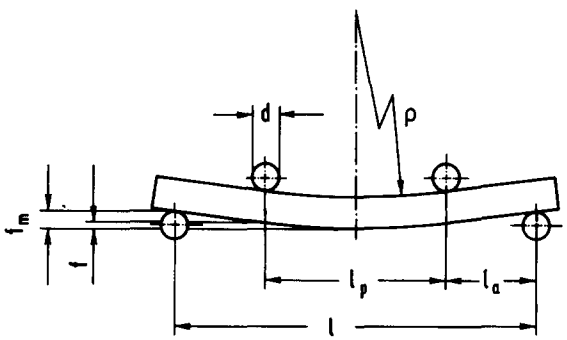

Fig. 3. Dimensions of the bend creep fixture ($l = 40$ mm, $l_a = 10$ mm, $l_p = 20$ mm, $d = 3$ mm).

configuration was taken as the standard for the bend test in the German research programme 'Keramische Komponenten für die Fahrzeug-Gasturbine'. To prevent any detrimental influence of the edges, these were provided with a 45°-bevel. The specimens were carefully ground along the direction of the long specimen axis.

The furnace was heated by a resistance heater and the temperature was controlled within the range of ±2 °C. The strain was measured as the deflection in the middle of the specimen by a linear variable displacement transducer (LVDT). Using the assumption of the theory of Bernoulli (i.e. plane cross-sections remain plane during creep), the strain, ε, of the outer tensile fibre can be calculated:

$$\varepsilon = \frac{2\rho}{h} = \frac{4h}{l_p^2} f \tag{1}$$

where ρ = radius of curvature of the neutral axis and h is the beam thickness (= 3·5 mm). For the definition of the other symbols see Fig. 3. The used

fixture allows only the measurement of the total deflection f_m. For this reason the interdependence:

$$\frac{f}{f_m} = 1 - 4\frac{l_a}{l} \cdot \frac{1 - \frac{4}{3}\frac{l_a}{l}}{1 - \frac{4}{3}\left(\frac{l_a}{l}\right)^2} \tag{2}$$

has to be taken into account.

For the calculation of the stress the linear elastic theory is used. The nominal stress of the outer fibres, σ_n, within the range of the inner rollers (range of constant moment) is:

$$\sigma_n = \frac{M}{W} \tag{3}$$

where M = bending moment and W = moment of resistance. The linear elastic theory is applied in spite of the well-known fact that the stress distribution within the bending specimen becomes nonlinear with time if the creep law is nonlinear (i.e. the power law of creep $\dot{\varepsilon} \sim \sigma^n, n > 1$ (Ref. 14)). In the nonlinear case the stress distribution depends on time and on the creep law itself; this fact is not generally known. Thus it seems to be convenient to operate with the linear elastic theory and to characterize the applied stress by the nominal stress, σ_n, of the outer fibres according to eqn (3).

In order to investigate the influence of oxidation effects on the creep of SiSiC the tests were carried out on specimens in the as-received state and on preoxidized materials. The preoxidation conditions were chosen to be 1350 °C and 200 h, in air.

4. RESULTS

All measured creep curves showed a decreasing creep rate, even under severe test conditions, after long test times up to 400 h. This is in good agreement with earlier publications.[1,3] Due to this fact it is not possible to characterize the creep mechanisms in a simple way by application of stationary creep rates. Creep of SiSiC is mainly of a transient nature.

To describe the creep curve of tin in 1911 Andrade[15] suggested the equation:

$$l(t) = l_0(1 + \beta' t^{1.3})\,e^{kt} \tag{4}$$

where $l(t)$ is the length of the specimen as a function of time t, l_0 is the initial length, and β' and k are constants. This equation was modified by Cottrell and Aytekin[16] who introduced a stationary creep rate, $\dot{\varepsilon}_s$:

$$\varepsilon(t) = \varepsilon_0 + \beta' t^{1.3} + \dot{\varepsilon}_s t \tag{5}$$

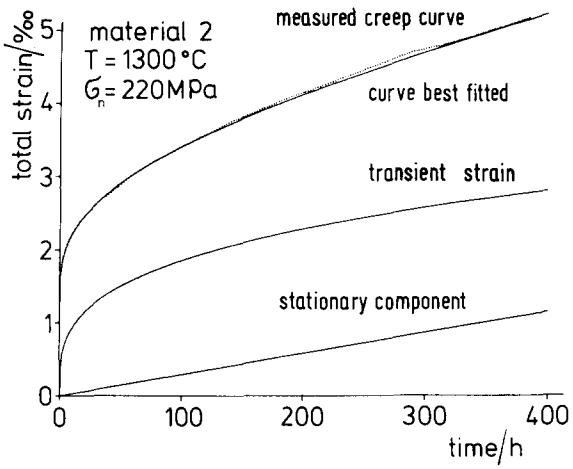

Fig. 4. Creep curve of SiSiC and comparison of measured curve with the curve best fitted.

where $\varepsilon(t)$ is the total strain, ε_0 is an instantaneous strain and $\beta' t^{1/3}$, with the constant β', is a transient strain. From eqn (5), with a general time exponent m and the dimensionless time (t/t_0), the strain–time relation can be written:

$$\varepsilon(t) = \varepsilon_0 + \beta\left(\frac{t}{t_0}\right)^m + \dot{\varepsilon}_s t \tag{6}$$

This equation describes the creep curve very well (Fig. 4). The parameters ε_0, β, m and $\dot{\varepsilon}_s$ can be calculated by a computer program using linear regression analysis.[17] From Fig. 4 it is seen that even at 400 h the contribution of transient strain to the total strain is significantly higher than the contribution of stationary strain $\dot{\varepsilon}_s t$. The strain rates indicated by the slope of the curves are of the same order for the transient and the stationary part of strain at this point.

Measurable stationary strain rates of the order of $\dot{\varepsilon}_s > 10^{-6}\,\mathrm{h}^{-1}$ could only be found in Material 1 under all test conditions. In Material 2 stationary strain rates could only be measured when the silicon carbide structure was damaged by cracks as in Fig. 2(c), or in cases of very severe test conditions.

For SiSiC a large scatter in the parameters of the creep curve is obtained.[17] For this reason a more complicated dependence of the parameters of transient creep on the nominal stress, σ_n, other than linearity, can not be seen. The method of least squares leads to an equation of the form:

$$y = (a \pm l_a) + (b \pm l_b)x \tag{7}$$

The constants a and b are supplemented by the 90%-confidence regions l_a

and l_b. The creep curve of SiSiC was measured at the following stress levels: 130, 160, 190 and 220 MPa.

Each measurement was repeated five times at a temperature of 1300 °C. Using this procedure the following dependences are found for the parameter describing the initial strain, ε_0, and the parameters for transient creep, β and m, for Material 1:

$$\begin{aligned}
\varepsilon_0[‰] &= -(0{\cdot}396 \pm 0{\cdot}136) + (8{\cdot}58 \pm 3{\cdot}52) \times 10^{-3}\sigma_n\ [\mathrm{MPa}] \\
\beta[‰] &= (0{\cdot}552 \pm 0{\cdot}033) - (1{\cdot}89 \pm 0{\cdot}84) \times 10^{-3}\sigma_n\ [\mathrm{MPa}] \\
m[1] &= (0{\cdot}034 \pm 0{\cdot}044) + (1{\cdot}39 \pm 1{\cdot}04) \times 10^{-3}\sigma_n\ [\mathrm{MPa}]
\end{aligned} \tag{8a}$$

and for Material 2:

$$\begin{aligned}
\varepsilon_0[‰] &= -(0{\cdot}151 \pm 0{\cdot}032) + (6{\cdot}32 \pm 2{\cdot}49) \times 10^{-3}\sigma_n\ [\mathrm{MPa}] \\
\beta[‰] &= (0{\cdot}448 \pm 0{\cdot}067) - (1{\cdot}31 \pm 1{\cdot}18) \times 10^{-3}\sigma_n\ [\mathrm{MPa}] \\
m[1] &= (0{\cdot}074 \pm 0{\cdot}035) + (1{\cdot}49 \pm 0{\cdot}62) \times 10^{-3}\sigma_n\ [\mathrm{MPa}]
\end{aligned} \tag{8b}$$

For Material 1 a stationary strain component which showed a large scatter was obtained at all test conditions. The results are plotted in the log–log plot shown in Fig. 5. From this diagram a stress exponent of $n = 5 \pm 1{\cdot}5 (\dot{\varepsilon}_s \sim \sigma^n)$ can be calculated by the method of least squares. For Material 2 such a diagram is not meaningful because stationary strain rates were obtained only at stress levels higher than 220 MPa.

The question arises as to at which stress level creep rupture occurs. On Material 1 at 1300 °C a nominal stress of 190 MPa could be applied without creep rupture within 200 h. But a nominal stress of 213 MPa ($\approx 70\%$ of

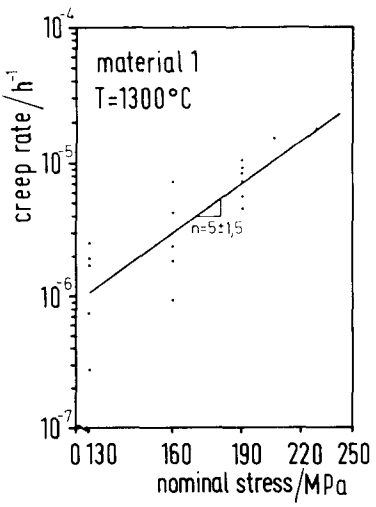

Fig. 5. Stress dependency of the stationary strain component.

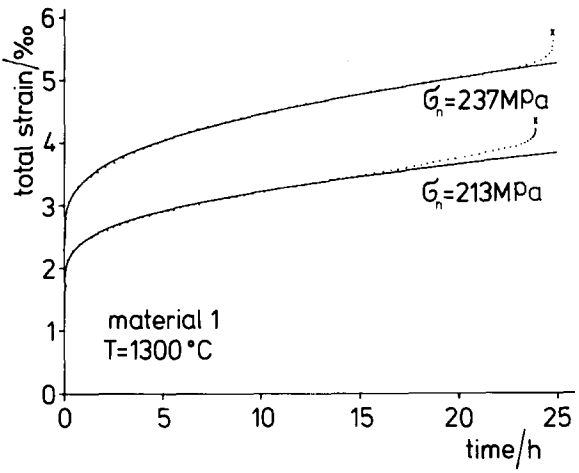

Fig. 6. Complete creep curve of SiSiC at very high stresses.

room temperature strength) led to creep rupture within 24 h (Fig. 6). The creep curves then show extensive tertiary creep before creep rupture occurs. From this creep curve a stationary creep rate of $\dot{\varepsilon} \approx 1{\cdot}5 \times 10^{-5}\,h^{-1}$ can be calculated by the procedure mentioned above. These creep rates are also plotted in Fig. 5. They are very well integrated in the band of scatter.

An interesting change in the creep mechanisms can be demonstrated by plotting the plastic strain, $\varepsilon_{pl} = \beta(t/t_0)^m + \dot{\varepsilon}_s t$, versus the nominal stress for different constant creep times (Fig. 7). It becomes clear that within the scattering band the strain at a constant time is independent of the stress for low nominal stresses, while at high stresses the strain increases significantly. The critical stress shifts to lower nominal stresses with increasing time at

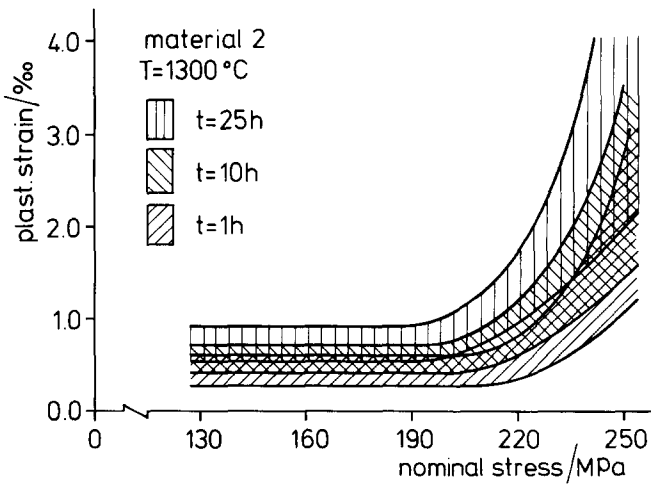

Fig. 7. Plastic strain versus nominal stress at different constant creep times.

TABLE 3
Comparison of the Parameters of Instantaneous and Transient Strain in the As-received and Preoxidized States

	$\varepsilon_0/‰$	$\beta/‰$	m/l
As-received state	$0{\cdot}810 \pm 0{\cdot}229$	$0{\cdot}213 \pm 0{\cdot}126$	$0{\cdot}182 \pm 0{\cdot}063$
Preoxidized 1 350 °C, 200 h	$0{\cdot}717 \pm 0{\cdot}247$	$0{\cdot}222 \pm 0{\cdot}078$	$0{\cdot}168 \pm 0{\cdot}044$

which the strain was taken. This finding indicates a necessary incubation time for reaching large strain values. The incubation time is lower the higher the nominal stress.

For determining the influence of oxidation on the creep of SiSiC, tests were carried out on Material 2 in the as-received state and in the preoxidized state. Table 3 gives the mean values and standard deviation of the instantaneous strain and the parameters of transient strain. The comparison shows no significant differences. This means that a severe oxidation treatment before creep testing does not influence the creep behaviour and the influence of oxidation on creep of SiSiC can, in general, be disregarded.

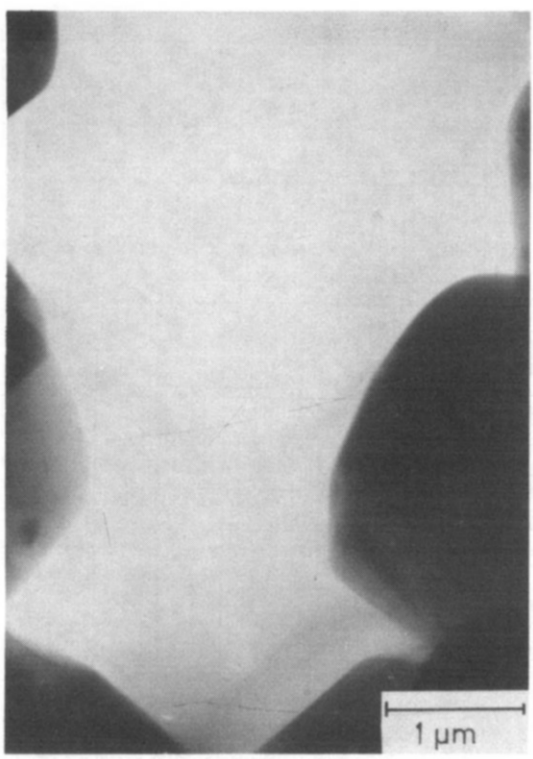

Fig. 8. TEM micrograph of Material 2 in the as-received state; silicon region free of any dislocation.

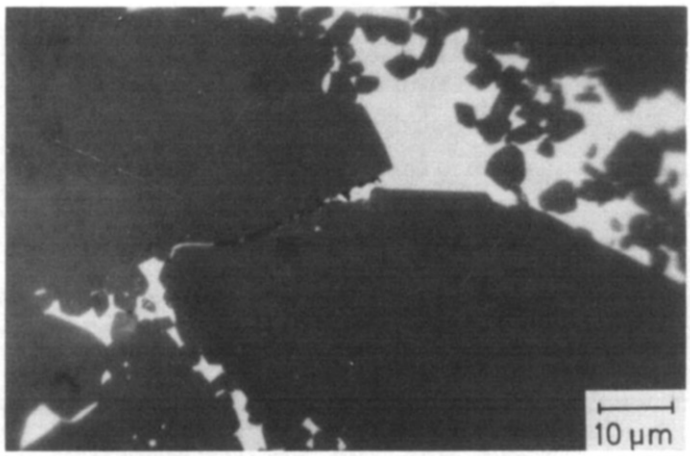

Fig. 9. Optical micrograph of Material 2 after 50 h creep at 1300 °C and 220 MPa.

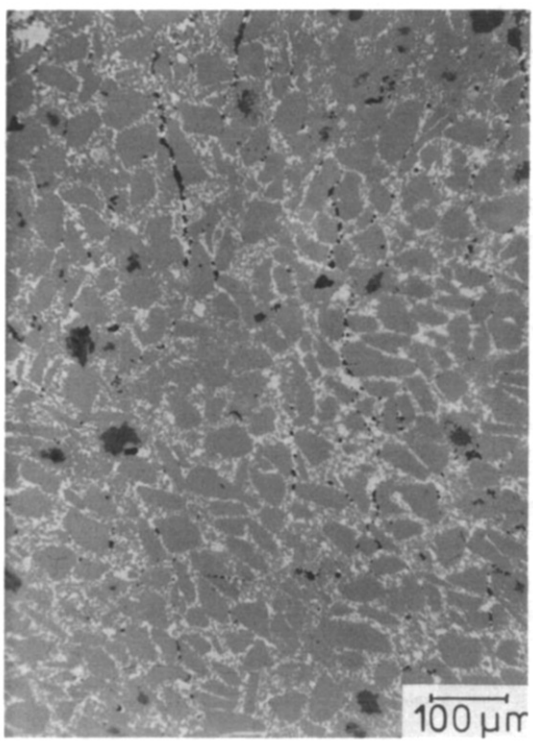

Fig. 10. Optical micrograph of Material 1 after 200 h creep at 1350 °C and 190 MPa.

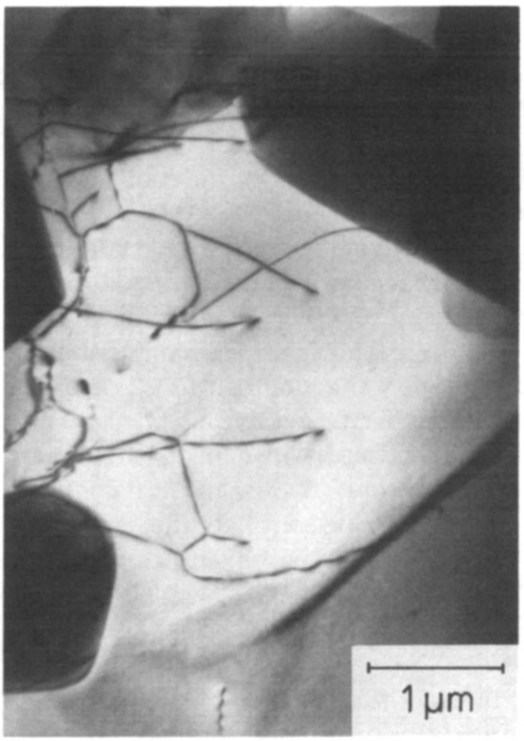

Fig. 11. TEM micrograph of silicon regions in Material 2 after 400 h creep at 1300 °C and 220 MPa.

Investigations by light microscopy and transmission electron microscopy (TEM) discovered some significant changes in the microstructure due to creep. In the as-received state no defects of microstructure other than those mentioned above could be discerned by light microscopy and only a few dislocations were found by TEM in the silicon carbide and silicon phases. In Fig. 8 a large region of free silicon, free of any dislocation, is shown. After a creep test when no stationary creep according to eqn (6) occurs, in general no influence of creep on the microstructure can be detected by light microscopy. In other cases microcracks appear between silicon carbide grains with grain boundaries perpendicular to the direction of the tensile stress (Fig. 9). In the later creep state the microcracks form pores which are arranged in planes also perpendicular to the direction of tensile stress (Fig. 10). After all creep tests a significant number of dislocations and twins were found in the silicon phase (Fig. 11). No change could be detected, however, in the configuration of dislocations in the silicon carbide grains. Cracks and pores were also found by TEM studies but it was not possible to decide whether they were due to creep or to the preparation of the TEM specimen.

5. DISCUSSION

The creep tests discovered a relatively large scatter of material behaviour which may be due to microstructural and chemical differences between the specimens. It was necessary to repeat the experiments five times for each test condition. By a statistical treatment of the results a good interpretation of material behaviour was possible.

The SiSiC material tested in the preoxidized state showed no significantly different mechanical behaviour from that in the as-received state. Therefore SiSiC can be regarded as a ceramic, the mechanical properties of which are not sensitive to oxidation. This fact makes discussion of the results easier. The creep curve of SiSiC was found to be well described by eqn (6).

The steady-state component, $\dot{\varepsilon}_s t$, was calculated only for Material 1 under all test conditions. In Material 2, with a much better microstructure, steady-state creep occurred only under very severe test conditions. Thus, creep of SiSiC may be regarded as being of a transient nature in general. By neglecting $\dot{\varepsilon}_s$ in eqn (6), differentiation with respect to time provides:

$$\dot{\varepsilon}(t) = m\beta\left(\frac{t}{t_0}\right)^{(m-1)} \tag{8a}$$

Equation (8) is of the same form as the more frequently used function for the description of transient creep:

$$\dot{\varepsilon}(t) = a\left(\frac{t}{t_0}\right)^{-c} \tag{8b}$$

with $c = (1 - m)$. In the case of $c = 1$, eqn (8) converts into the function of logarithmic creep:

$$\varepsilon(t) = a \ln\left(\frac{t}{t_0}\right) \tag{9}$$

Equation (9) has the disadvantage of unrealistic negative strain in the range $0 < (t/t_0) < 1$ and an infinite strain rate at the beginning of the creep test $(t \to 0)$. These disadvantages disappear when eqn (9) is written in the form:

$$\varepsilon(t) = a \ln\left(\frac{t}{t_0} + 1\right) \tag{10}$$

For long periods of times, eqn (10) converts into eqn (9). At $t =$ zero we obtain zero strain and the strain rate $\dot{\varepsilon}(t = 0) = a/t_0$.

Logarithmic creep indicates strain-hardening processes which can be described by an extended Norton creep law as follows:

$$\dot{\varepsilon} = A\sigma^n = A_0 \, e^{-B\varepsilon}\sigma^n \tag{11}$$

In this equation A_0, B and n are constants and the structure parameter A depends exponentially on the strain itself. For homogeneous stress distribution (i.e. in tension test) integration by time leads to:

$$\varepsilon(t) = \frac{1}{B} \ln (BA_0\sigma^n + 1) \tag{12}$$

Equation (12) shows the same form as eqn (11) with $a = 1/B$ and $t_0 = 1/(BA_0)$. This derivation indicates the relationship of logarithmic creep with the transient creep according to eqn (8) and therefore the mechanisms may be discussed in the same manner.

Logarithmic creep was found in metals at very low temperature where recovery processes do not occur. Deviations from this creep behaviour are known in the literature as hyperbolic creep ($c > 1$) and parabolic creep ($c < 1$).[18] In metals logarithmic creep was interpreted as increasing activation stress for dislocation motion. However, in ceramic materials this consideration is not realistic because dislocation motion does not seem to be the mechanism controlling the deformation. SiSiC consists of very stiff and less deformable silicon carbide grains embedded in the ductile silicon phase. In the undeformed material there exist a number of contacts between the silicon carbide grains. Carter and co-workers[13] investigated the SiC–SiC contacts by TEM and found no free silicon within these contacts. During creep new contacts are generated and the total area of contacts becomes larger because of local plastic deformation in the silicon carbide grains at high stress concentrations. This results in a hardening effect and also in a material behaviour dependent on strain, which may be described by a function similar to eqn (11).

The mechanisms may be discussed by regarding the microstructure in Figs 8 and 9. Before creep only a few dislocations were found in the silicon carbide and in the silicon phases. After creep the dislocation configuration in the silicon carbide phase had not changed, but in the free silicon the number of dislocations and twins increased significantly. Thus, the creep deformation of the silicon phase is controlled by dislocation motion, which is consistent with results given in the literature, where it is shown that deformation of silicon is controlled by dislocation glide. Diffusion-controlled dislocation motion was not found in silicon at temperatures up to near the melting point.[19,20]

Consequently, the strain hardening of SiSiC is not caused by the silicon phase but by the silicon carbide skeleton. The mechanisms may be deformation processes in the volume of the silicon carbide grains caused by dislocation motion or by diffusion processes and resulting in an increase of the summarized contact area. Another hardening mechanism may be the rearrangement of silicon carbide grains, resulting in a stiffer silicon carbide

skeleton. Substantial dislocation motion in silicon carbide is only possible at temperatures above 2000 °C;[21,22] thus, only local deformation by dislocation motion at highly stressed contacts may be possible. In the same way the possibilities for diffusion processes are only limited because the test temperature was approximately half of the melting point of silicon carbide (3100 K). Regarding the local stress concentration at the contacts of silicon carbide grains, both mechanisms should be possible. Nevertheless, they do not allow a large deformation of SiSiC without damage of the microstructure. The free silicon does not control the deformation because it is very easy to deform at the test temperature.[23]

The interpretation of the stationary strain component according to eqn (6) is somewhat difficult. The stress exponent of Material 1, according to the classical Norton creep law ($\dot{\varepsilon}_s = \text{const} \times \sigma^n$), was found to be $n = 5$ (Fig. 5). Such n-values are usually correlated with diffusion-controlled dislocation motion. Such a creep mechanism, however, cannot be realistic for SiSiC as shown above. Another possible interpretation is damage to the microstructure. In Fig. 9 the formation of microcracks is shown. The formation of cavities and microcracks leads to the lowering of the Young's modulus and therefore to an additional strain component.

Such a steady-state deformation process does not seem to be controlled by processes being in equilibrium. When the deformation is associated with continuous damaging the resulting creep rate in general should not be constant with time. However, an additional 'deformation' process occurs which may change or even terminate the declining character of the creep curve. At a certain time quasi-steady-state creep may emerge.

The responsible damaging may be regarded as a two-step process. The first step is the microcrack nucleation, which has been correlated to a nearly constant strain rate; the second is microcrack growth leading to an increasing strain rate. Hasselmann *et al.*[24–26] calculated the stress exponent for this so-called 'elastic creep' to be $n > 3$. Therefore the stress exponent calculated in Fig. 5 may be interpreted by the formation and later growth of the microcracks, the latter probably leading also to the formation of creep porosity, arranged in planes perpendicular to the direction of the tensile stress (Fig. 8), and resulting in an increasing strain rate with the possible consequence of creep rupture.

The question arises as to whether or not a threshold stress for initiation of the formation and growth of microcracks exists. For Material 2 stationary strain components could only be calculated at nominal stresses above 220 MPa. By looking at Fig. 7 a threshold stress becomes more clear. The significant increase of strain above 200–220 MPa should be interpreted by microcrack formation and crack growth activated above this stress. From Fig. 7 it is also seen that the threshold stress shifts to lower values when the

time for which the strain is taken is increased. The processes leading to crack initiation and growth are therefore stress- and time-dependent.

When a critical stress concentration in the silicon carbide structure is needed for crack initiation and growth, its time dependency can be explained as follows. At the beginning of bending creep possibilities for local deformations and rearrangement of silicon carbide grains exist and the critical stress concentration will not be reached at any silicon carbide contacts in the specimen. With increasing time the initial deformation mechanism will be blocked more and more (strain hardening). The stress concentrations increase and may perhaps reach the critical value at one of the silicon carbide silicon carbide contacts. A crack will be initiated and at this contact the stress concentration decreases. So, the microcrack will not propagate at first and the stress concentration increases at other silicon carbide -silicon carbide contacts.

Therefore, to reach higher stress concentrations a certain deformation by creep is needed. The time necessary for this process is shorter, the higher the nominal stress. The time for reaching the critical stress concentration may be correlated with the incubation time for reaching higher strain values in Fig. 7.

By this procedure the silicon carbide structure will be weakened more and more, and after a certain time the microcracks will begin to grow and contribute to the creep porosity shown in Fig. 10 and also to strain. The time at which microcrack growth occurs may be regarded as stress-dependent; thus, the shifting of the threshold stress to lower values in Fig. 7 may be explained.

6. CONCLUSION

Reaction-bonded siliconized silicon carbide with a well-defined microstructure shows a very good creep behaviour that is not sensitive to severe oxidation treatment. The creep is of a transient nature and can be described by an extended Norton creep law considering the strain-hardening behaviour of the material. The deformation of SiSiC is controlled by the silicon carbide skeleton, while the free silicon is very ductile and easy to deform under the applied test conditions. Small local deformations of the silicon carbide grains by dislocation motion or diffusion processes are responsible for the transient creep. Also, some rearrangement of the silicon carbide grains may be possible. These processes cause the strain hardening. The total deformation that can be reached without disturbance of the microstructure is very limited. Steady-state creep components occur only at high stress levels, creating microcracks and creep porosity within the

microstructure. Creep rupture occurs only above a threshold stress and is due to the growth of microcracks at high stress concentrations.

REFERENCES

1. Marshall, P., The relationship between delayed fracture, creep and texture in silicon carbide, *Special Ceramics*, **4** (1967) 191–203.
2. Rumsey, J. C. V. and Roberts, A. L., Delayed fracture and creep in silicon carbide, *Proc. Brit. Ceram. Soc.*, **7** (1967) 233–45.
3. Marshall, P. and Jones, R. B., Creep of silicon carbide, *Powder Metallurgy*, **12** (1969) 193–208.
4. Adams, R. M., The creep of silicon carbide; its measurement and mechanisms, Ph.D. Thesis, University of Leeds, 1972.
5. Osborne, N. J., Creep testing of high temperature engineering ceramics, *Proc. Brit. Ceram. Soc.*, **25** (1975) 263–80.
6. Seltzer, M., *High Temperature Creep of Ceramics*, Rept. No. AD-A 031 760, 1976.
7. Krishnamachari, V. and Notis, M. R., Interpretation of high temperature creep of SiC by deformation mapping techniques, *Mat. Sci. Eng.*, **27** (1977) 83–8.
8. Larsen, D. C., Borth, S. A., Ruh, R. and Tallan, N. M., Evaluation of four commercial Si_3N_4 and SiC materials for turbine application, in *Ceramics for High Performance Application II*, Eds J. J. Burke, E. N. Lenoe and R. N. Katz, Brook Hill, Chestnut Hill, Massachusetts, 1978, 651–67.
9. Wirth, G., Gephart, W. and Schönau, W., *Zug- und Biegekriechverhalten sowie Biegebruchfestigkeit von HP- und RB-Silizium-Karbid bei hohen Temperaturen an Luft*, DFVLR-Bericht IB 354-78/3, 1978.
10. Schnürer, K., Kriechverhalten verschiedener SiC-Materialien im Vakuum und an Luft, Dissertation Universität Karlsruhe, 1979, KfK-Bericht 2883.
11. Schnürer, K., Grathwohl, G. and Thümmler, F., Kriechverhalten verschiedener SiC-Werkstoffe, *Science of Ceramics*, **10** (1980) 645–52.
12. Gugel, E., Leimer, G., Cohrt, H., Grathwohl, G. and Thümmler, F., Gasturbinenbauteile aus reaktionsgesintertem SiC und deren mechanische Hochtemperatureigenschaften, in *Keramische Komponenten für Fahrzeug-Gasturbinen II*, Eds. W. Bunk and M. Böhmer, Springer-Verlag, Berlin, 1981.
13. Davis, R. F., Carter, C. H. Jr, Chevacharoenkul, S. and Bentley, J., The occurrence and behavior of dislocations during plastic deformation of selected transition metal and silicon carbides, in *Deformation of Ceramic Materials II*, Eds R. E. Tressler and R. C. Bradt, Plenum Press, New York, 1984.
14. Cohrt, H., Grathwohl, G. and Thümmler, F., Non-stationary stress distribution in a ceramic bending beam during constant load creep, *Res Mechanica*, **10** (1984) 55–71.
15. Andrade, C., On the viscous flow in metals and allied phenomena, *Proc. Roy. Soc.*, **A84** (1911) 1–12.
16. Cottrell, A. H. and Aytekin, V., Andrade's creep law and the flow of zinc crystals, *Nature*, **160** (1974) 328–9.
17. Cohrt, H., *Mechanik und Mechanismen des Biegekriechens von reaktionsgebundenem Siliziumkarbid*, KfK-Bericht 3731, 1984.

18. Seeger, A., Theorie der Kristall-Plastizität, *Z. Naturforschung*, **9a** (1954) 758–75.
19. Reppich, B., Haasen, P. and Ilschner, B., Kriechen von Silizium-Einkristallen, *Acta Met.*, **12** (1964) 1283–8.
20. George, A., Escaravage, C., Champier, G. and Schröter, W., Velocities of screw and 60°-dislocation in silicon, *Phys. Stat. Sol. (b)*, **53** (1972) 483–96.
21. Frantsevich, I. N., Kravets, V. A., Egorov, L. O., Nazarenko, K. V. and Smusherich, V. S., High-temperature deformability of α-SiC, *Soviet Powder Metallurgy*, **10** (1971) 229–31.
22. Frantsevich, I. N., Kravets, V. A. and Nazarenko, K. V., Investigation of α-SiC plastic strain, *Poroshkovaya Met.*, **15** (1975) 89–93.
23. Sylwestrowicz, W. D., Mechanical properties of single crystals of silicon, *Phil. Mag.*, **7** (1962) 1825–45.
24. Hasselmann, D. P. H., Venkateswaran, A. and Shih, C., Elastic creep of brittle ceramics with special reference to creep by crack growth in aluminium oxide, in *Surfaces and Interfaces in Ceramic and Ceramic–Metal Systems*, Eds J. A. Pask and A. G. Evans, Plenum Press, New York, 1981.
25. Venkateswaran, A. and Hasselmann, D. P. H., Elastic creep of stressed solids due to time dependent changes in elastic properties, *J. Mat. Sci.*, **16** (1981) 1627–32.
26. Hasselmann, D. P. H. and Venkateswaran, A., Role of cracks in the creep deformation of brittle polycrystalline ceramics, *J. Mat. Sci.*, **18** (1983) 161–72.

Received 29 May 1985; accepted 15 July 1985

Int. J. High Technology Ceramics 1 (1985) 107–118

Sintering and Strength of Silicon Nitride–Silicon Carbide Composites

Hidehiko Tanaka*, Peter Greil and Günter Petzow

Max-Planck Institut für Metallforschung, Institut für Werkstoffwissenschaften, Pulvermetallurgisches Laboratorium, Heisenbergstr. 5, D-7000 Stuttgart 80, FRG

SUMMARY

The sintering, microstructure, fracture toughness and strength of silicon carbide-dispersed silicon nitride composite systems were investigated. The composite powders could be sintered with aluminium oxide and yttrium oxide additives at normal pressure. Nearly complete densification was achieved by hipping presintered compacts. The silicon carbide particle dispersion retarded both grain and pore growth during sintering. The strength was found to increase with silicon carbide content, whereas fracture toughness remained constant. Thus strengthening of the composite is attributed to the decrease in flaw size.

1. INTRODUCTION

Silicon nitride and silicon carbide materials exhibit excellent high temperature mechanical properties and are candidates for application as structural materials in heat engines. Improvement of the mechanical properties of silicon nitride and silicon carbide-based materials has also focused on the dispersion of second-phase particles.[1–5] Dispersed zirconium dioxide or hafnium dioxide particles of up to 20 vol.% were found to increase the fracture toughness.[6,7] This was attributed to the stress-induced tetragonal to monoclinic phase transformation of zirconium dioxide or the formation of microcracks in the matrix. Lange,[1] and Wei and Becher[4] reported that the fracture toughness can also be increased by silicon

* Present address: National Institute of Research in Inorganic Materials, Sakura-mura, Ibaraki-ken, Japan.

Int. J. High Technology Ceramics 0267-3762/85/$03·30

carbide particle dispersion in a silicon nitride matrix and likewise by titanium carbide particles in silicon carbide. Usually, the particle-dispersed silicon nitride or silicon carbide matrix materials were prepared by hot-pressing, because the second phase did not promote densification. Common sintering additives able to sinter both matrix and second-phase particles were seldom found.

Fine silicon nitride powder can be sintered easily by the addition of aluminium oxide and yttrium oxide,[8] resulting in microstructures with glassy or crystalline grain boundary phases, respectively. Omori and Takei[9] found that the combination of aluminium oxide and yttrium oxide can also be used to sinter silicon carbide powder under normal pressure. The densification process in both systems is supposed to be dominated by a liquid-phase sintering mechanism, where the liquid is formed by the oxide additives and the silicon dioxide impurity content of the powders. Thus the Al_2O_3–Y_2O_3 oxide system seems to be a possible sintering additive for a silicon carbide-dispersed silicon nitride matrix material, i.e. silicon nitride–silicon carbide composite.

In this work the pressureless sintering of silicon nitride–silicon carbide composites with the additives aluminium oxide and yttrium oxide was investigated. Hot isostatic pressing (hipping) was applied to provide further densification. The effects of silicon carbide dispersion on the microstructure formation and the mechanical properties of the composite were studied.

2. EXPERIMENTAL

Pure and fine grain α-Si_3N_4 powder (H. C. Starck, LC 10) and β-SiC powder (H. C. Starck, B 10) were used as the starting materials. These modifications are both low temperature forms. The mean grain sizes of the silicon nitride and silicon carbide powders were 0·5 and 1·0 μm, respectively. The powders containing fixed amounts of silicon nitride and silicon carbide were mixed with aluminium oxide (Alcoa, A 16) and yttrium oxide (Ventron, 4 N) powders by the attritor mill, and cold isostatically pressed at 630 MPa.

These powder compacts were subsequently sintered in a graphite element furnace under 0·1 MPa nitrogen. The bend strength and the fracture toughness were measured at room temperature. Inner and outer spans for 4-point bend tests were 20 and 40 mm, respectively. The indentation strength-in-bending technique (ISB)[10] was used for measuring fracture toughness. Indentation forces were 29·4–196·2 N and the span of the 3-point bend test for ISB was 12 mm.

The microstructure of the specimens was observed by scanning electron microscopy (SEM) on the polished and etched surfaces. Molten sodium

hydroxide and Murakami's reagent were used as the etching materials. The molten sodium hydroxide etched the oxynitride grain boundary phase and the Murakami's reagent etched the silicon carbide grains. From the photomicrographs the areas of pores and grains which appeared on the polished and etched surfaces were counted and measured.

Hipping was performed with nitrogen at 100 MPa and 2000 °C. The samples were presintered at 1850 °C and were not encapsulated. The strength and fracture toughness of the hipped samples were also measured.

3. RESULTS AND DISCUSSION

3.1. Sintering

Figure 1 shows the density of sintered silicon nitride as a function of the total amount of oxide additives and the content of aluminium oxide in the additive. From the results given in Fig. 1, it was decided that the amount of oxide additive for the pressureless sintering of silicon nitride–silicon carbide composite materials should be 15 wt % and the weight content of aluminium oxide in the additive, $Al_2O_3/(Al_2O_3 + Y_2O_3)$, was chosen as 0·7.

Figure 2 shows the relationship between the weight fraction of silicon carbide and the relative density of the composites which were sintered in the temperature range 1600–1850 °C. The sinterability of the silicon nitride–silicon carbide composite powder was found to be lower than that of

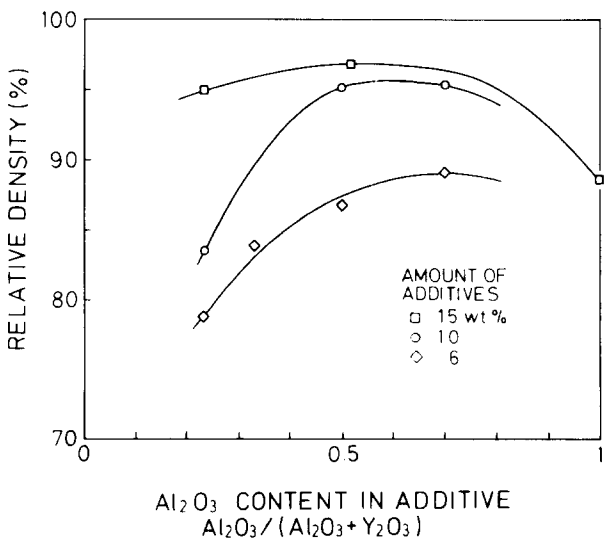

Fig. 1. Sintering density of silicon nitride powder with yttrium oxide and aluminium oxide additions. The sintering was carried out at 1800 °C for 30 min.

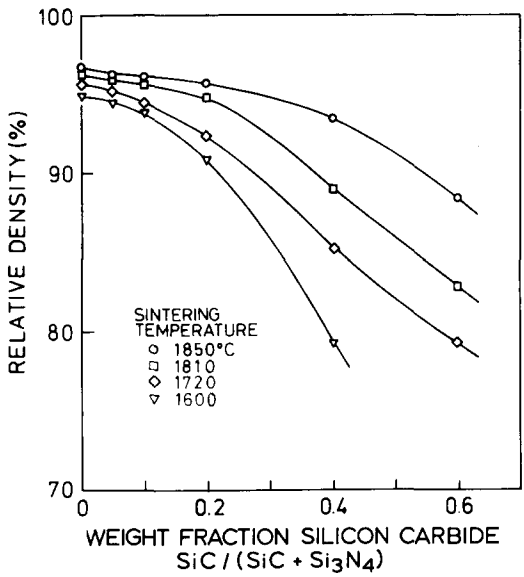

Fig. 2. Density of silicon nitride–silicon carbide composites as a function of the weight fraction [SiC/(SiC + Si_3N_4)] of silicon carbide content. Samples were sintered with 10·5 wt % aluminium oxide and 4·5 wt % yttrium oxide in the temperature range 1600–1850 °C for 1 h.

pure silicon nitride, but it was possible to sinter it to nearly the same density as silicon nitride if the composite contained less than 20 wt % silicon carbide and it was sintered at 1850 °C. The powder X-ray diffraction measurement detected only β-Si_3N_4 and β-SiC phases in the sintered samples. Silicon nitride transformed completely from α- to β-phase, but the silicon carbide remained β-SiC.

Figure 3 shows the microstructure of the sintered composites. The optical micrographs reveal the β-SiC grains in bright contrast lying in the dark silicon nitride matrix. Figure 4 shows a SEM micrograph of the surface etched by Murakami's reagent. The silicon carbide grains exhibit rough surfaces and are very well dispersed in the continuous silicon nitride matrix. The bonding between silicon carbide and silicon nitride seems to be strong. It is suggested that the oxide melt wetted both silicon carbide and silicon nitride grains during sintering.

3.2. Strength and microstructure

Table 1 lists the results of strength and fracture toughness measurements of the composites. All samples were sintered with 10·5 wt % aluminium oxide and 4·5 wt % yttrium oxide at 1850 °C. The strength was found to increase with the silicon carbide dispersion up to a silicon carbide fraction of 0·1. The fracture toughness, however, did not exhibit any increase with silicon

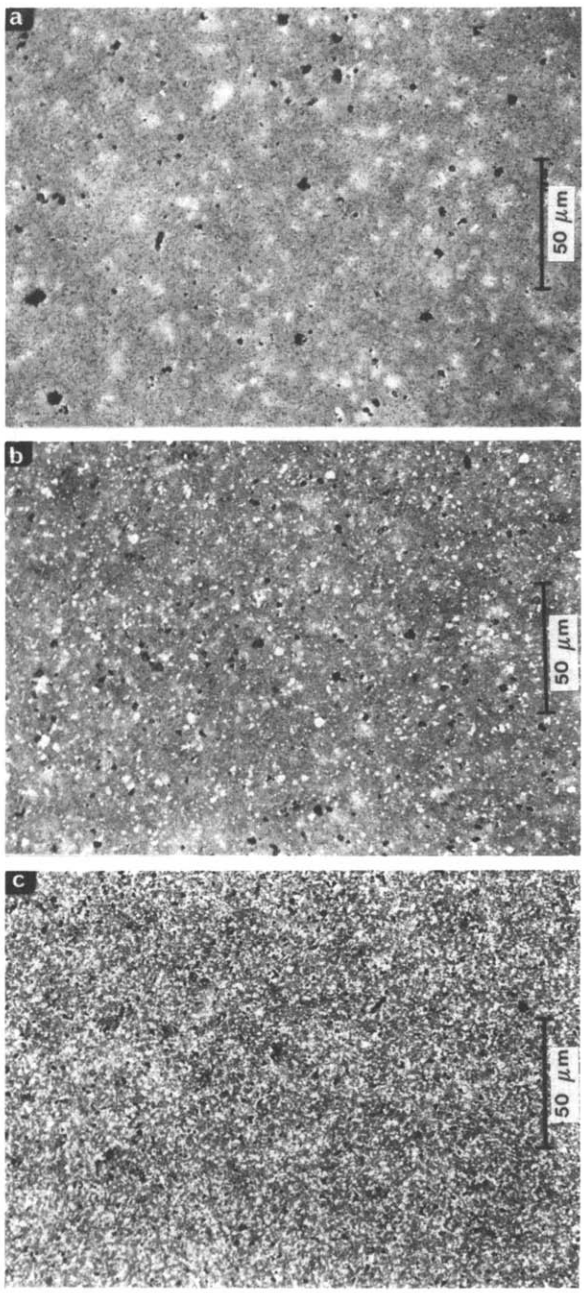

Fig. 3. Optical micrographs of polished surfaces. Weight fraction silicon carbide contents are (a) 0, (b) 0·2 and (c) 0·4. (Additive composition 10·5 wt % aluminium oxide and 4·5 wt % yttrium oxide; sintering conditions 1850 °C for 1 h.)

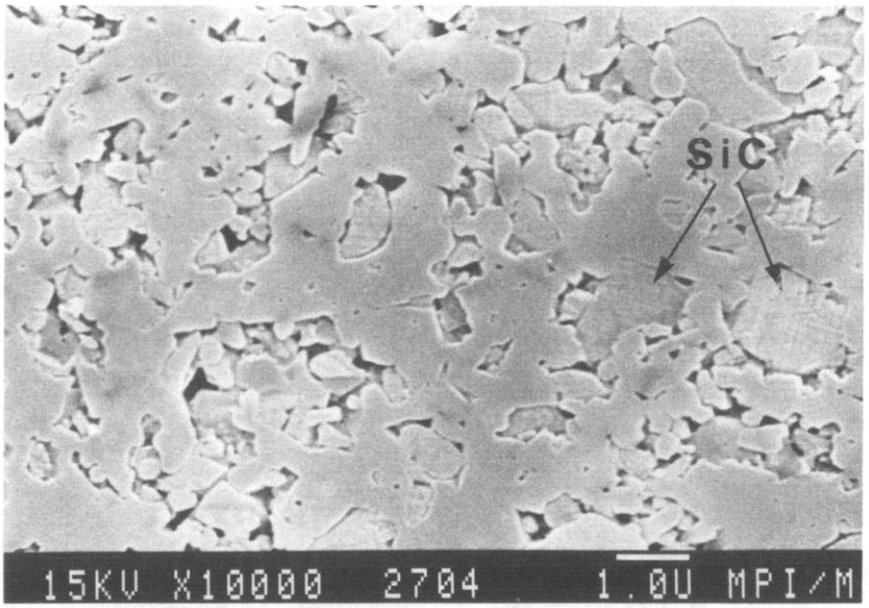

Fig. 4. SEM photograph showing silicon carbide grains in a silicon nitride matrix. The composite contains a silicon carbide weight fraction of 0·4 and was etched by Murakami's reagent. (Additives and sintering conditions as for Fig. 3.)

TABLE 1
Strength and K_{Ic} of Normal Sintered Composites

Sample		σ/*MPa*	K_{Ic}/$MN\,m^{-1.5}$	c/μm
$SiC/(SiC+Si_3N_4)$	ρ/% *theoretical*			
0	96·0	348 ± 108	3·95 ± 0·13	100
0·05	95·3	405 ± 28		
0·1	94·9	439 ± 31	3·94 ± 0·11	63
0·2	92·0	273 ± 56		
0·4	91·7	208 ± 57	3·17 ± 0·15	180
0·6	87·0	291 ± 78		

$SiC/(SiC+Si_3N_4)$ = content of SiC.
ρ = relative density at 20 °C.
σ = mean 20 °C 4-point bend strength.
K_{Ic} = mean 20 °C fracture toughness by ISB method.
c = expected flaw size calculated from σ and K_{Ic}.

carbide dispersion. Samples containing a silicon carbide fraction of 0·2 or more show lower strength and fracture toughness, which can be attributed to the increasing residual porosity after sintering.

Concerning the mechanical properties of the particle-dispersed ceramic, there are many mechanisms which are supposed to strengthen the matrix materials. Internal stresses due to thermal expansion or elasticity mismatch affect the strength. The proposed mechanisms are the prestressing of the dispersed phase,[11] the deflection of the propagating crack by a stress field[4,12] and energy dissipation by microcracking.[13–15] The dispersed particles can also act as obstacles to the crack propagation. The effects of crack pinning[16] and the crack deflection by inclusions have been reported to be effective in ceramic composite systems.[1,17]

All the mechanisms mentioned above mainly increase the fracture toughness, K_{Ic}, of the composite material as compared to the pure matrix material.[18] The strengthening effect is therefore mainly attributed to the increase of the fracture toughness if the critical flaw size remains unchanged by particle dispersion.

In this work an increase of fracture strength with silicon carbide dispersion was found, but the fracture toughness remained fairly constant. The toughening mechanism did not appear. Thus the increase of fracture strength may be explained by the decrease of the critical flaw size due to dispersed silicon carbide particles. Table 1 summarizes the results of an estimation of the critical flaw size, c, which was calculated from the fracture strength, σ_B, and fracture toughness, K_{Ic}, by using the Griffith equation $c = (K_{Ic}/Y\sigma_B)^{1/2}$, with Y equal to 1·13 when a penny-shaped crack is assumed. The smallest flaw size at fracture was estimated to be about 60 μm in the specimen containing a silicon carbide fraction of 0·1.

Figure 5 shows the microstructures of the samples containing a silicon carbide fraction of 0 and 0·2. The silicon carbide-containing microstructure clearly reveals a smaller grain size and a better homogeneity as compared to the silicon carbide-free sintered silicon nitride; this is also confirmed by the optical micrographs of the polished surfaces given in Fig. 3. The results of quantitative microstructure analysis are given in Fig. 6. The mean areas of pores and grains are plotted against the weight fraction of silicon carbide in the composite in a semi-logarithmic scale. The mean pore and grain sizes decrease with increasing weight fraction of silicon carbide. It follows that the dispersion of silicon carbide particles in the silicon nitride matrix retarded both pore and grain growth during sintering. The mean pore and grain diameters of $\sim$ 1–2 μm and even their maximum values (7 μm for the grains and 12 μm for the pores) do not correspond to the estimated critical flaw size.

Thus the silicon carbide dispersion seems to result in a shift of the pore and grain size distributions to smaller sizes after pressureless sintering with a

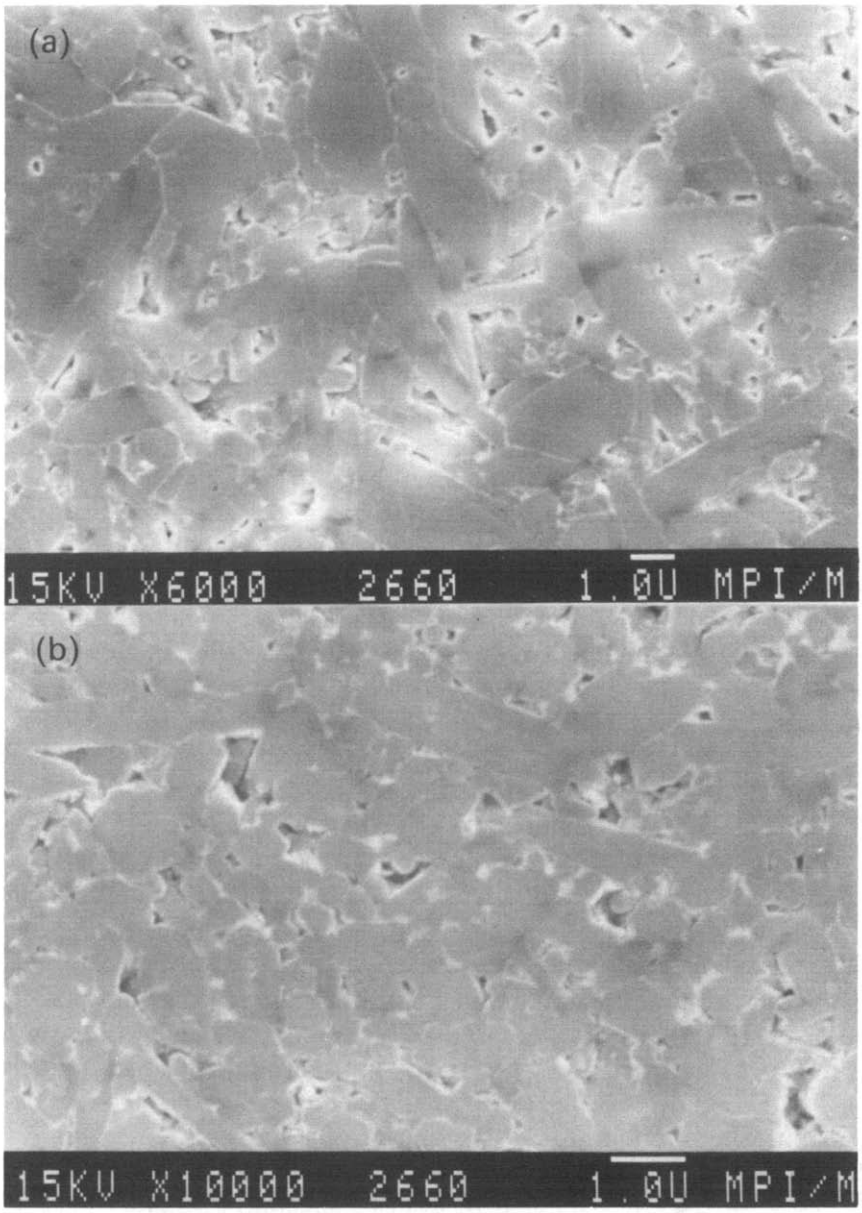

Fig. 5. Microstructure of (a) silicon carbide-free sintered silicon nitride; (b) composite containing a silicon carbide fraction of 0·2.

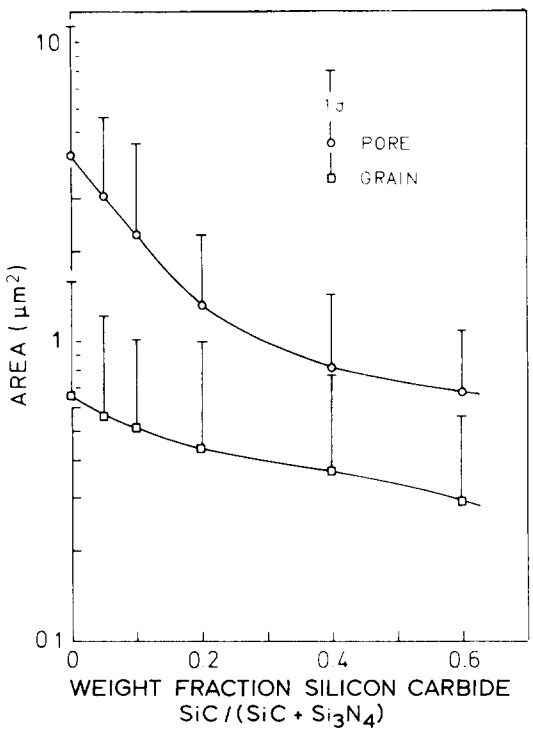

Fig. 6. Mean pore and grain areas as a function of weight fraction of silicon carbide content in the composite. The mean values were obtained by the counting of 100–280 pores and 230–300 grains on the SEM photographs.

more homogeneous microstructure as compared to the silicon carbide dispersion-free silicon nitride material.

3.3. Strength of composite after hipping

The results of the strength measurements suggest that the decrease in fracture strength in silicon carbide-rich composites is mainly attributed to residual porosity after pressureless sintering. Hipping was applied so that complete densification could also be attained in composites containing a silicon carbide fraction of $> 0{\cdot}2$. The results of the hipping treatment are given in Fig. 7 and Table 2. After hipping, the densities were calculated to be $\sim 97\%$ of theoretical density in the samples with a silicon carbide fraction of 0–0·4, and 96% in the sample with a fraction of 0·6.

Pressure-assisted densification of silicon nitride ceramics during hipping was reported to be strongly time-dependent.[19] In this investigation, hipping for 10 min and 50 min at 2000 °C resulted in almost the same densities. Thus 10-min hipping seemed to be sufficient for densification even though a small amount (2–3%) of residual porosity still remained.

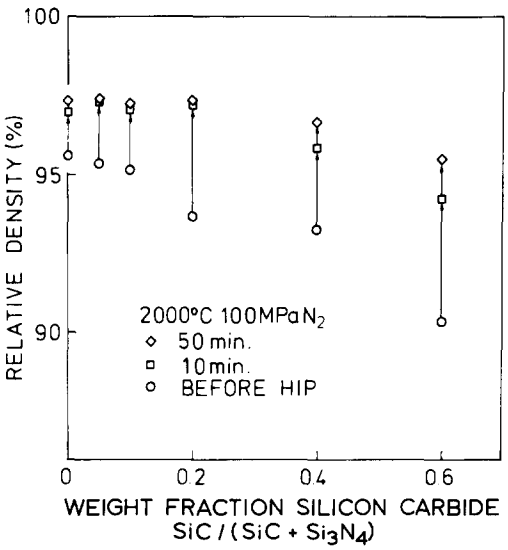

Fig. 7. Increase in relative density after hipping at 2000 °C and 100 MPa nitrogen pressure for 10 min and 50 min.

The mechanical properties of the hipped samples are listed in Table 2. A distinct improvement of fracture strength occurred, whereas fracture toughness was slightly degraded by silicon carbide dispersion. A mean fracture stress of 561 MPa was determined in the specimen containing a silicon carbide fraction of 0·4 with a fracture toughness of only 3·3 MN $m^{-3/2}$. The results show that the main effect of hipping is to decrease the flaw size in the composite system. The small pore size and good homogeneity of the presintered silicon carbide–silicon nitride composite

TABLE 2
Strength and K_{Ic} after Hipping

Sample		σ/*MPa*	K_{Ic}/*MN* $m^{-1.5}$	c/μ*m*
$SiC/(SiC+Si_3N_4)$	ρ/% *theoretical*			
0	96·9	352 ± 33	3·85 ± 0·20	95
0·1	96·6	491 ± 101	3·55 ± 0·35	41
0·4	96·6	561 ± 38	3·30 ± 0·08	27

$SiC/(SiC+Si_3N_4)$ = content of SiC.
ρ = relative density at 20 °C.
σ = mean 20 °C 4-point bend strength.
K_{Ic} = mean 20 °C fracture toughness by ISB method.
c = expected flaw size calculated from σ and K_{Ic}.

microstructure seem to be particularly suitable for the application of hipping to silicon nitride-based materials.

4. CONCLUSIONS

The sintering and mechanical properties of silicon carbide dispersed in a silicon nitride matrix composite were investigated. The mixture of α-Si_3N_4 and β-SiC fine powders could be sintered at normal pressure with aluminium oxide and yttrium oxide additives. The composites with silicon carbide fractions of 0·05 and 0·1 had higher strength than the sintered silicon nitride. Silicon carbide dispersion retarded both grain and pore growth, but did not toughen the composite materials. Thus strengthening is explained by a reduction of the critical flaw size. The hipping process was effective in further densifying the presintered silicon carbide-containing composites. Strengths improved after hipping and increased with silicon carbide content. Further hipping markedly decreased the flaw size in the composite system.

REFERENCES

1. Lange, F. F., Effect of microstructure on the strength of Si_3N_4–SiC composite system, *J. Am. Ceram. Soc.*, **56** (1973) 445.
2. Mah, T., Mendiratta, M. G. and Lipsitt, H. A., Fracture toughness and strength of Si_3N_4–TiC composites, *Am. Ceram. Soc. Bull.*, **60** (1981) 1229.
3. Faber, K. T. and Evans, A. G., Intergranular crack deflection toughening in silicon carbide, *J. Am. Ceram. Soc.*, **66** (1983) C94.
4. Wei, G. C. and Becher, P. F., Improvements in mechanical properties in SiC by addition of TiC particles, *J. Am. Ceram. Soc.*, **67** (1984) 571.
5. Greskovich, C. and Palm, J. A., Observations on fracture toughness of β-Si_3N_4–β-SiC composites, *J. Am. Ceram. Soc.*, **63** (1980) 597.
6. Claussen, N. and Jahn, J., Mechanical properties of sintered and hot-pressed Si_3N_4–ZrO_2 composites, *J. Am. Ceram. Soc.*, **61** (1978) 94.
7. Gauckler, L. J., Lorenz, J., Weiss, J. and Petzow, G., Improved fracture toughness of SiC-based ceramics, *Sci. Ceram.*, **10** (1980) 577.
8. Smith, J. and Quackenbush, C. L., A study of sintered Si_3N_4 compositions with Y_2O_3 and Al_2O_3 densification additives, in *Proc. Int. Symp. Factors in Densification and Sintering of Oxide and Non-oxide Ceramics*, Eds S. Sōmiya and S. Saito, KTK Publ. Tokyo, 1978, 426.
9. Omori, M. and Takei, H., Pressureless sintering of SiC, *J. Am. Ceram. Soc.*, **65** (1982) C92.
10. Anstis, G. R., Chantikul, P., Lawn, B. R. and Marshall, D. B., A critical evaluation of indentation techniques for measuring fracture toughness. I, direct crack measurements, *J. Am. Ceram. Soc.*, **64** (1981) 533.
11. Evans, A. G., The role of inclusions in the fracture of ceramic materials, *J. Mat. Sci.*, **9** (1974) 1145.

12. Nadeau, J. S. and Dickson, J. I., Effect of internal stress due to a dispersed phase on the fracture toughness of glass, *J. Am. Ceram. Soc.*, **63** (1980) 517.
13. Davidge, R. W. and Green, T. J., The strength of two phase ceramic/glass materials, *J. Mat. Sci.*, **3** (1968) 629.
14. Kreher, W. and Pompe, W., Increased fracture toughness of ceramics by energy dispersive mechanisms, *J. Mat. Sci.*, **16** (1981) 694.
15. Evans, A. G. and Faber, K. T., Toughening of ceramics by circumferential microcracking, *J. Am. Ceram. Soc.*, **64** (1981) 394.
16. Lange, F. F., The interaction of a crack front with a second phase, *Phil. Mag.*, **22** (1970) 983.
17. Faber, K. T. and Evans, A. G., Crack deflection processes, *Acta Met.*, **31** (1983) 565.
18. Rice, R. W., Mechanisms of toughening in ceramic matrix composites, *Ceramic Engineering and Science Proc.*, **2** (1981) 661.
19. Hirota, H., Ichikizaki, T. and Yajima, Y., Hot isostatic pressing of normally sintered silicon nitride in nitrogen gas as pressure medium, *Yogo-Kyokai-Shi*, **92** (1984) 188.

Received 16 September 1985; accepted 28 October 1985

Int. J. High Technology Ceramics **1** (1985) 119–127

Phase Equilibrium Studies in Si_2N_2O-containing Systems: I. Phase Relations in the Si_2N_2O–Al_2O_3–Y_2O_3 System

G. Z. Cao, Z. K. Huang, X. R. Fu and D. S. Yan (T. S. Yen)

Shanghai Institute of Ceramics, Academia Sinica, Shanghai, People's Republic of China

SUMMARY

Sub-solidus phase relations have been studied in the Si_2N_2O–Al_2O_3–Y_2O_3 system. The results show that Si_2N_2O forms a small range of compositions with Al_2O^3 (O'ss) containing up to 15 m/o Al_2O_3, and that $2Y_2O_3 \cdot Si_2N_2O$ forms a continuous solid solution series with $2Y_2O_3 \cdot Al_2O_3$ (Jss). In the Si_2N_2O-rich corner of the system, Si_2N_2O reacts with Y_2O_3 at 1550°C to form Si_3N_4 and $Y_{10}(SiO_4)_6N_2$(H-phase). Four quaternary phase regions occur in this system:

H–Si_3N_4–$Y_2O_3 \cdot Si_2N_2O$–$3Y_2O_3 \cdot 5Al_2O_3$

H–Si_3N_4–$3Y_2O_3 \cdot 5Al_2O_3$–O'ss

H–Si_3N_4–O' ss–Si_2N_2O

H–$Y_2O_3 \cdot Si_2N_2O$–$3Y_2O_3 \cdot 5Al_2O_3$–$4Y_2O_3 \cdot Si_2N_2O \cdot Al_2O_3$

From the results of this work, the sub-solidus phase diagram and the isothermal section at 1550°C in the Si_2N_2O–Al_2O_3–Y_2O_3 system are presented. A large liquid-phase area near the Si_2N_2O–Al_2O_3 side that may effect the sintering of O'-sialon ceramics is reported. The difference between our results and those previously reported in the Si_3N_4–SiO_2–Y_2O_3 phase diagram is also discussed.

1. INTRODUCTION

In recent years silicon oxynitride ceramics as high temperature structural material have received more and more attention from the point of view of their excellent oxidation resistance at elevated temperature. Although

Int. J. High Technology Ceramics 0267-3762/85/$03·30

silicon nitride ceramics possess very high mechanical strength, their oxidation resistance at high temperatures can be significantly degraded by oxide additives used to promote the densification process. Therefore, a combination of silicon nitride matrix with silicon oxynitride grain boundary might give a material with both high strength and good oxidation resistance. Thus the investigation of the system containing Si_2N_2O is of interest. The present paper is based on the understanding that the reaction between Si_3N_4 and SiO_2 to form Si_2N_2O solid solution occurs essentially in the presence of Al_2O_3.[1] The current commercial 'sialon' ceramics are of the β'-form and have an overall composition quite close to the Si_3N_4–Al_2O_3–Y_2O_3 plane. They contain an oxygen-rich yttrium sialon glass and therefore the Si_2N_2O–Al_2O_3–Y_2O_3 plane should cut across the tie line joining β'-sialon to glass for this composition range. Hence, a study of the phase relationships in this system is of importance to the understanding of the grain boundary characteristics of the related silicon nitride ceramics and the preparation of two-phase β'- and O′-sialon ceramics.

Phase relationships previously reported in the Y_2O_3–Al_2O_3 system[2] show two stable compounds, $2Y_2O_3 \cdot Al_2O_3$ and $3Y_2O_3 \cdot 5Al_2O_3$, and one metastable compound, $Y_2O_3 \cdot Al_2O_3$, which has two phases. The low temperature form has the same structure as $Y_2O_3 \cdot Si_2N_2O$ but is only stable up to $\sim$1100 °C;[3] the high temperature form is stable above 1825 °C. In the Si_2N_2O–Y_2O_3 system there exist two compounds, $2Y_2O_3 \cdot Si_2N_2O$ and $Y_2O_3 \cdot Si_2N_2O$, corresponding to $2Y_2O_3 \cdot Al_2O_3$ and $Y_2O_3 \cdot Al_2O_3$, respectively, in the Y_2O_3–Al_2O_3 system. However, no compound similar to $3Y_2O_3 \cdot 5Al_2O_3$ has been found. A continuous solid solution can be formed between $2Y_2O_3 \cdot Si_2N_2O$ and $2Y_2O_3 \cdot Al_2O_3$.[4] As to the Si_2N_2O–Al_2O_3 system, no new compound has been found, but a certain amount of Al_2O_3 can enter into the crystal structure of Si_2N_2O, forming a partial solid solution, the so-called O′-sialon. The limiting solubility of Al_2O_3 in Si_2N_2O ss was reported by different authors to be 6 e/o Al^{3+} (equivalent to 8 m/o Al_2O_3),[5] or 20 m/o Al_2O_3.[6]

2. EXPERIMENTAL

The starting materials used were silicon oxynitride, aluminium oxide and yttrium oxide. Silicon oxynitride powder was synthesized in our laboratory and after analysis shown to have the composition, Si 57·17, N 24·83, and O 16·40 %, corresponding to $Si_{2.04}N_{1.77}O_{1.02}$ which is deficient in nitrogen, but powder X-ray diffraction showed a single phase of Si_2N_2O only. Aluminium oxide was prepared by the decomposition of ammonium aluminium sulphate and its purity reached 99·9 %. The yttrium oxide was a

high purity (99·99%) reagent produced by Shanghai Yuolong Chemical works. About 50 compositions were prepared with these starting materials. The powder mixes were milled, using an agate mortar, in 100% ethanol for 2 h, dried and cold isostatically pressed at 300 MPa into pellets.

The melting method was used to determine the liquid-phase area at 1550 °C. The pellets were placed in small boron nitride-coated and screw-topped graphite crucibles filled with boron nitride powder and fired for 1 h in a graphite heating furnace at 1550 °C in a nitrogen atmosphere. The molten area on the specimens was observed by its visual appearance and by microscopy. Similar firings were carried out at lower temperatures, thus decreasing the liquid-phase formation area until the eutectic was identified. The eutectic point was determined by means of differential thermal analysis (DTA) and high temperature microscopy observation.

For the determination of sub-solidus phase compositions, hot-pressing was used in order to promote reactions to reach equilibrium and to minimize weight loss. Powder mixtures were placed in graphite dies coated with boron nitride on the inner surface, and hot-pressed under a pressure of 20 MPa in a nitrogen atmosphere. The hot-pressing temperature used was 1400 °C for the compositions which could form a liquid phase at 1550 °C and was 1400–1550 °C for all other compositions. The phase compositions of the specimens after hot-pressing were detected by X-ray diffraction analyses. Energy dispersion analysis of X-ray (EDAX) was used to determine the solid solubility of Al_2O_3 in Si_2N_2O ss.

3. RESULTS AND DISCUSSION

3.1. Phase relations in two Si_2N_2O-containing binary systems

Results obtained for the Si_2N_2O–Al_2O_3 system show that no binary compound is formed and there is only a limited solid solution of Al_2O_3 in Si_2N_2O to form O′-sialon. The extent of solid solubility of Al_2O_3 in Si_2N_2O was determined to be 15 m/o by X-ray diffraction and by EDAX. For the former method the composition at which X-ray peaks of Al_2O_3 virtually disappeared on the join O′ ss–Al_2O_3 was considered as the limit of solid solubility.

In the Si_2N_2O–Y_2O_3 system experiments confirm the existence of two compounds, $2Y_2O_3 \cdot Si_2N_2O$ and $Y_2O_3 \cdot Si_2N_2O$. The latter is formed at a temperature as low as 1400 °C and is stable; its structure is the same as the low temperature form of $Y_2O_3 \cdot Al_2O_3$ (stable only up to ~1100 °C) in the Y_2O_3–Al_2O_3 system.[3] At the Si_2N_2O-rich corner, Si_2N_2O reacts at 1550 °C

with Y_2O_3 to form $Y_{10}(SiO_4)_6N_2$(H-phase) and Si_3N_4 (mainly α-form, with a little β) by the following reactions:

$$10Si_2N_2O + 6Y_2O_3 \rightarrow Y_{10}(SiO_4)_6N_2 + 4Si_3N_4 + Y_2O_3 \cdot Si_2N_2O$$

$$9Si_2N_2O + 5Y_2O_3 \rightarrow Y_{10}(SiO_4)_6N_2 + 4Si_3N_4$$

3.2. Sub-solidus phase relations in the Si_2N_2O–Al_2O_3–Y_2O_3 system

The main compositions studied and the results of X-ray diffraction phase analyses are shown in Table 1, and the sub-solidus phase diagrams of the Si_2N_2O–Al_2O_3–Y_2O_3 system constructed on the basis of these data are shown in Figs 1 and 2. In this quasi-ternary system, a continuous solid solution (J ss) is formed between $2Y_2O_3 \cdot Si_2N_2O$ and $2Y_2O_3 \cdot Al_2O_3$. The solid solution phase of $2Y_2O_3 \cdot Si_2N_2O$ and $4Y_2O_3 \cdot Si_2N_2O \cdot Al_2O_3$ forms a triangular phase area with $Y_2O_3 \cdot Si_2N_2O$. Another triangular phase area is formed by $3Y_2O_3 \cdot 5Al_2O_3$ and the solid solution phase between $2Y_2O_3 \cdot Al_2O_3$ and $4Y_2O_3 \cdot Si_2N_2O \cdot Al_2O_3$. The experimental results in the Y_2O_3-rich area are very similar to the phase diagram of the Si_3N_4–Y_2O_3–$AlN \cdot Al_2O_3$ system reported by Sun *et al.*[7] As some decomposition and reactions occur in the Si_2N_2O-rich corner

TABLE 1
Compositions Studied and X-ray Analysis Results for the Si_2N_2O–Al_2O_3–Y_2O_3 System

No.	Y_2O_3	Si_2N_2O	Al_2O_3	*Phases present*[a]	*Phase regions*[a]
1	8	1	1	Y_2O_3; J ss	Y_2O_3–J ss
2	6	2	1	J ss	
3	6	1	3	J ss; YAG	J ss–YAG
4	6	3	1	J ss; K	J ss–K
5	3	1	2	J ss; K; YAG	J ss–K–YAG
6	3	2	1	J ss; K; YAG	
7	1	1	0	K	
8	3	4	0	K; H; SN	K–H–YAG–SN
9	3	2	2	K; H; SN; YAG	
10	5	9	0	SN; H	
11	3	5	2	SN; H; YAG; O′	H–SN–YAG–O′
12	1	7	2	SN; H; YAG; O′	
13	1	9	0	SN; H; Si_2N_2O	SN–H–Si_2N_2O
14	1	8·5	0·5	SN; H; O′	
15	0	9	1	O′ ss	
16	0	1	1	O′; Al_2O_3	
17	2	9	9	YAG; O′; Al_2O_3	YAG–Al_2O_3–O′
18	2	2	6	YAG; O′; Al_2O_3	

[a] For key see Fig. 1 and text.

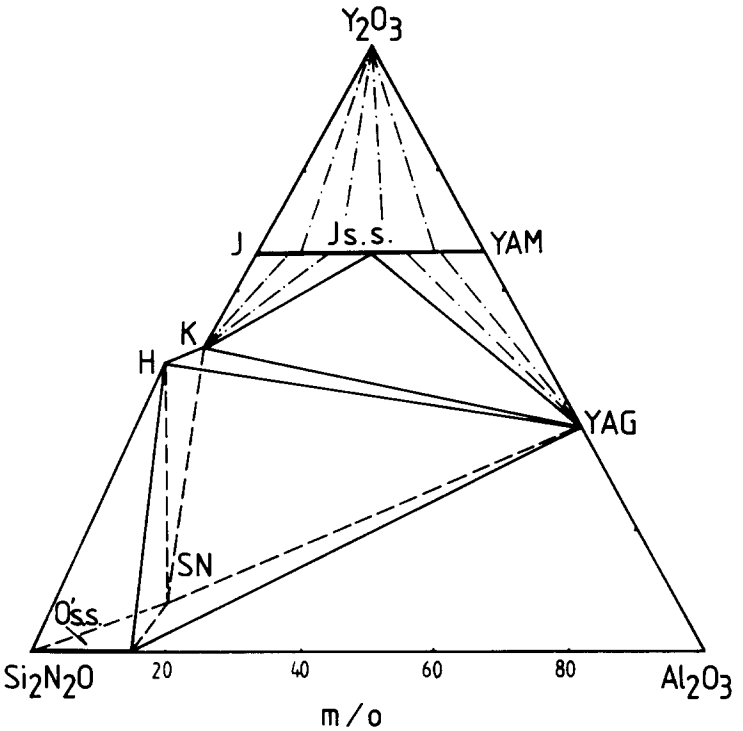

Fig. 1. Sub-solidus diagram of the Si_2N_2O–Al_2O_3–Y_2O_3 system. $J = 2Y_2O_3 \cdot Si_2N_2O$; $SN = Si_3N_4$; $YAM = 2Y_2O_3 \cdot Al_2O_3$; $K = Y_2O_3 \cdot Si_2N_2O$; $H = Y_{10}(SiO_4)_6N_2$; $YAG = 3Y_2O_3 \cdot 5Al_2O_3$.

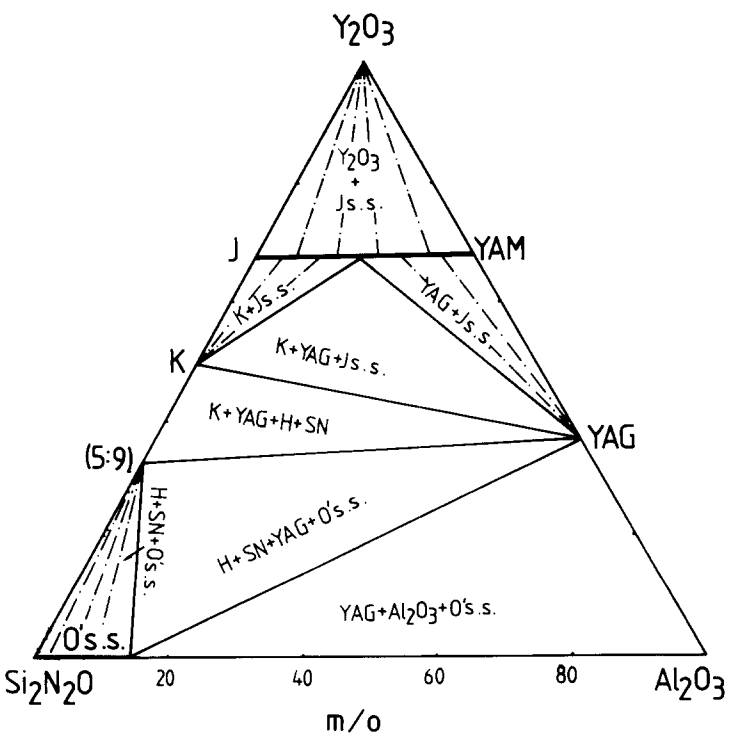

Fig. 2. Sub-solidus diagram of the Si_2N_2O–Al_2O_3–Y_2O_3 system. (5:9) Si_3N_4 and $Y_{10}(SiO_4)_6N_2$.

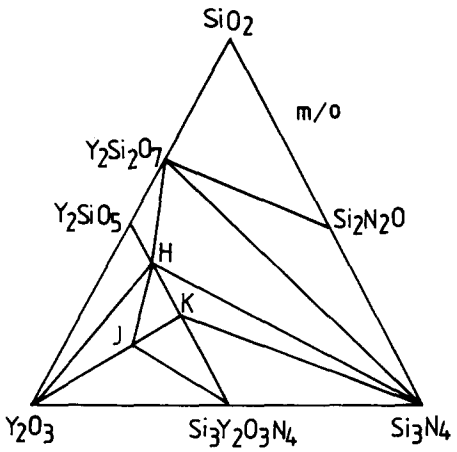

Fig. 3. Phase diagram of the Si_3N_4–SiO_2–Y_2O_3 system reported by Lange *et al.*[8]

of the Si_2N_2O–Y_2O_3 system, so in the Si_2N_2O-rich area of the Si_2N_2O–Al_2O_3–Y_2O_3 system several quaternary compatibility areas are formed:

$$H\text{–}Si_3N_4\text{–}Y_2O_3 \cdot Si_2N_2O\text{–}3Y_2O_3 \cdot 5Al_2O_3$$

$$H\text{–}Si_3N_4\text{–}3Y_2O_3 \cdot 5Al_2O_3\text{–}O' \text{ ss}$$

$$H\text{–}Si_3N_4\text{–}O' \text{ ss}\text{–}Si_2N_2O$$

$$H\text{–}Y_2O_3 \cdot Si_2N_2O\text{–}3Y_2O_3 \cdot 5Al_2O_3\text{–}4Y_2O_3 \cdot Si_2N_2O \cdot Al_2O_3$$

3.3. Review of the Si_3N_4–SiO_2–Y_2O_3 phase diagram

In the Si_3N_4–SiO_2–Y_2O_3 phase diagram previously reported,[8–10] Si_3N_4 is considered to be compatible with $Y_2O_3 \cdot 2SiO_2$ (Fig. 3). However, our experimental results in connection with the Si_2N_2O–Y_2O_3 system showed the contrary. Using either silicon oxynitride or a mix of silicon nitride and silicon dioxide, several samples in the composition range of

TABLE 2
Compositions Studied and X-ray Analysis Results for the Si_2N_2O–Y_2O_3 System

No.	Y_2O_3	Si_2N_2O	Si_3N_4	SiO_2	*Phases present*[a]
1	5	9	0	0	SN; H
2	5	0	4·5	4·5	SN; H
3	1	3	0	0	SN; H; Si_2N_2O
4	2	0	3	3	SN; H; Si_2N_2O

[a] For key see Fig. 1.

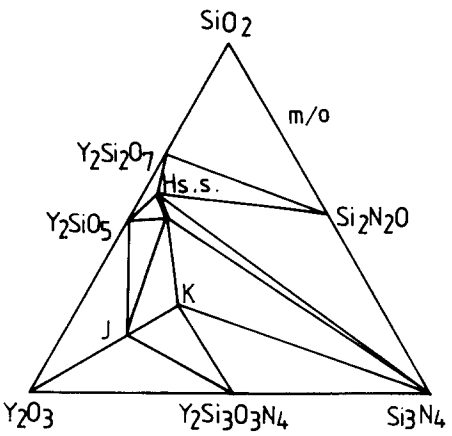

Fig. 4. Phase diagram of the Si_3N_4–SiO_2–Y_2O_3 system reported by Jack.[11]

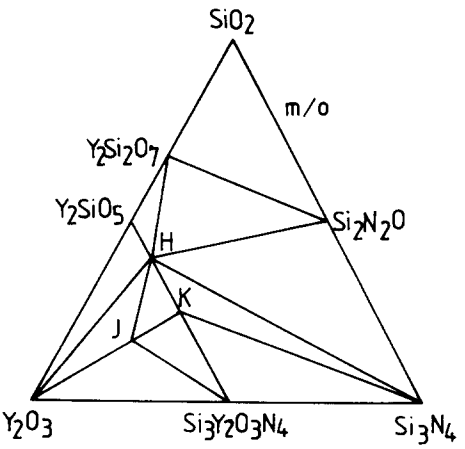

Fig. 5. Phase diagram of the Si_3N_4–SiO_2–Y_2O_3 system obtained in the present work.

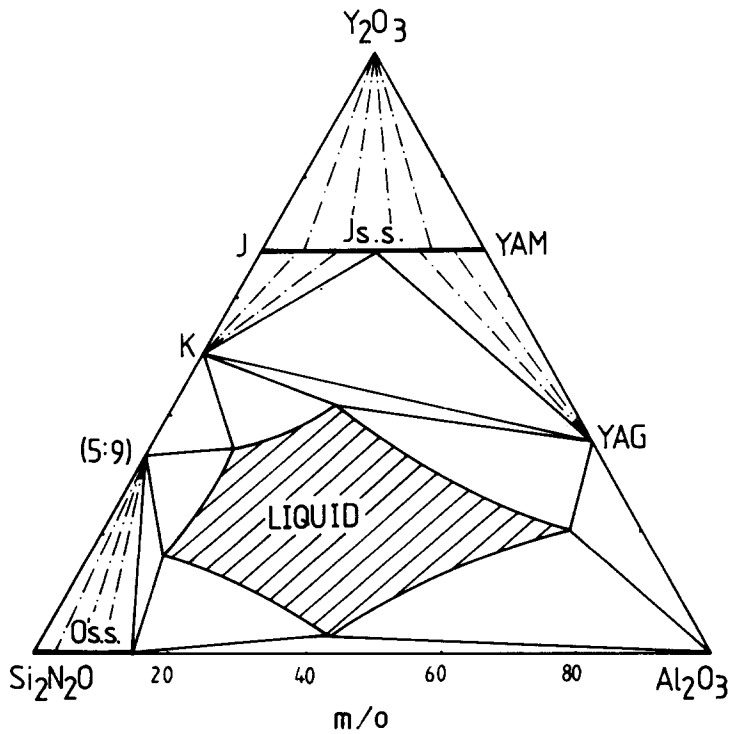

Fig. 6. Isothermal section at 1550 °C in the Si_2N_2O–Al_2O_3–Y_2O_3 system. $T_{eu} = 1450$ °C.

$Si_2N_2O:Y_2O_3 > 9:5$ were prepared and their phase analyses were performed. The results (Table 2) show that under a pure nitrogen atmosphere only $Y_{10}(SiO_4)_6N_2$ (H-phase) can be compatible with Si_3N_4, not $Y_2O_3 \cdot 2SiO_2$. This contradiction may be caused by the different experimental conditions used. The sub-solidus reaction immediately gave the H-phase. However, $Y_2O_3 \cdot 2SiO_2$ was only detected by the devitrification of glass,[8,9] indicating the difficulty of crystallization of a nitrogen-containing phase. This result is similar to that of Jack[11] (Fig. 4). The phase diagram of the Si_3N_4–SiO_2–Y_2O_3 system, based on the above results, is also presented (Fig. 5).

3.4. The isothermal section at 1550 °C of the Si_2N_2O–Al_2O_3–Y_2O_3 system

Using the melting method, a very large liquid-phase area at 1550 °C was identified near the Si_2N_2O–Al_2O_3 side in this system (Fig. 6). The small liquid-phase area in the Si_3N_4–SiO_2–Y_2O_3 system[10] is greatly enlarged with the addition of Al_2O_3. The eutectic in this liquid-phase area was detected to be $Y_2O_3:2Al_2O_3:2Si_2N_2O$ with $T_{eu} \sim 1450$ °C by means of DTA and high temperature microscopy observation. This liquid-phase formation phenomenon may have a considerable effect on the sintering of O′-sialon-containing ceramics.

4. CONCLUSIONS

1. The sub-solidus phase diagram of the Si_2N_2O–Al_2O_3–Y_2O_3 system is presented, in which no new compound has been found. The extent of solid solubility of Al_2O_3 in Si_2N_2O is defined as 15 m/o. For the Si_2N_2O–Y_2O_3 system all compositions of $Si_2N_2O:Y_2O_3 > 1:1$ decompose at high temperatures, forming Si_3N_4 and $Y_{10}(SiO_4)_6N_2$. As a result, four quaternary phase regions are formed in the Si_2N_2O–Al_2O_3–Y_2O_3 system.
2. In the Si_3N_4–SiO_2–Y_2O_3 system, Si_3N_4 was found to be compatible with $Y_{10}(SiO_4)_6N_2$, but not $Y_2O_3 \cdot 2SiO_2$, contrary to what was previously reported.
3. The isothermal section at 1550 °C of the Si_2N_2O–Al_2O_3–Y_2O_3 system is also presented, in which a large liquid-phase area near the Si_2N_2O–Al_2O_3 side was determined. It may have a considerable effect on the sintering of O′-sialon-containing ceramics.

REFERENCES

1. Huang, Z. K., Greil, P. and Petzow, G., *Ceramics International*, **10**(1) (1984) 14–17.

2. Levin, E. M., Robbins, C. R. and McMurdia, H. F., *Phase Diagrams for Ceramists*, American Ceramic Society, Columbus, Ohio, 1969, Fig. 2344.
3. Bertaut, F. and Mareschal, J., *Compt. Rend.*, **257** (1963) 867–70.
4. Naik, I. K. and Tien, T. Y., *J. Am. Ceram. Soc.*, **62** (1979) 642–3.
5. Naik, I. K., Gauckler, L. J. and Tien, T. Y., *J. Am. Ceram. Soc.*, **61** (1978) 332–5.
6. Sekercioglu, I. and Wills, R. R., *J. Am. Ceram. Soc.*, **62** (1979) 590–3.
7. Sun, W. Y., Huang, Z. K. and Cheng, J. X., *Trans. Brit. Ceram. Soc.*, **82** (1983) 173–5.
8. Lange, F. F., Singhal, S. C. and Kurnicki, R. C., *J. Am. Ceram. Soc.*, **60** (1977) 249–52.
9. Wills, R. R., Holmquist, S., Wimmer, J. M. and Cunningham, J. A., *J. Mat. Sci.*, **11**(7) (1976) 1305.
10. Gauckler, L. J., Hohnke, H. and Tien, T. Y., *J. Am. Ceram. Soc.*, **63**(1/2) (1980) 35.
11. Jack, K. H., in *Nitrogen Ceramics*. Ed. F. L. Riley, Noordhoff International, Reading, Mass., 1977, 109–28.

Received 10 April 1985; amended version received and accepted 29 October 1985

Int. J. High Technology Ceramics 1 (1985) 129–137

Crack Propagation Resistance of Aluminium Titanate Ceramics

Kenya Hamano, Yutaka Ohya and Zenbe-e Nakagawa

Research Laboratory of Engineering Materials, Tokyo Institute of Technology, 4259 Nagatsuta, Midori-ku, Yokohama-shi 227, Japan

SUMMARY

The crack propagation behaviour of aluminium titanate ceramics containing grain boundary microcracks has been investigated. The mean grain size of the aluminium titanate was 0·6 μm at 1300°C and 2·3 μm at 1500°C. Specimens sintered at 1450 and 1500°C contained grain boundary microcracks, while the specimen sintered at 1300°C had few cracks. Grain boundary microcracks decreased the bend strength and Young's modulus of the specimens. At the propagation of a crack, the microcracks deflected and caused branching of the crack, and blunted the crack tip; consequently, work of fracture of the specimen increased to more than twice the original value and crack propagation velocity decreased to 1/2000 of that in a microcrack-free aluminium titanate ceramic.

1. INTRODUCTION

Aluminium titanate ceramics are well known as low thermal expansion materials but have the disadvantage of low mechanical strength.[1,2] These two characteristics are due to grain boundary microcracks caused by a marked anisotropy of the thermal expansion of the aluminium titanate crystal.[1,3] In order to improve the mechanical strength, it is widely appreciated that a decrease in the size of cracks at the grain boundaries is necessary. In single-phase non-cubic polycrystalline ceramics, grain boundary microcracking occurs during the cooling period after sintering, under a set of conditions which is determined by their microstructure, thermal expansion anisotropy, fracture surface energy,

Int. J. High Technology Ceramics 0267-3762/85/$03·30

elastic moduli, and the difference between their sintering temperatures and room temperature.[4-6]

As aluminium titanate has a high thermal expansion anisotropy, in order to reduce the grain boundary microcracking, its grain size must be decreased markedly. Cleveland and Bradt[6] estimated that the 'transition grain size' for microcracking in aluminium titanate ceramics was 1–2 μm. One of the results of our study on the improvement of the mechanical strength of the aluminium titanate ceramics[7-10] showed that the transition grain size is 2·5 μm,[8] and that the bend strength of the sintered specimens increased suddenly as the grain size became smaller than this value.

Recently, several methods of toughening ceramic materials have been investigated; microcrack toughening[11-13] is one of these. Many researchers use K_{Ic} and the work of fracture to evaluate the toughness of the ceramic materials. In addition to these, the crack propagation velocity during fracture would be thought to be one of the significant evaluating factors. Although the crack velocity in fatigue fracture and slow crack growth has been measured, the fast crack velocity occurring during fracture has seldom been measured, because of the difficulties in making the measurement,[14] especially for opaque specimens.[15] Thus discussion of the relationship between crack velocity during fracture of the specimens and their microstructure has been rare.

In this paper the relationship between the microstructure of the aluminium titanate ceramics and their behaviour during fracture, i.e. crack propagation phenomena, crack velocity during fracture and work of fracture, has been investigated.

2. EXPERIMENTAL PROCEDURE

The sintered specimens were prepared from synthesized aluminium titanate powder having a mean particle size of $\sim 0{\cdot}5\,\mu$m and containing ~ 5 wt% aluminium oxide contaminant introduced during its ball-milling. Sintering temperatures were 1300, 1350, 1400, 1450 and 1500 °C, and the sintering period was 4 h. Thermal contraction and expansion of the specimens during the cooling period were measured by a non-loading type dilatometer.[16] Bend strengths were measured by the 3-point loading method, and the results were shown as the mean value of three specimens for each sintering condition. The microstructure and appearance of the side surfaces of the specimens after the bend test were observed using a scanning electron microscope. Work of fracture was determined, using a single-edge notched-beam specimen, by 3-point loading. The notch width was $\sim 0{\cdot}2$ mm and its

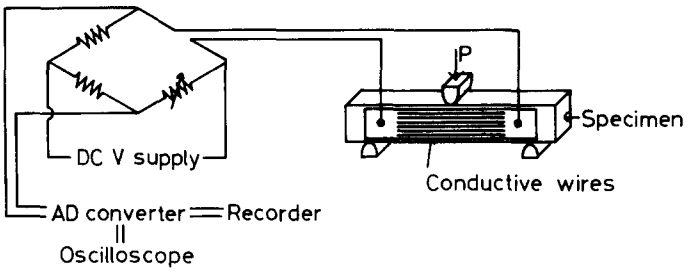

Fig. 1. Schematic diagram showing the experimental arrangement for measurement of crack velocity.

depth was ~ 40 % of the specimen thickness. Bulk density of the sintered specimens was measured by the mercury displacement method.

Crack propagation velocity during the fracture was determined as follows. Conductive wires which were connected to terminals at both sides were printed on a side surface of the sintered specimen and then baked. The width of each printed wire was ~ 0·2 mm, and the distance between each wire was also ~ 0·2 mm. When the crack propagates during fracture, it cuts the printed wires, and the electrical resistance between the terminals is increased. This change of resistance was transformed to a voltage by means of a Wheatstone bridge, and was then recorded as a function of time. The very rapid change in voltage required the use of an ultra-high-speed A–D converter with a digital memory (Transient Converter TCG-4000S, Riken Denshi Co., Ltd). This equipment has a maximum resolution of 0·05 μs/word and can memorize 4096 words. A schematic diagram of the experimental arrangement for measurement of the crack velocity is shown in Fig. 1.

3. RESULTS AND DISCUSSION

3.1. Grain boundary cracking and microstructure

During cooling subsequent to sintering, grain boundary cracking occurs, due to the high thermal expansion anisotropy of the aluminium titanate, and this cracking causes expansion of the specimens.[17] Figure 2 shows the thermal contraction and expansion curves of the specimens during cooling from their sintering temperatures. Every specimen changed from a contraction to an expansion at temperatures in the range 300–200 °C. The specimen sintered at 1400 °C expanded ~ 1 %, the largest value in this set of experiments. Specimens sintered at 1350, 1450 and 1500 °C expanded by ~ 0·3–0·5 %; the specimen sintered at 1300 °C showed very little expansion.

Figure 3 shows the fractured surfaces of the sintered specimens. The mean grain size of the titanate increased from 0·6 μm following sintering at 1300 °C to 2·3 μm at 1500 °C. The specimen sintered at 1400 °C had large and

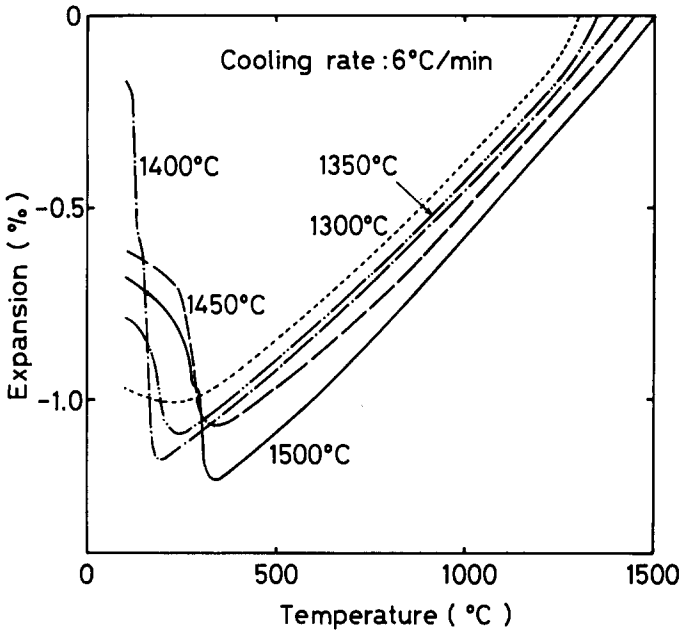

Fig. 2. Thermal contraction and expansion curves obtained during cooling from the sintering temperatures.

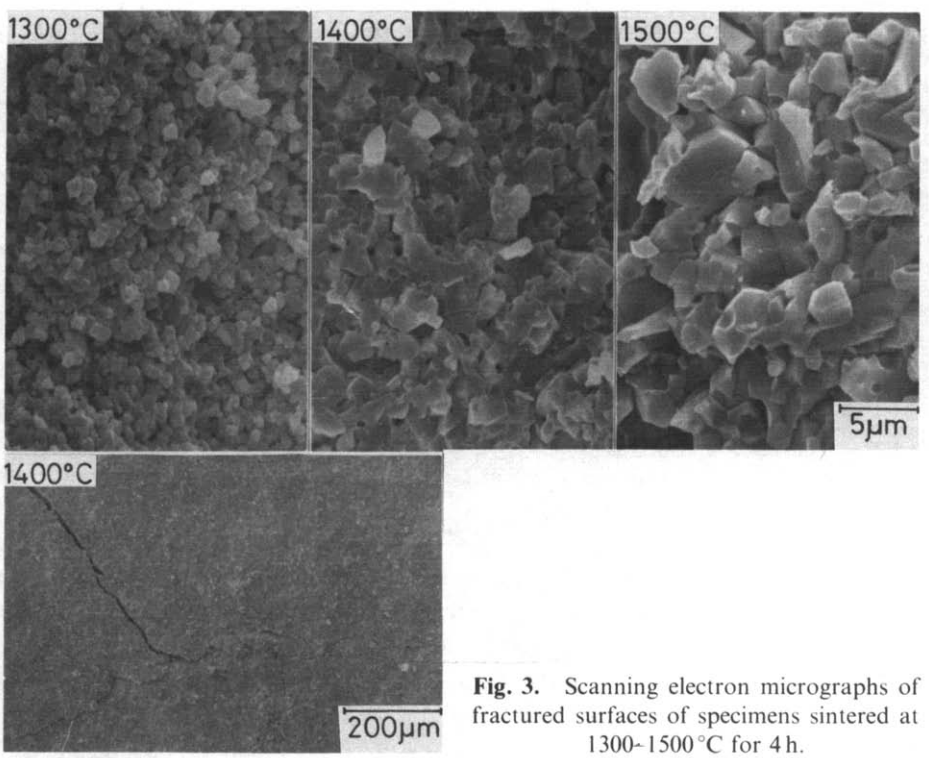

Fig. 3. Scanning electron micrographs of fractured surfaces of specimens sintered at 1300-1500 °C for 4 h.

continuous cracks through the body and failed when cooled to room temperature. Specimens sintered at 1450 and 1500 °C had small grain boundary microcracks and the microcracks of the 1450 °C specimen appeared to be continuous. The specimen sintered at 1300 °C had few cracks. The degree of microcracking and the size of the cracks in the sintered specimens can be seen to correspond with the degree of expansion during cooling.

3.2. Mechanical properties of sintered specimens

Bend strengths and bulk densities of the sintered bodies are shown in Fig. 4. The specimen sintered at 1400 °C had already fractured during cooling, so the bend strength of this specimen was considered as 0 MPa. The specimen sintered at 1300 °C, which contained few cracks, showed the highest strength. The specimens sintered at 1350 and 1450 °C were weak because the cracks in these specimens were comparatively large and continuous. From these results it becomes clear that a continuous crack is more harmful than discrete isolated microcracks and has the effect of lowering the strength of the specimens.

The microcracks present on the grain boundary also influenced the stress–strain relationship of the specimen, which is shown in Fig. 5. The specimen sintered at 1300 °C showed a linear stress–strain relation, whereas the specimens sintered at 1450 and 1500 °C did not show such behaviour and fractured in a more stable manner. From the initial straight part of the stress–strain curves, the Young's modulus was calculated and this is also

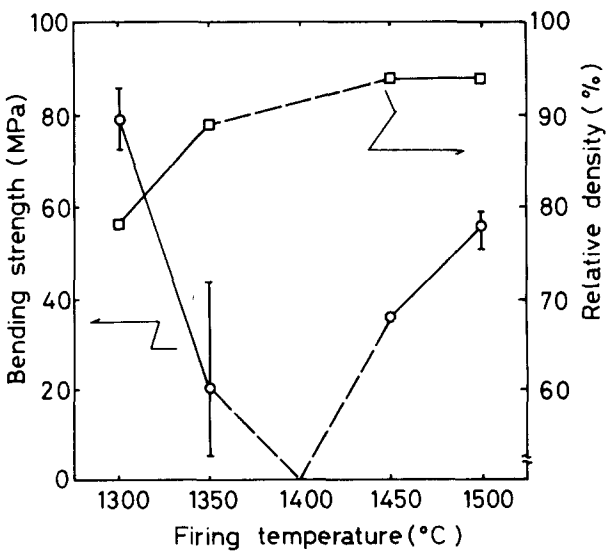

Fig. 4. Bend strengths and bulk densities of sintered specimens.

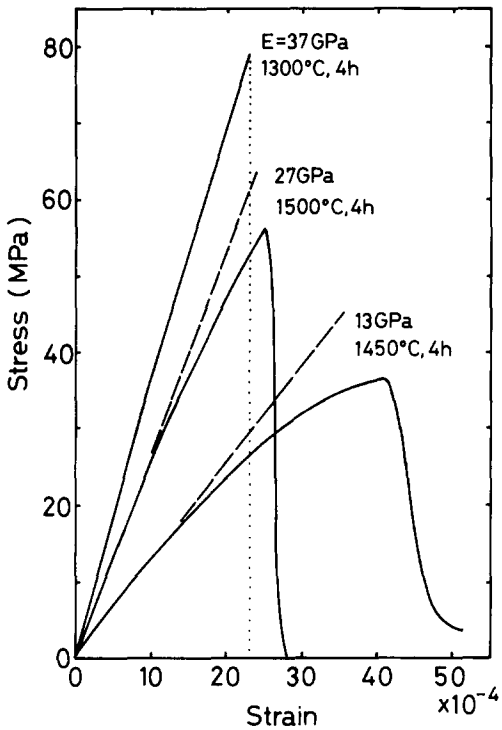

Fig. 5. Stress–strain curves obtained in 3-point bending.

shown in Fig. 5. The specimen sintered at 1300 °C has a higher modulus than the others, which whilst denser, contained appreciable amounts of cracks on their grain boundaries. This decrease in Young's modulus of the specimens containing grain boundary microcracks would be caused by the decrease in the area of contact across the sintered grain boundaries.

The microcracks also affected the fracture behaviour of the specimens. After the bend test, the specimens sintered at 1450 and 1500 °C did not break into separate pieces (Fig. 6(a)). In these specimens, as shown on scanning electron micrographs of their side surfaces in Fig. 6(b), cracks were deflected, branched, and blunted by the grain boundary microcracks and these processes finally combined to stop further propagation.

3.3. Work of fracture and crack propagation velocity during fracture

The work of fracture of the specimens sintered at 1300 and 1450 °C was measured. In this measurement both specimens were fractured in a stable manner. The work of fracture, γ_{wof}, was calculated to be $16{\cdot}8 \pm 0{\cdot}3$ and $38{\cdot}6 \pm 3{\cdot}1\ \mathrm{Jm}^{-2}$ for specimens sintered at 1300 and 1450 °C, respectively. This result indicates that the presence of the grain boundary microcracks in the specimen sintered at 1450 °C increases the work of fracture.

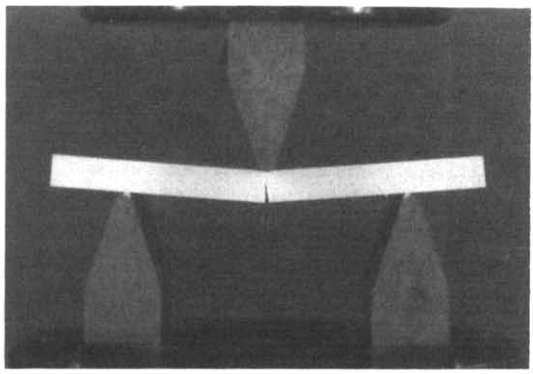

(a)

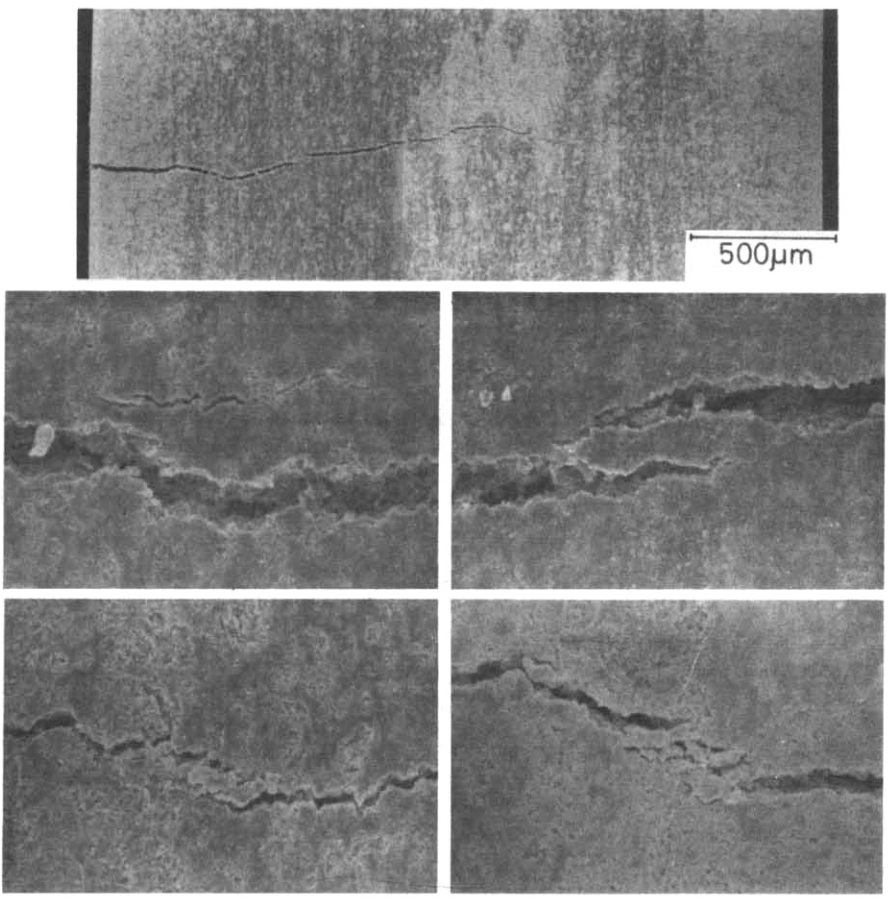

(b)

Fig. 6. Specimen fracture (a) and the side surface (b) of the specimen sintered at 1450 °C, after the bend test.

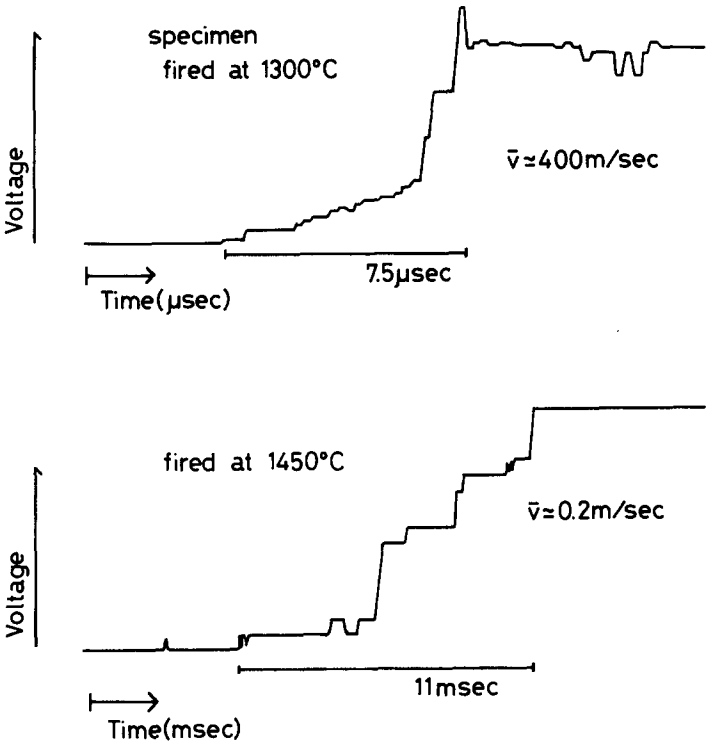

Fig. 7. Voltage–time relationships obtained during fracture, used to determine crack velocity.

Figure 7 shows voltage changes between two terminals printed on the side surface of the specimens sintered at 1300 and 1450 °C during fracture in the bend test. From this graph mean velocities of crack propagation were determined. The velocities were calculated to be ~ 400 and $0{\cdot}2\ \mathrm{m\ s^{-1}}$ for the specimens sintered at 1300 and 1450 °C, respectively. A fast crack extension speed of $400\ \mathrm{m\ s^{-1}}$ is a value comparable with that reported for hot-pressed silicon nitride[15] and other dense ceramics. The microcracks on the grain boundaries in aluminium titanate thus decrease the crack propagation velocity to 1/2000 of the velocity for microcrack-free specimens.

These measurements of the crack propagation velocity and the change in value of the work of fracture give a strong indication that the grain boundary microcracks interfere significantly with the crack extension.

4. CONCLUSION

Microcracks on the grain boundaries of the aluminium titanate studied decrease the bend strength and Young's modulus of the specimens by linking

with a critical crack and by reducing the area of contact between boundaries. However, these microcracks increase the resistance to crack propagation on fracture by mechanisms involving crack deflection, branching and blunting.

REFERENCES

1. Buessem, W. R., Thielke, N. R. and Sarakauskas, R. V., *Ceramic Age*, **60** (1952) 38.
2. Hamano, K., *Taikabutsu* [*Refractories*], **27** (1975) 520.
3. Morosin, B. and Lynch, R. W., *Acta Cryst.*, **B28** (1972) 1040.
4. Davidge, R. W., *Acta Met.*, **29** (1981) 1695.
5. Rice, R. W. and Pohanka, R. C., *J. Am. Ceram. Soc.*, **62** (1979) 559.
6. Cleveland, J. J. and Bradt, R. C., *ibid.*, **61** (1978) 478.
7. Hamano, K., Ohya, Y. and Nakagawa, Z., *Yogyo-Kyokai-Shi*, **91** (1983) 289.
8. Ohya, Y., Hamano, K. and Nakagawa, Z. *ibid.*, **91** (1983) 289.
9. Hamano, K., Nakagawa, Z., Sawano, K. and Hasegawa, M., *Nippon Kagaku Kaishi*, (1981) 1647.
10. Qian, D., Ohya, Y., Hamano, K. and Nakagawa, Z., *Yogyo-Kyokai-Shi*, **93** (1985) 315.
11. Green, D. J., Nicholson, P. S. and Embury, J. D., *J. Am. Ceram. Soc.*, **56** (1973) 619.
12. Evans, A. G. and Faber, K. T., *ibid.*, **64** (1981) 394.
13. Evans, A. G. and Faber, K. T., *ibid.*, **67** (1984) 255.
14. Schardin, H. and Struth, W., *Glastech. Ber.*, **16** (1938) 219.
15. Matsunaga, K., Takahira, K., Isobe, T. and Hashimoto, R., *Yogyo-Kyokai-Shi*, **90** (1982) 333.
16. Hamano, K., *Taikabutsu* [*Refractories*], **36** (1984) 231.
17. Wright, R. E., *J. Am. Ceram. Soc.*, **55** (1972) 54.

Received 10 April 1985; amended version received and accepted 31 October 1985

Int. J. High Technology Ceramics **1** (1985) 139–153

Wurtzitic Boron Nitride—A Review

R. R. Wills

TRW, Inc., 1455 East 185th Street, Cleveland, Ohio 44110, USA

SUMMARY

Boron nitride exists in four main crystalline forms. These have graphitic, cubic, rhombohedral and wurtzitic crystal structures. Wurtzitic boron nitride is formed at relatively low temperatures above 12 GPa pressure. It is a hard ceramic with properties closely resembling those of cubic boron nitride, and has found application in composite cutting tools containing cubic boron nitride as the second phase. Earlier suggestions that the excellent performance of these cutting tools may be due to the wurtzitic boron nitride undergoing a stress-induced transformation to graphitic boron nitride appear to be incorrect.

1. INTRODUCTION

Boron nitride exists in several crystalline forms of which the graphitic (g-BN) and cubic (c-BN) forms are the best known because of their similarity to the graphite and diamond forms of carbon. The wurtzitic form (w-BN) has found use in composite cutting tools containing cubic boron nitride as the other phase. These cutting tools, called Geksanit-R or Hexanit-R in the Soviet Union, perform better in certain applications than tool bits composed only of c-BN.[1,2] The reason for this is not clear since the properties of w-BN are not well known. In this paper, the properties of w-BN are discussed primarily with respect to the graphitic and cubic forms of boron nitride. Efforts are also made to understand the fracture behavior of the composite materials consisting of c-BN and w-BN. In particular, the possibility that w-BN toughens the c-BN matrix[3] through a stress-induced transformation toughening mechanism is examined.

While the exact details of the transformation toughening mechanism are

Int. J. High Technology Ceramics 0267-3762/85/$03·30

still uncertain it is well known that a martensitic phase transformation involving a stress-induced shear transformation is responsible for toughening. Shear transformations are exhibited by several ceramics[4] including zirconia and boron nitride. In zirconia ceramics the transformation is from the tetragonal phase to the monoclinic phase, whereas the shear transformation in boron nitride is between the graphitic and wurtzitic forms. The possibility of using the wurtzitic form of boron nitride as a means of toughening ceramics is intriguing because it is metastable at all temperatures and a large volume expansion (51 %) occurs on conversion of the wurtzitic form to the hexagonal form. Thus, the use of the wurtzitic form of boron nitride could produce substantial toughening of a ceramic matrix over a wide temperature range.

2. CRYSTAL STRUCTURES

The wurtzitic form (w-BN) was originally prepared by Bundy and Wentorf[5] by applying high static pressures to g-BN powder. The transformation occurred above 12·5 GPa at low temperature. Figure 1[5] shows that, with

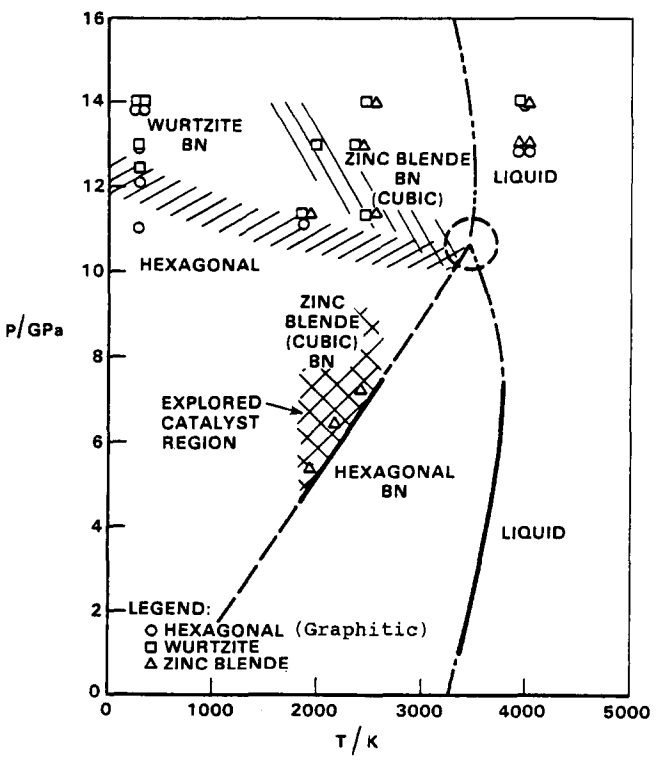

Fig. 1. Boron nitride pressure–temperature diagram.[5]

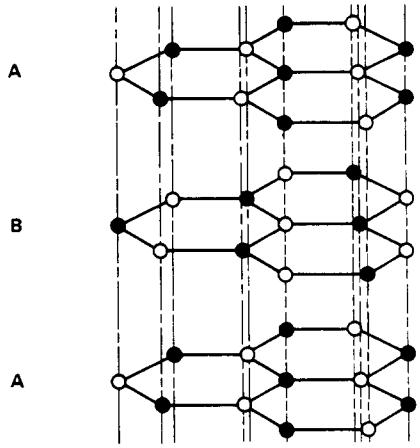

Fig. 2. Crystal structure of graphitic boron nitride.

increasing temperature at the same pressure, the cubic or zinc blende form is usually formed. The crystal structures of g-BN and w-BN are shown in Figs 2 and 3. The graphitic form consists of alternating AB layers, the boron and nitrogen atoms exchanging places in these layers, which are separated by half the length of the c-axis (333 pm). Boron nitride hexagons are nonplanar and form a 'chair' configuration.

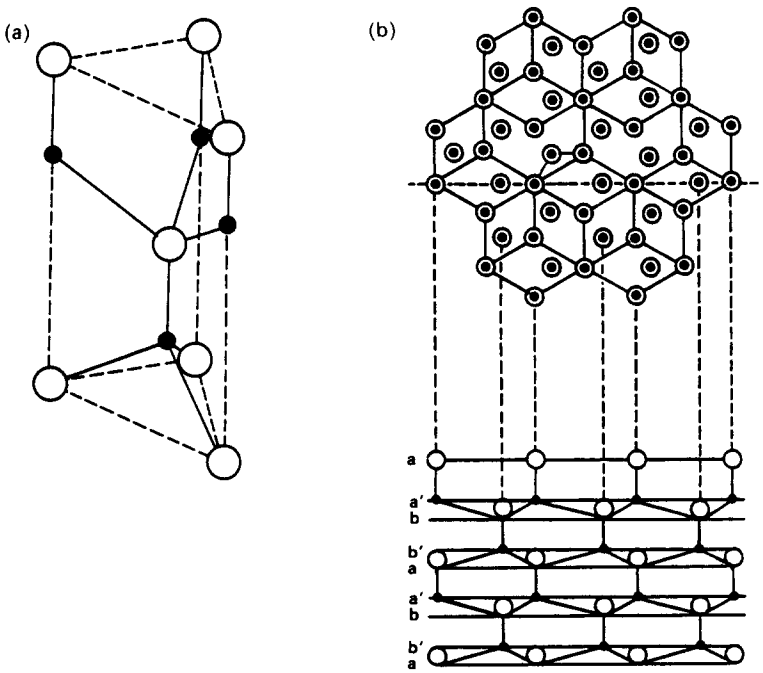

Fig. 3. (a) Hexagonal lattice of wurtzite; (b) schematic representation of the structure of wurtzitic boron nitride.

In the ideal wurtzitic structure (see Fig. 3(a)) each atom is tetrahedrally coordinated with a B—N bond length of 157 pm and a bond angle of 109·5°. The actual coordination tetrahedron in w-BN is distorted, being elongated along the *c*-axis and compressed along the *a*-axis. The distortion also depends upon whether the material was prepared by static or dynamic compaction. The structure consists of a series of close-packed layers alternating all boron and all nitrogen, aa′bb′aa′ (see Fig. 3(b)). The '*a*' unit cell dimension is similar to that found in the graphitic form, but the '*c*' dimension is approximately 35% shorter. The distinct difference in bond length and bond strength in these two crystallographic directions in g-BN is responsible for the large anisotropy in physical and thermal properties. The properties of w-BN are not expected to be as directionally dependent.

Kurdyumov and co-workers[6-16] have studied the substructures of both these forms of boron nitride extensively, using X-ray diffraction and electron diffraction techniques. Twins, stacking faults, and dislocations were found in g-BN. Whole or partial dislocations lie in the [0001] basal planes. Their Burger's vectors are $1/3a$ [$11\bar{2}0$] and $1/3a$ [$10\bar{1}0$], respectively. Stacking faults were characterized as being either polytypic or random. In the first type some hexagonal layers are shifted to positions equivalent to positions in the graphite structure. In the second type there is no correlation between neighboring layers in the defect region. Kurdyumov found the concentration of these defects to increase during shock compression[11] and concluded that the g-BN to w-BN transformation would not occur in regions containing these random or 'turbostratic' stacking faults.

In examining lattice defects in w-BN prepared by both shock and static compaction, Kurdyumov[7] found them to be independent of the preparation method. The crystallographic relations found within the boundaries of individual crystallites in two-phase particles were (001)w‖(001)g and ($11\bar{2}0$)w‖($11\bar{2}0$)g. The lattice parameters of the w-BN samples prepared by the two methods were identical (within the error limits). Considerable comminution[8] occurs during the shock process so that the resulting w-BN particles are less than 0·3 μm in size and consist of 0·05-μm crystallites orientated primarily in the (001) direction normal to the main particle surface. These crystallites are under considerable strain (0·3%).

3. THE GRAPHITIC TO WURTZITIC BORON NITRIDE TRANSFORMATION

At pressures above 12 GPa, g-BN converts to the wurtzitic form.[5] Coleman and Forbes[17] calculated that the temperature at which this occurs is 230 °C. The amount of w-BN formed depends upon the synthesis conditions and

upon the nature of the boron nitride powder, but does not exceed 80% by weight. In particular, it has been shown that the crystallinity is an important factor controlling the transformation. Pyrolytic boron nitride shows very little conversion to w-BN unless it is first converted to g-BN. This is because a crystallographic correspondence exists between g-BN and w-BN. The basal planes of the wurtzitic phase are parallel to the basal planes of the graphitic form. Complete conversion to w-BN presumably does not occur because, in the early stages of compaction, random stacking faults are generated in a fraction of the material. These prevent w-BN formation, as discussed earlier. In addition, adiabatic heating of the powder compact during shock loading probably provides sufficient energy to reconvert some of the w-BN back to g-BN. The shear mechanism proposed for the transformation by Kurdyumov is similar to that proposed earlier by Lonsdale[18] for the graphite to wurtzite transformation in both graphite and boron nitride. Figure 4 illustrates the structure change which arises from shear in the basal plane by a B—N bond distance. The differences in stacking sequence in these two structures are shown more clearly in Figs 2 and 3(b). Kurdyumov explained the transformation in terms of a martensitic transformation, proceeding athermally under the influence of pressure. This does not appear to be correct since, if shock loading is carried out in such a way that the compact does not heat during shock loading,[19] then the conversion from g-BN to the wurtzitic form does not occur at room temperature. Under the same shock loading conditions maximum conversion to w-BN occurs on heating to 200 °C. This temperature is very close to the conversion temperature calculated by Coleman and Forbes[17] for normal shock loading of g-BN at room temperature. Thus both temperature and pressure are required to convert g-BN to w-BN.

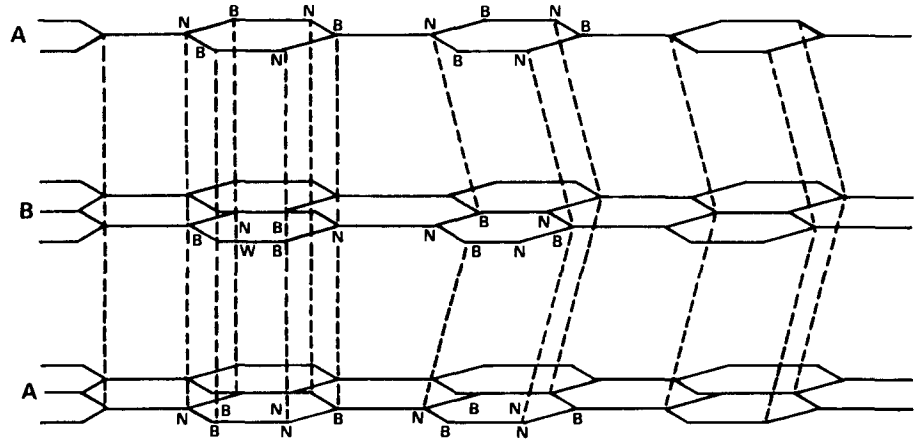

Fig. 4. Graphite → wurtzite orientation relation for boron nitride.[4] The (0001) planes straighten and shear by a B N bond distance.

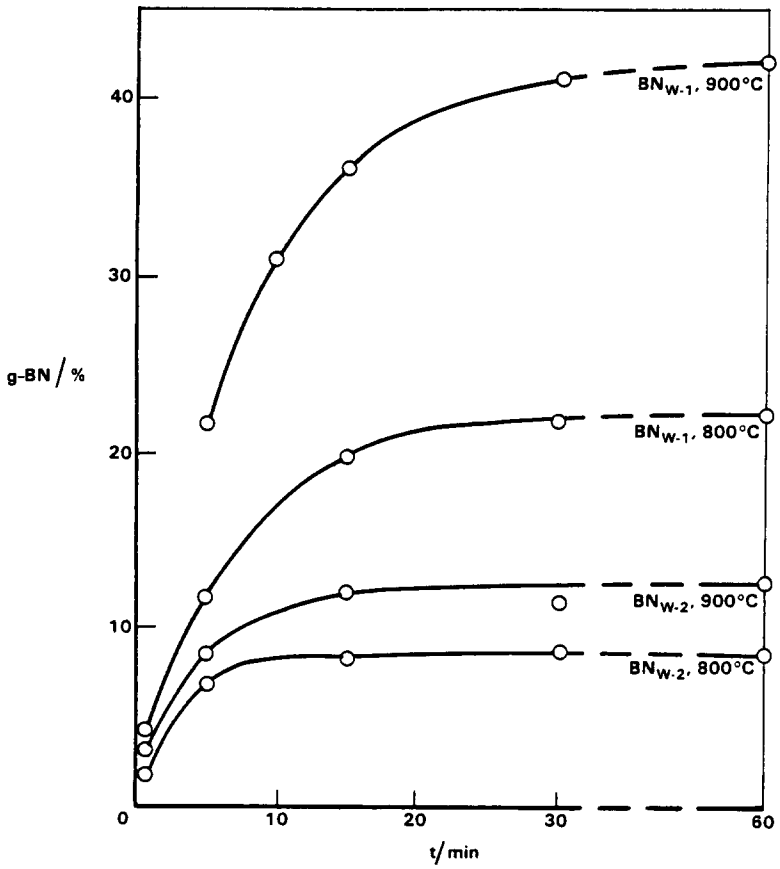

Fig. 5. Transformation of two wurtzitic boron nitride powders to graphitic boron nitride in flowing nitrogen at 800 °C and 900 °C.

The reverse transformation is of particular interest in preparing ceramic composites. On heating, w-BN reverts to a highly defective form of g-BN. There is evidence to suggest that the ambient conditions determine whether the transformation is truly reversible. At normal pressures the relation [0001]g⊥[0001]w was observed,[20] but at high pressures and temperatures the transformation is crystallographically reversible.[21]

Kinetic studies of the transformation at normal pressures have shown that the transformation is rapid, and depends upon both the temperature and the nature of the powder. Figure 5[22] shows the volume fraction of g-BN formed as a function of time at 800 °C and 900 °C for two different w-BN powders. The transformation consists of two stages: an initial rapid stage and a subsequent slow stage in which very little additional g-BN is formed. Kurdyumov *et al.*[20] interpreted the data in terms of a nucleation and growth mechanism and also observed this phenomenon in samples examined under

the electron beam. The reaction kinetics obey an equation of the first order with an activation energy of $21\,kJ\,mol^{-1}$. It was concluded that the transformation was determined by the number of nucleation sites rather than by the growth of the nuclei, and that the transformation was of a diffusionless martensitic type. The exact experimental conditions used to obtain the data in Fig. 5 are not given in Ref. 22, but the factors which would affect the transformation rate would be expected to include powder compact density, particle size, the strain energy in the particles, and impurity content. Table 1[22] shows that there are some differences between the characteristics of these powders in terms of their impurity or second-phase content, but their surface areas are identical. Since it is likely that the surface energy of the powder plays a significant role in the transformation, it is somewhat surprising that the powders labeled $BN_{w\text{-}1}$ and $BN_{w\text{-}2}$ in Fig. 5 exhibit different transformation rates but possess identical surface areas. A difference in the respective strain energies of these powders might be expected because of the threefold difference in loading rates used to produce these powders. Yet if this were the reason for the observed difference in transformation rates, the powder labeled $BN_{w\text{-}2}$ should transform at a higher rate, not a lower rate, as shown in Fig. 5. The explanation offered by Pechentkovskaya and Savvakin[22] is that the extremely high loading rate conditions give rise to a new form of w-BN in which some changes in the fine structure of the valence band and conduction band exist. It is difficult to envisage why this modification of w-BN should be more stable if it is in some kind of excited state. Their explanation, therefore, cannot be considered to be very plausible.

The experimental data indicate that the transformation is both temperature and stress dependent. Both temperature and pressure are necessary to convert g-BN to w-BN, but the reverse transformation occurs at atmospheric pressure with a low activation energy typical of a displacive or diffusionless transformation mechanism. It does not, however, appear to be a martensitic transformation. This is in agreement with Kriven[4] who concluded that claims for a martensite mechanism in terms of an invariant plane strain model were not justified.

TABLE 1
Characteristics of Two Wurtzitic Boron Nitride Powders[22]

Material	*Average loading rate/* $GPa\,s^{-1}$	*Content of the basic phase and impurities/* %				*Surface area/* $m^2\,g^{-1}$
		w-BN	*g-BN*	B_2O_3	O_2	
$BN_{w\text{-}1}$	10^7	97·2	0·8	0·15	0·7	15
$BN_{w\text{-}2}$	10^{10}	95·6	2·4	0·10	1·6	15

4. PROPERTIES OF WURTZITIC BORON NITRIDE

The thermal and mechanical properties of w-BN are given in Tables 2 to 5. It should be noted that measurements were frequently made on impure samples or multiphase specimens such as the cutting tool material Geksanit-R (a two-phase boron nitride ceramic containing principally w-BN and c-BN). Some of the materials also contained residual stresses or were

TABLE 2
Thermal Properties of the Wurtzitic, Graphitic and Cubic Forms of Boron Nitride

Property	*Temperature (K)*	*w-BN*	*g-BN*	*c-BN*
Specific heat/$J\,kg^{-1}\,K^{-1}$ at constant pressure	300	810 (Ref. 23)	800 (Ref. 24)	270 (Ref. 25)
Thermal conductivity/ $W\,m^{-1}\,K^{-1}$	1 150	60 (Ref. 26)	15–30 (Ref. 24)	26 (Ref. 26)
Linear coefficient of thermal expansion/ $M\,K^{-1}$	300–530	3·7[a] (Ref. 38)		2·8 (Ref. 38)
	300–550	2·7[b] (Ref. 38)		
	270–1 070		40·5[a] (Ref. 39)	
	270–370		−2·9[b] (Ref. 39)	

Note: Temperatures given represent those for which data have been found for w-BN. More extensive data are available for g-BN and c-BN.
[a] Value in the '*c*' direction.
[b] Value in the '*a*' direction.

TABLE 3
Room Temperature Hardness Values for w-BN and c-BN Specimens

Material	*Measurement method*[a]	*Hardness/GPa*	*Reference*
c-BN	Vickers	>66·7	29
w-BN	Vickers	22·3	29
w+c-BN	Vickers	67·7	29
w+c-BN	Vickers	87·3	30
w-BN	Vickers	52·5	31
c-BN	Vickers	58·7	31
w-BN	Knoop	35·6	31
c-BN	Knoop	48·9	31
w+c-BN	Vickers	48·9–71·2[b]	32, 34
c-BN	Vickers	38·3	34

[a] Vickers hardness measurements were made at a load of 0·5 kg, Knoop at a load of 0·4 kg.
[b] Specimens were heat treated prior to testing.

TABLE 4
Young's Modulus, Fracture Toughness, and Fracture Surface Energy Values for Wurtzitic Boron Nitride Materials

Property	*Material*	*Value*	*Reference*
Young's modulus/GPa	50% c-BN, 50% w-BN	890	32
Fracture toughness/MPa $m^{1/2}$	Mixed w-BN/c-BN	15–17·05	34
	100% c-BN	14·57–17·05	34
	Mixed c-BN/w-BN containing 2–7% g-BN	5·89–6·20	34
	100% c-BN	16–18	33
	Mixed c-BN/w-BN	16–18	33
	Mixed c-BN/w-BN after annealing	10–14	33
Fracture surface energy/J m^{-2}	Mixed w-BN/c-BN	62–75	33, 34
	100% c-BN	62–75	

microcracked. Comparisons are made with the corresponding data for the cubic and graphitic forms of boron nitride (see Tables 2 and 3) and with several other ceramics (Tables 5 and 6).

The specific heat data at 300 K and the thermal conductivity data at 1150 K are shown in Table 2. The specific heat of the wurtzitic form (810 J kg^{-1} K^{-1}) is similar to that for the graphitic form (800 J kg^{-1} K^{-1}). The range of values for the thermal conductivity of g-BN reflects the anisotropy of this material, the higher value being for the '*a*' axis or basal plane in which the atoms are closer together. Even if the w-BN specimens used by Fedoseev *et al.*[26] were textured so that conduction was measured only along the '*a*' direction, this would still not explain the very high thermal conductivity found for this form of boron nitride. The specimen contained 15% c-BN, so that if the appropriate correction is made using the data in

TABLE 5
Room Temperature Fracture Toughness Values for Boron Nitride and Other Ceramics

Material	*Fracture toughness*[a] *MPa $m^{1/2}$*	*Reference*
c-BN/w-BN	15·5–17·05	34
100% c-BN	14·47–17·05	34
Silicon nitride	4·96	35
Cobalt-bonded tungsten carbide	16·75	35
Diamond	9·61	34
Sapphire (single crystal)	2·1	35

[a] Determined by the indentation technique of Evans and Charles.[35]

TABLE 6
Room Temperature Fracture Surface Energies for Alumina, Silicon Nitride and Wurtzitic Boron Nitride

Material	*Fracture surface energy/* $J m^{-2}$	*Reference*
c-BN/w-BN	70	34
Hot pressed alumina	42[a]	36
	21[b]	36
Sintered alumina	23	36
Hot pressed silicon nitride	61[a]	36
	42[b]	36

[a] Flaw moving perpendicular to hot pressing direction.
[b] Flaw moving parallel to hot pressing direction.

Table 2, the thermal conductivity of w-BN is actually nearer 70 $W m^{-1} K^{-1}$. This is a very high value for a ceramic at this temperature and may be one reason that the cutting tools consisting of both c-BN and w-BN perform better than those composed of only c-BN. The higher thermal conductivity of w-BN is difficult to explain in terms of its crystal structure. Slack *et al.*[27,28] concluded that ceramics with high thermal conductivities possessed four characteristics: (1) low atomic mass, (2) strong bonding, (3) a simple crystal structure, and (4) low anharmonicity. On this basis, the simpler crystal structure of c-BN should result in the highest thermal conductivity value for any of the allotropes of boron nitride. Single-crystal c-BN has the highest thermal conductivity after diamond; thus, the high value for w-BN (60 $W m^{-1} K^{-1}$ (Ref. 26)) is surprising, more so because it is not just slightly higher, but twice that for the c-BN specimen. The samples used by Fedoseev *et al.* were polycrystalline. Consequently, a likely explanation for the disparity in thermal conductivities is that it is due to differences in porosity and impurity content of the two specimens. The single-crystal value for w-BN should be lower than that for c-BN.

There is a marked difference in the thermal expansion coefficients of the wurtzitic and graphitic forms of boron nitride (see Table 2). The weak van der Waals forces between the layers of atoms in the '*c*' direction of g-BN are responsible for the high expansion coefficient in this direction. Stronger bonding exists between the layers of atoms in w-BN. Consequently, it has a lower expansion coefficient and exhibits only moderate anisotropy in expansion values. The thermal expansion coefficient of w-BN (average 3·2 $M K^{-1}$) is close to that of c-BN (2·8 $M K^{-1}$ (Ref. 38)) and silicon nitride (2·9 $M K^{-1}$ (Ref. 24)).

Hardness values for various specimens of w-BN and c-BN, shown in Table 3, exhibit considerable scatter for several reasons. First, most of the

materials examined by Bochko and co-workers[31–33] were made by a process that gave rise to a temperature distribution in the samples during processing. Furthermore, many of the materials contained residual stresses arising from their multiphase composition. Stresses arise from the thermal expansion mismatch between w-BN and c-BN ($1{\cdot}0\ M\ K^{-1}$, see Table 2) on cool-down, and from the formation of g-BN from either w-BN or c-BN during processing. Secondly, some of the samples listed in Table 3 were not fully dense. Annealing[31–33] to eliminate these stresses resulted in higher hardness values,[34] and a smaller scatter in values was obtained for the Geksanit-R materials. The hardness of w-BN is similar to that of c-BN.

The Young's modulus and fracture toughness values[32–34] for the mixed phase Geksanit-R materials and c-BN are shown in Table 4. The Young's modulus of 890 GPa is high for a ceramic and only about 15% lower than that for diamond (1033 GPa[32]). The data in Table 4 are not strictly accurate since all samples contained residual stresses unless they were annealed out. This is the reason for the differences in values for c-BN in Refs 33 and 34 and for the Geksanit-R material in Ref. 34 (Table 4 shows that annealing causes the fracture toughness of the mixed phase Geksanit-R to decrease from 16–18 MPa $m^{1/2}$ to 10–14 MPa $m^{1/2}$). The fracture toughness drops drastically if the material contains more than a small amount of g-BN. For example, Geksanit-R materials containing 2–7% g-BN exhibit a much lower fracture toughness (6 MPa $m^{1/2}$ (Ref. 34)). This decrease in fracture toughness can be only partly explained by the lower Young's modulus (90 GPa[24]) of g-BN. These materials exhibit both intergranular and transgranular fracture, whereas Geksanit-R fractures only intergranularly. It thus appears that the main reason for the substantial decrease in fracture toughness is that the g-BN provides a lower resistance crack path. Toughening through a crack deflection mechanism is reduced since the advancing crack moves through the g-BN particles.

The fracture toughness values for c-BN and the mixed Geksanit materials are similar (approximately 16 MPa $m^{1/2}$). Table 5 shows that this is higher than that for any other known monophase ceramic material and comparable to that for cobalt-bonded tungsten carbide. This is partly due to its high Young's modulus, but not entirely, since diamond also has a high Young's modulus but possesses a lower fracture surface energy. In Table 6 the fracture surface energies of several ceramics are given. The boron nitride materials have a high fracture surface energy in spite of their very fine grain size ($< 3\ \mu m$). This is difficult to explain in terms of conventional fracture behavior since fine-grained, polycrystalline ceramics do not generally have a high fracture surface energy. For example, in both hot-pressed alumina and silicon nitride crack propagation around the high aspect grains is responsible for their relatively high fracture energies in the direction

perpendicular to the hot-pressing direction (see Table 6). In fine-grained, sintered alumina the fracture surface energy is 50 % lower. Complicating the issue also is the fact that the 100 % c-BN samples and Geksanit-R materials have different grain sizes and fracture modes, but possess similar fracture toughness values. Geksanit-R has a grain size of approximately 0·5 μm and an intergranular fracture mode, whereas c-BN has a slightly higher grain size (1–2 μm), and exhibits both intergranular and transgranular fracture.[34]

A fracture surface energy of 70 J m^{-2} is high for a fine-grained structure. One mechanism that might explain these data is transformation toughening. Following the method of Evans *et al.*,[37] the contribution to toughening by the transformation can be estimated:

$$\Delta K_{Ic} = 0{\cdot}34\ V_f E\,(\Delta V/V) r_0^{1/2}$$

where ΔK_{Ic} = the contribution to toughening due to the transformation; V_f = the volume fraction of transformable particles; E = Young's modulus; $(\Delta V/V)$ = the transformation volume strain; and r_0 = the width of the transformation zone.

Although this equation ignores any contribution due to shear strains, it enables an estimate of the amount of toughening due to volumetric changes. Assuming that r_0 is equal to the grain size (0·1 μm), the effect of 50 % w-BN in a matrix of c-BN would be to increase its fracture toughness by 25 MPa m$^{1/2}$. Table 4 shows very little difference in the fracture toughness values for the cubic and mixed-phase boron nitrides. Furthermore, Claussen[40] was unable to detect any stress-induced transformation toughening in silicon nitride and cordierite composites containing w-BN. Transformation toughening can, therefore, be ruled out as the mechanism responsible for the high fracture energy. It seems more likely that microcracking is the toughening mechanism, particularly since these boron nitride materials were formed under non-uniform temperature conditions and usually contain residual stresses. In view of the similarity in the properties of w-BN and c-BN it is difficult to explain, using the available information, why the Geksanit-R cutting tools perform better than the c-BN materials.

ACKNOWLEDGEMENT

The author wishes to acknowledge helpful technical discussions with Dr D. K. Shetty of Battelle Columbus Laboratories and to thank the Air Force Office of Scientific Research for supporting this project.

REFERENCES

1. Karyuk, G. G., Kolomiets, I. P., Fedoseev, V. V., Bochko, A. V., Dhamarov, S. S. and Uvarov, V. V., Geksanit-R—a new superhard material, *Porosh. Metall.*, **10**(130) (1973) 102.
2. Saito, S. and Sawaoka, A., in *High Pressure Science and Technology, Proc. 7th Int. AIRAPT Conference*, Eds B. Vodar and Ph. Marteau, Pergamon Press, Oxford, 1980, 541.
3. Pilyankevich, A. N. and Claussen, N., Toughening of BN by stress induced phase transformation, *Mat. Res. Bull.*, **13** (1978) 413.
4. Kriven, W. M., Shear transformations in inorganic materials, *Proc. Int. Conference on Solid Solid Phase Transformations*, Carnegie Mellon University, Pittsburgh, 1981, 1507–32.
5. Bundy, F. P. and Wentorf, R. H., Direct transformation of hexagonal boron nitride to denser forms, *J. Chem. Phys.*, **38**(6) (1963) 1144.
6. Kurdyumov, A. V., Ostrakova, N. F., Pilyankevich, A. N. and Frantsevich, I. N., Electron-optical study of the products of shock compression of boron nitride, *Dokl. Akad. Nauk. SSSR*, **215**(4) (1974) 836.
7. Kurdyumov, A. V., Ostrakova, N. F., Pilyankevich, A. N., Dubitskii, G. A. and Slesarev, V. N., Crystal structures of wurtzite type boron nitride prepared at high static pressures, *Dokl. Akad. Nauk. SSSR*, **229** (1976) 338.
8. Kurdyumov, A. V. and Frantsevich, I., Influence of impact compression on the crystal structure of boron nitride, *Dokl. Akad. Nauk. SSSR*, **221**(3) (1975) 588.
9. Kurdyumov, A. V. and Pilipenko, V. A., Stacking faults in the structure of the wurtzitic modification of boron nitride and their role in the wurtzite to sphalerite type phase transformation, *Dokl. Akad. Nauk. SSSR*, **224** (1979) 348.
10. Kurdyumov, A. V., Ostrakova, N. F. and Pilyankevich, A. N., Twinning in graphite like boron nitride, *Sov. Phys. Cryst.*, **21**(2) (1976) 418.
11. Kurdyumov, A. V., Stacking faults in graphitic boron nitride, *Sov. Phys. Cryst.*, **20**(5) (1975) 969.
12. Kurdyumov, A. V., Distortions in the lattice of wurtzite type boron nitride, *Porosh. Metall.*, **12**(156) (1975) 69.
13. Kurdyumov, A. V., Ostrakova, N. F., Pilyankevich, A. N. and Frantsevich, I. N., Investigations of the substructure of a wurtzite like modification of boron nitride, *Dokl. Akad. Nauk. SSSR*, **209**(5) (1973) 1081.
14. Kurdyumov, A. V., Ostrakova, N. F., Pilipenko, V. A., Pilyankevich, A. N., Savvakin, G. A. and Trefilov, V. I., Structure of boron nitride after high temperature shock compression, *Dokl. Akad. Nauk. SSSR*, **246** (1979) 1113.
15. Kurdyumov, A. V., Oleinik, G. G., Ostrakova, N. F., Pilyankevich, A. N., Gromyko, S. N. and Frantsevich, I. N., Multilayered polytypes in boron nitride, *Dokl. Akad. Nauk. SSSR*, **265** (1982) 66.
16. Kurdyumov, A., Ostrakova, N. F., Pilipenko, V. A. and Pilyankevich, A. N., Structures occurring in boron nitride during shock compression in the presence of water, *Porosh. Metall.*, **9**(189) (1978) 76.
17. Coleman, N. L. and Forbes, J. W., Irreversible transformation of hexagonal boron nitride by shock compression, *J. Chem. Phys.*, **48**(2) (1968) 555.
18. Lonsdale, K., Formation of Lonsdaleite from single crystal graphite, *Am. Miner.*, **56** (1971) 333.

19. Adadurov, G. A. and Godanski, V. I., *Russ. Chem. Rev.*, **50**(10) (1981) 948.
20. Kurdyumov, A. V., Ostrakova, N. F., Pilyankevich, A. N., Balan, T. R. and Bochko, A. V., Phase and structural transformations of wurtzite type boron nitride at high temperatures, *Porosh. Metall.*, **1** (1976) 64.
21. Pesin, V. A., Sokhor, M. I. and Feldgun, L. I., The mechanisms of the phase transformation of the wurtzite like boron nitride at high pressures, *Russ. J. Phys. Chem.*, **53**(6) (1979) 908.
22. Pechentkovskaya, L. E. and Savvakin, G. I., Properties of wurtzite like boron nitride crystallized under dynamic conditions, *Soviet Powder Met.*, **23**(4) (1984) 319.
23. Sirota, N. N. and Kofman, N. A., Temperature characteristics of the thermodynamic properties of wurtzitic boron nitride over the 5–300 K range, *Dokl. Akad. Nauk. SSSR*, **230** (1976) 82.
24. *Engineering Property Report Data on Selected Ceramics, Volume 1, Nitrides*, The Metals and Ceramics Information Center, Battelle's Columbus Laboratories, Columbus, Ohio, March, 1976.
25. Kiseleva, I. N., Melchakova, L. V. and Topor, N. D., Experimental determination of the high temperature specific heat of β-boron nitride, *Izv. Akad. Nauk. SSSR, Neorg. Mater.*, **9**(3) (1973) 494.
26. Fedoseev, D. V., Lavrentev, A. V., Varshavskaya, I. G., Bochko, A. V. and Karyuk, G. G., Determination of the thermal conductivities of refractory materials with the aid of an optical quantum generator, *Porosh. Metall.*, **183**(3) (1978) 92.
27. Slack, G. A., Nonmetallic crystals with high thermal conductivity, *J. Phys. Chem. Solids*, **34** (1973) 321.
28. Borom, M. P., Slack, G. A. and Szymaszek, J. W., Thermal conductivity of commercial aluminium nitride, *Bull. Am. Ceram. Soc.*, **51**(11) (1972) 852.
29. Saito, S. S., Shock synthesis and very high pressure sintering of high dense form boron nitride, *Proc. International Symposium on Factors in Densification and Sintering of Oxide and Nonoxide Ceramics*, Tokyo, Japan, 1978.
30. Sawaoka, A. and Kondo, K., *Progress in Shock Wave Research at the Research Laboratory of Engineering Materials*, Report of the Research Laboratory of Engineering Materials, Tokyo Institute of Materials, **9** (1984) 131.
31. Bochko, A. V., Grigorev, O. N., Dhamarov, S. S., Karyuk, G. G., Millman, Yu. V. and Trefilov, V. I., Temperature dependence of the hardness of boron nitride, *Porosh. Metall.*, **6**(174) (1977) 64.
32. Bochko, A. V., Grigorev, O. N., Dhamarov, S. S., Karyuk, G. G., Pilyankevich, A. N., Trefilov, V. I., Frantsevich, I. N. and Shatokhin, A. M., Effect of structural factors on the ductility and strength properties of superhard materials based on boron nitride, *Porosh. Metall.*, **5**(209) (1980) 96.
33. Grigorev, O. N., Dhamarov, S. S., Trefilov, V. I. and Shatokhin, A. M., Effect of heat treatment on the structural state and mechanical properties of polycrystals based on superhard boron nitride modifications, *Porosh. Metall.*, **1**(217) (1981) 53.
34. Bochko, A. V., Grigorev, O. N., Dhamarov, S. S., Karyuk, G. G., Kurdyumov, A. V., Oleinik, G. S., Pilyankevich, A. N., Trefilov, V. I., Frantsevich, I. N. and Shatokhin, I. M., Effect of structural factors on the mechanical properties of superhard materials based upon boron nitride, *Porosh. Metall.*, **10**(202) (1979) 61.

35. Evans, A. G. and Charles, E. A., Fracture toughness determination by indentation, *J. Am. Ceram. Soc.*, **59**(7–8) (1976) 371.
36. Bansal, G. K., Effects of ceramic microstructure on strength and fracture surface energy, in *Ceramic Microstructures 76*, Ed. R. M. Fulrath and J. A. Pask, Westview Press, Boulder, Colorado, 1977, 860–71.
37. Evans, A. G., Marshall, D. B. and Burlingame, N. H., Transformation toughening in ceramics, in *Advances in Ceramics: Science and Technology of Zirconia*, Eds A. H. Heuer and L. W. Hobbs, American Ceramic Society, Columbus, Ohio, 1981, 202–16.
38. Kurdyumov, A. V. and Pilyankevich, A. N., Phase transformations in carbon and nitride of boron, *Knizhnaya Letopis 80*, No. 9 (1979) 28.
39. Pease, R. S., An X-ray study of boron nitride, *Acta Cryst.*, **5** (1952) 356.
40. Claussen, N., Private communication, 1984.

Received 1 May 1985; amended version received and accepted 29 October 1985

Int. J. High Technology Ceramics **1** (1985) 155–156

Workshop Report

WORKSHOP ON TRANSFORMATION TOUGHENING, LORNE, AUSTRALIA (15–19 April, 1985)

The workshop organised by the Zirconia group at CSIRO was host to many international participants. The largest contingents were from America and Australia but Japan, West Germany and the People's Republic of China were also strongly represented.

Of the four days devoted to the workshop, the first, after the official opening by Professor Polmear, was concerned with the crystallography, thermodynamics and nucleation of the transformation process in zirconia. Summaries of the state-of-knowledge in these areas were given by Professor A. H. Heuer in his usual lucid style, by Dr R. Cannon and Dr M. Rühle. Up-to-date information on the t' phase was given by Professor Heuer who, using electron micrographs to illustrate his ideas, showed it to be the stable non-transformable phase at room temperature. In this section Dr P. Kelly gave a discourse on the martensitic transformation process that was notable for both its clarity and quality.

The processing theme was developed by Dr F. F. Lange of the Rockwell International Science Centre who supplemented an earlier lecture on the distribution and source of flaws in engineering ceramics with pertinent information on the failure mechanism involved in the degradation of yttrium oxide-stabilised zirconium dioxide in the temperature range 150–400 °C. He showed convincing evidence of yttria removal from solid solution into discrete precipitates within adjacent porosity, the mechanism still being open to discussion. On the same topic, Dr Rühle suggested that mechanical constraint was necessary for the transformation to proceed.

Int. J. High Technology Ceramics (1) (1985)—

Phase diagrams were discussed in detail and it was a general conclusion of the meeting that great care was required to generate reproducible data, which could be affected by numerous variables, ranging from the powder source, to the disposition of the research worker.

As the meeting moved towards discussion of the means of attaining strength and toughness, it became apparent that two phenomena were becoming recognised as being of great importance, specifically, surface strengthening and a form of microplasticity caused by microtwinning in the relatively long range stress fields ahead of a crack tip. Dr D. Green gave an account of the methods available for the development of surface compressive stresses, concluding that removal of the stabilising oxide from the surface gives the greatest thickness (40–50 μm) of compressive layer. An elegant method developed at Utah was quoted, whereby slip-casting allowed the larger zirconium dioxide particles to be at a surface of a ceramic body; these larger particles are most likely to transform and the process thus gives a method for control of the thickness of the compressive surface layer.

Dr D. B. Marshall discussed perhaps the most significant work presented, the concept of a reversible $t \rightarrow m$ transformation. On loading, the surface of a test piece of Mg PSZ becomes rumpled on a scale equivalent to the grain size, the rumpling being removed on unloading, i.e. the process was reversible. Deformation strains of 0·17 % were achieved before 'microcracking' took place. On unloading, the surface became smooth apart from regions adjacent to the microcracks. X-ray diffraction data were also presented which indicated that the amount of monoclinic increased with the applied load and decreased as the load was removed. Dr Richard Hannick, the co-author of the original paper 'Ceramic steel', supported the hypothesis showing 'deformation bands', $\sim 500\ \mu$m long, on the inner surface of a wire drawing die. In a later paper he showed again the similarity of the zirconia transformations to the martensitic transformation in steel.

Classic micrographs and experiments illustrating an isothermal transformation at 1340 °C in Mg PSZ were shown demonstrating that three stages of the precipitation process could be represented on a TTT (transformation/temperature/time) diagram, specific to the $MgO–ZrO_2$ ceramic.

The atmosphere of the conference was positive and enthusiastic and the participants foresaw a practical and increasingly useful place for zirconia ceramics in engineering materials. As a celebration of the ten years work of the Australian group, the meeting was a fitting accolade to the major contributions they have made over this period and was acknowledged as such by all those attending.

R. Stevens

Int. J. High Technology Ceramics **1** (1985) 157–158

Book Review

Engineering Ceramics 1984. Edited by M. Ish-Shalom and D. G. Brandon. Elsevier Applied Science Publishers, London, 1985. 408 pp. ISBN 0-85334-397-7. Price: £65.00.
(Reprinted from the journal *Materials Science and Engineering*, Vol. 71, Nos 1–2.)

This volume constitutes the proceedings of the International Symposium on Engineering Ceramics which was held in Jerusalem, Israel, during December 16th to 20th 1984. The symposium was attended by 120 research scientists and engineers from 14 different countries.

The reviewer who was fortunate to attend this enjoyable and interesting conference would like to congratulate the editors and publishers for the speed with which they have been able to produce this attractive volume.

The editorial note mentions that the authors of the papers presented at this conference were asked whether they wished to submit their paper for publication in these proceedings. All the papers accepted for publication have been thoroughly refereed. Abstracts of the papers presented at the conference which are not published in full in these proceedings have been included but have not been refereed. Manuscripts had to be submitted at the time of the conference and it is obvious that rapid publication, which is so highly desirable, could only be achieved by not delaying publication for the sake of including late contributions. Thus, of the 59 contributions which were presented, 20 are published only as abstracts because they were either not submitted in time or were not passed by the referees. In fact, one of the contributions which was not ready at the time has been published in the first

Int. J. High Technology Ceramics (1) (1985)—

issue of *High Technology Ceramics* (G. Ziegler and G. Wötting, Post-treatment of pre-sintered silicon nitride by hot isostatic pressing, *High Technology Ceramics*, **1** (1985) 31–58).

The 59 contributions, full papers and abstracts, apart from the introductory paper by A. G. Evans on Engineering property requirements for high performance ceramics, are grouped in the following sections:

1. Microstructure and properties
2. Reliability
3. Applications
4. Processing
5. Electronic and optical ceramics.

The Local Organizing Committee selected eight key topics to be dealt with by invited speakers. The titles and authors apart from the introductory paper were:

—Strengthening strategies for ZrO_2-toughened ceramics at high temperatures (N. Claussen)
—Structural reliability of ceramic materials (S. M. Wiederhorn and E. R. Fuller, Jr)
—Recent trends in the development of fine ceramics in Japan (H. Suzuki)
—Applications of high performance ceramics in heat engine design (R. N. Katz)
—Thermal stress resistance of engineering ceramics (D. P. H. Hasselman)
—Processing technology for high performance ceramics (R. J. Brook)
—Recent advances in ceramic coatings obtained by chemical vapour deposition and plasma processing deposition (R. Avni and U. Carmi).

These papers formed the backbone of the conference but other interesting contributions were presented in lectures or as posters. It is gratifying now to be able to study their full text. The ceramic materials covered are: zirconia, alumina, silicon nitride, silicon carbide, silicon oxynitride, sialons (the reviewer regrets to see the use of a commercial trade name, i.e. Syalon, in a title!), titanium diboride, lead zirconate titanate, and complex systems like mullite–zirconia, etc.

Readers of *High Technology Ceramics* will find a lot of interesting information in this volume, which is well produced; contrary to many conference proceedings volumes, it contains an author and subject index which considerably enhances the ability of a reader to find the required information.

Paul Popper

International Journal of
HIGH TECHNOLOGY CERAMICS

The *International Journal of High Technology Ceramics* will concentrate its attention on research papers which deal with the development, fabrication and utilisation of modern ceramic materials that have technological, as well as commercial potential. The Journal will publish papers of high scientific standard and will provide a much needed interface for scientists, technologists and engineers working with ceramic materials. Attention will also be given to the concept of ceramic engineering, be it for mechanical, electrical, magnetic or other special applications.

Manufacturing-related topics with which this Journal will be concerned include: powder synthesis, processing and fabrication techniques such as slip casting, injection mouldings, isostatic pressing, CVD and hipping.

Materials to be covered in the areas of engineering and electrical ceramics will include silicon carbide, silicon nitride, sialons, alumina, zirconia and zirconates, titanates, ferrites and aluminates.

Papers dealing with the interaction between design, manufacture and microstructural control will be particularly welcome.